THE HONG KONG POLYTECHNIC UNIVERSITY
THE DEPARTMENT OF APPLIED PHYSICS

STUDY OF BNT-BKT-BT LEAD-FREE PIEZOELECTRIC CERAMICS AND THEIR APPLICATION IN PIEZOELECTRIC DEVICES

SUBMITTED BY

CHOY SIU HONG

A THESIS SUBMITTED IN PARTIAL FULFILMENT
OF THE REQUIREMENTS FOR THE DEGREE OF
DOCTOR OF PHILOSOPHY

NOVEMBER 2006

CERTIFICATE OF ORIGINALITY

I hereby declare that this thesis is my own work and that, to the best of my knowledge and belief, it reproduces no material previously published or written nor material which has been accepted for the award of any other degree or diploma, except where due acknowledgement has been made in the text.

________________________(Signed)

___CHOY SIU HONG___(Name of student)

ABSTRACT

Perovskite lead-free ceramics bismuth sodium titanate ($Bi_{0.5}Na_{0.5}TiO_3$, BNT) modified with potassium and barium to form a new compound, $0.90Bi_{0.5}Na_{0.5}TiO_3$-$0.05Bi_{0.5}K_{0.5}TiO_3$- $0.05BaTiO_3$ (BNKBT-5), have been fabricated by a solid-state reaction method. The dielectric, piezoelectric and ferroelectric properties of the ceramics have been measured and the microstructures studied by X-ray diffraction and scanning electron microscopy. In the ferroelectric hysteresis loop measurements, a large remanent polarization (P_r ~ 28.5 $\mu C/cm^2$) and coercive field (E_c) ~3.5 MV/m have been observed. The electromechanical coupling coefficients k_p and k_t are 0.31 and 0.46, respectively. Those properties are comparable to that of lead-based ceramics such as lead zirconate titanate (PZT).

BNKBT-5 has relatively high dielectric loss (dissipation factor, tan δ ~2.7%), low mechanical quality factor (Q_M ~ 65 for radial mode) and low piezoelectric charge coefficient (d_{33} ~160 pC/N). To improve the properties of BNKBT-5, three different compounds have been used as additives/dopants. These include various amounts of cerium oxide (CeO_2), dicalcium ferrite ($Ca_2Fe_2O_5$) and bismuth lithium titanate ($Bi_{0.5}Li_{0.5}TiO_3$ (BLT)). All the samples with different compositions have been characterized. The measured dielectric, piezoelectric and ferroelectric properties are compared with that of undoped BNKBT-5. It has been found that the BNKBT-5 doped with 1.5 mole % of BLT, namely BNKLBT-1.5, has the best performance. It can enhance k_p, k_t, Q_M, P_r, and can reduce the dielectric loss tan δ but do not lower the depolarization temperature.

Two different types of devices have been fabricated using BNKBT-5 and BNKLBT-1.5 ceramic rings. The first type of device is compressive type accelerometers. A PZT accelerometer with similar structure has also been fabricated for comparison. The accelerometers are calibrated using a back-to-back calibration method against a standard reference accelerometer (Brüel & Kjær standard reference accelerometer Type 8305). Within the ±2.5% tolerance, the PZT accelerometer has a mean sensitivity value of 4.34 pC/ms^{-2} from 50 Hz to 8.24 kHz. The BNKBT-5 accelerometer has a mean value of 2.24 pC/ms^{-2} from 50 Hz to 10.1 kHz and the BNKLBT-1.5 accelerometer has a mean value of 2.97 pC/ms^{-2} from 50 Hz to 12.45 kHz. Although the PZT accelerometer has the highest sensitivity, but it has the lowest working frequency range. The BNKLBT-1.5 accelerometer has a reasonably high sensitivity and the broadest sensing frequency range which would be the most preferable choice for structural health monitoring applications.

The second type of device is ultrasonic wirebonding transducers for microelectronic packaging. It has been found that if titanium is used as the metal parts in the transducer, the BNKLBT-1.5 transducer has similar axial displacement (~1.6 μm) to that of PZT/stainless steel (which is the state-of-the-art transducer) transducer presumably because the lead-free ceramic has an acoustic impedance close to that of titanium metal. The lateral displacement of the BNKLBT-1.5 is much smaller than that of PZT transducer thus can improve the bonding quality. It shows that lead-free ceramics has the potential to replace PZT in certain transducer designs.

PUBLICATIONS

1. Wang, X. X., **Choy, S. H.**, Tang, X. G. and Chan, H. L. W. Dielectric Behavior and Microstructure of $(Bi_{1/2}Na_{1/2})TiO_3$ - $(Bi_{1/2}K_{1/2})TiO_3$ - $BaTiO_3$ Lead-free Piezoelectric Ceramics. *JOURNAL OF APPLIED PHYSICS*, 2005, 97, 104101.

2. **Choy, S. H.**, Wang, D. Y., Dai, J. Y., Chan, H. L. W. and Choy, C. L. Barium strontium zirconate titanate (BSZT) thin films for optical waveguide applications. *INTEGRATED FERROELECTRICS*, 2005, 80, 107.

3. **Choy, S. H.**, Wang, X. X., Chan, H. L. W. and Choy, C. L. $0.75(Bi_{1/2}Na_{1/2})TiO3\text{-}0.20(Bi_{1/2}K_{1/2})TiO_3\text{-}0.05BaTiO_3$ lead-free ceramics with addition of CeO_2. *FERROELECTRICS*, 2006, 336, 69.

4. **Choy, S. H.**, Wang, X. X., Chan, H. L. W. and Choy, C. L. Study of compressive type accelerometer based on lead-free BNKBT piezoceramics. *APPLIED PHYSICS A-MATERIALS SCIENCE & PROCESSING*, 2006, 82, 715.

5. **Choy, S. H.**, Wang, X. X., Chong, C. P., Chan, H. L. W., Liu, P. C. K. and Choy, C. L. $0.90(Bi_{1/2}Na_{1/2})TiO_3$ - $0.05(Bi_{1/2}K_{1/2})TiO_3$ - $0.05BaTiO_3$ transducer for ultrasonic wirebonding applications. *APPLIED PHYSICS A-MATERIALS SCIENCE & PROCESSING*, 2006, 84, 313.

6. Sun, C. L., Lam, K.H., **Choy, S. H.**, Chan, H. L. W., Zhao, X. Z. and Choy, C. L. High sensitivity cymbal-based accelerometer. *REVIEW OF SCIENTIFIC INSTRUMENTS*, 2006, 77, 036109.

7. **Choy, S. H.**, Li, H. K., Lam, K. H., Chan, H. L. W. and Choy, C. L. $(Bi_{1/2}Na_{1/2})TiO_3$ - $(Bi_{1/2}K_{1/2})TiO_3$ - $(Bi_{1/2}Li_{1/2})TiO_3$ - $BaTiO_3$ lead-free ceramic fibres fabricated by a powder-based extrusion method. *FERROELECTRICS*, 2006. (in press)

8. Xu, W. C., Lam, K. H., **Choy, S. H.** and Chan, H. L. W. A stepped Horn Transducer Driven by Lead-free Piezoelectric Ceramics. *INTEGRATED FERROELECTRICS*, 2006. (in press)

9. Edwards, G., **Choy, S. H.**, Chan, H. L. W., Scott, A. and Batten, A. Lead-free Transducer for Non-destructive Evaluation. *APPLIED PHYSICS A-MATERIALS SCIENCE & PROCESSING*, 2007. (in press)

10. **Choy, S. H.**, Wang, X. X., Chan, H. L. W. and Choy, C. L. Electromechanical and ferroelectric properties of $(Bi_{1/2}Na_{1/2})TiO_3$ - $(Bi_{1/2}K_{1/2})TiO_3$ - $(Bi_{1/2}Li_{1/2})TiO_3$ - $BaTiO_3$ lead-free piezoelectric ceramics. 2006. (submitted to JOURNAL OF ELECTROCERAMICS)

ACKNOWLEGEMENTS

I would first like to express my sincere gratitude to my chief supervisor Prof. H. L. W. Chan for her guidance and valuable advice. Thanks are extended to my co-supervisor Prof. C. L. Choy for his motivations, constant supports, understanding and helpful advice.

I would like to thank Dr. X. X. Wang for his stimulating comments on the ceramic modification technique and providing me with valuable suggestions.

Thanks are also due to staffs in the ASM research team including Dr. H. L. Li and Mr. C. P. Chong who have offered technical help in finite element analysis modelling and the transducer design. I have learnt much invaluable knowledge in wirebonding technology and product development from the team.

My thanks are also extended to my colleagues in our department for their assistance in material preparation and measurement techniques. They include (in no particular order): Dr. K. W. Kwok, Dr. K. H. Lam, Dr. D. Y. Wang, Dr. C. W. Tai, Dr. S. T. Lau, Mr. P. F. Lee, Mr. K. H. Ho and Mr. M. N. Yeung. Equipment support from the Center for Smart Materials and Materials Research Centre of the Hong Kong Polytechnic University is also acknowledged.

Last but not least, I truly appreciate the continual encouragement, supports and understanding from my family and from my best friends during my research study.

Without their supports, I could not finish my project smoothly.

TABLE OF CONTENTS

LIST OF FIGURE CAPTIONS

LIST OF TABLE CAPTIONS

CHAPTER 1 INTRODUCTION

1.1. MOTIVATION AND OBJECTIVES OF RESEARCH

Various types of piezoelectric materials have been extensively studied and widely used in different related devices since the discovery of piezoelectric effect in 1880 by J. and P. Curie. At present, lead-based perovskite structured piezoelectric materials, including lead titanate ($PbTiO_3$, PT), lead zirconate titanate ($Pb(Zr,Ti)O_3$, PZT) and lead magnesium niobate – lead titanate (PMN-PT) are dominating. They are commonly used in various applications such as filters, transducers and actuators. Lead-based perovskites contain over 60 wt% of lead and they have to be sintered at high temperature (commonly over 1200 ^oC). Since lead compound is volatile thus there is lead pollution during fabrication. In Europe, the legislation on waste electrical & electronic equipment (W.E.E.E.) has been issued and the use of hazardous substance such as lead in electrical parts (e.g. in solders) is prohibited from July, 2006. The search for alternative piezoelectric materials is now a very active research topic and a great deal of attention has been focused on different types of lead-free piezoelectric materials.

The research and development of lead-free materials generally included different categories: (1) Barium titanate (BT) based materials, (2) Tungsten-bronze (TB) structure; (3) Bismuth-layer (Bi-layer) structure; (4) Alkali niobate perovskite structure and (5) Bismuth-based perovskite structure. Both alkali niobate perovskite structure and bismuth-based perovskite structure have good piezoelectric properties which are good candidates for replacing lead-based perovskites. However, complicated procedures are required for fabricating dense, high quality alkali niobate ceramics which call for special forming methods (i.e. cold isostatic pressing, hot pressing) and sintering methods (e.g. spark plasma sintering). Those complicated procedures entail high cost and limit the popularization of this material in becoming a commercial product. Bismuth-based perovskite can be fabricated by a conventional method similar to that of the lead-based perovskite to achieve dense and good quality ceramics, which is more attractive to manufacturers. Although some of the properties in BNT-based materials are comparable with lead-based materials, some properties still have room for improvement. In this work, we will use a BNT-based ternary system, with the chemical formula $0.90(Bi_{0.5}Na_{0.5})TiO_3$ – $0.05(Bi_{0.5}K_{0.5})TiO_3$ – $0.05BaTiO_3$ (BNKBT-5), as the base material since this composition has good properties as found in our previous study. This material was modified by using different additives/dopants and their dielectric, piezoelectric and ferroelectric properties in different compositions were investigated.

Many researchers have studied modifications of the BNT-based materials, but very few reports are found on the applications of lead-free piezoelectric materials. In this study, the modified BNKBT-5 with good properties was chosen for piezoelectric device applications, including piezoelectric accelerometer (using the direct piezoelectric effect) and piezoelectric ultrasonic wirebonding transducer (using the converse piezoelectric effect). Lead-based PZT APC 840 (supplied by American Piezoceramics Ltd) was used as a reference for comparing the performance of the prototype devices.

1.2. SCOPE AND OUTLINE OF THESIS

The main objective of this thesis is to modify BNT-based lead-free piezoelectric ceramics by using additives/dopants for better dielectric, piezoelectric and ferroelectric properties. The performance of these lead-free ceramics in different device applications are then studied.

This thesis describes the fabrication of BNT-based bulk ceramics and reports the effect of different additives/dopants on this system. Characterizations of the ceramics with different compositions are also presented. Characterization of the prototype devices based on BNKBT-5 and BNKLBT-1.5 are given and compared with those devices based on PZT.

Following this brief introduction, a detail review on different lead-free piezoelectric ceramics is given in Chapter 2, including the structures and properties of each category mentioned in the previous section. The modification of each category is also summarised.

The procedures for fabricating BNT-based lead-free materials are described in

Chapter 3. Properties of BNKBT-5 and its modified compositions, including dielectric, piezoelectric and ferroelectric properties are also given.

Chapters 4 and 5 report the results in using lead-free ceramics for device applications. In Chapter 4, processing and characterization of a piezoelectric compressive-type accelerometer with PZT APC 840, BNKBT-5 and BNKLBT-1.5 ceramic rings as the transduction elements are given. In Chapter 5, a three-dimensional finite element model of an ultrasonic wirebonding transducer has been used to describe the transducer vibration characteristics. Prototype transducers with APC 840, BNKBT-5 and BNKLBT-1.5 ceramics rings as driving elements have been fabricated. The vibrational characteristics of the prototype transducers have been investigated and compared with the state-of-the-art transducer.

Conclusion and suggestions for future work on lead-free piezoelectric ceramics are given in Chapter 6.

1.3. ORIGINAL CONTRIBUTIONS

The original contributions reported in the present thesis are:

1. Lead-free ceramics BNKBT-5 was modified by using different additives/dopants, including cerium oxide (CeO_2), dicalcium ferrite ($Ca_2Fe_2O_5$) and bismuth lithium titanate ($Bi_{0.5}Li_{0.5}TiO_3$) and the two systems

have been systematically studied. The dielectric, piezoelectric and ferroelectric properties in each system with various additives/dopants amounts have been investigated and the optimum composition has been identified in each system.

2. Prototype piezoelectric compressive-type accelerometers have been fabricated. Two lead-free ceramics, BNKBT-5 and BNKLBT-1.5 have been used as the transduction elements and the performance of the accelerometers evaluated.

CHAPTER 2 LITERATURE REVIEW

2.1. INTRODUCTION

Piezoelectric materials find applications in a wide range of sensors, actuators and transducers that are important in diverse fields such as industrial process control, environmental monitoring, communications, information systems, medical instrumentation etc. The range of applications continues to grow and with it the demand for materials with improved performance, and for materials having tailored performance for specific applications.

Applied piezoelectric materials including natural and synthetic single crystals, bulk ceramics, ceramic thin films, multi-layer ceramics, polymer and ceramic/polymer composites. In recent years, there has been considerable research interest in exploring new lead-free materials with good ferroelectric or piezoelectric properties which can be used as an alternative to lead-based materials. The research and development of lead-free materials generally included different categories: (1) Barium titanate (BT) based materials, (2) Tungsten-bronze (TB) structure; (3) Bismuth-layer (Bi-layer) structure; (4) Alkali niobate perovskite structure and (5) Bismuth-based perovskite structure. The properties of the well-known lead-free materials, for example barium titanate (BT), are not as good as lead-based materials such as lead zirconate titanate

(PZT). Therefore in the literature, over the last decade, there have been more efforts to improve the properties of lead-free materials either by adding additive or by doping. Other than that, some novel routine such as single crystal growth or grain oriented growth ceramics greatly improve the performance. Apart from the above, only a small fraction of the literature has focused on lead-free devices.

This Chapter briefly described the fundamentals of ferroelectricity and piezoelectricity. A short review of the literature on the studies of lead-free materials was given to explain the structure-property relationship and finally focus on the recently developed devices using lead-free materials.

2.2. PIEZOELECTRICITY

The direct piezoelectric effect (from the Greek word “piezin”, meaning to press) was discovered by the brothers Pierre and Jacques Curie and first announced during the session of the Académie des Sciences in Paris on 2 August 1880 (Curie and Curie 1880). They reported the relationship between mechanical load and electric polarization but did not use the term piezoelectricity yet. The existence of converse piezoelectric effect was predicted using the thermodynamic consideration (Lippmann 1881). The now commonly used term “piezoelectricity” was first proposed by Hankel (Hankel 1881).

When a pressure is applied to a piezoelectric material, its crystalline structure produces a voltage proportional to the pressure (Jaffe et al. 1971) and this is the direct piezoelectric effect. Conversely, when an electric field is applied, its physical dimensions will change which is the converse piezoelectric effect. Perovskite types of piezoelectric materials commonly have an ABO_3 crystal structure as shown in Figure 2.1.

Piezoelectric ceramics have to be poled by applying a large electric field to align the dipoles in one direction. After poling, the ceramic material will become anisotropic. Piezoelectric effect allows the ceramic material to generate a voltage when it is subjected to a compressive or tensile force (Figure 2.2.)

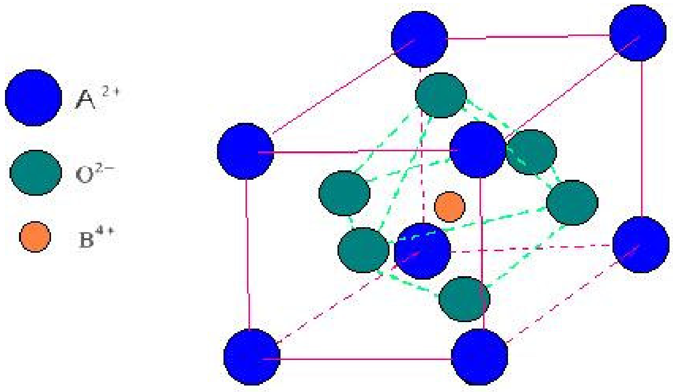

Figure 2.1 Perovskite crystal structure of (ABO_3).

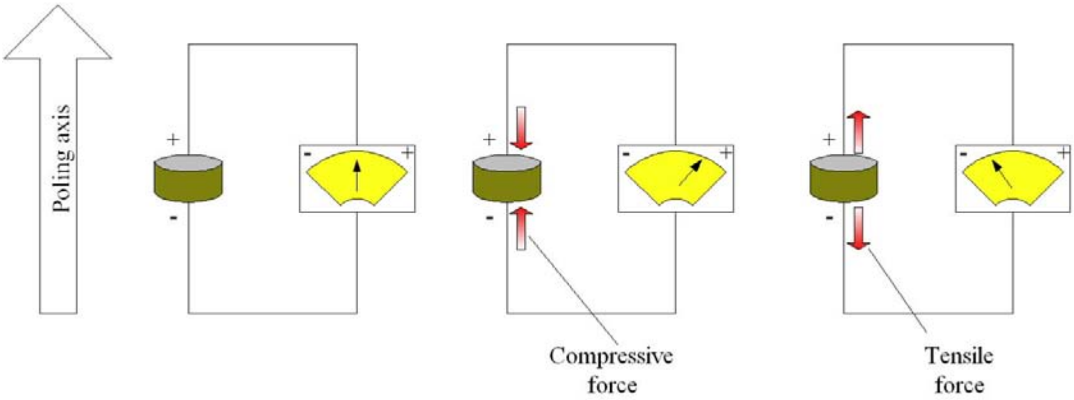

Figure 2.2 The direct piezoelectric effect.

The following two equations can be used to describe the electrical and mechanical variables in linear piezoelectric theory:

$$S_{ij} = s_{ijkl} X_{kl} + d_{mij} E_m \tag{2.1}$$

$$D_i = d_{ikl} X_{kl} + \varepsilon_o \varepsilon_{r_{ij}} E_j \tag{2.2}$$

where S_{ij} is the strain tensor component, s_{ijkl} the elastic compliance tensor component, X_{kl} the elastic stress tensor component, d the piezoelectric coefficient tensor component, E (E_j, E_m) the electric field tensor component, Di the dielectric displacement tensor component, ε_o the permittivity of free space and $\varepsilon_{r_{ij}}$ is the relative permittivity of the ceramic material. The first equation describes the converse piezoelectric effect and the second equation describes the direct piezoelectric effect (Hom et al. 1994).

2.3. FERROELECTRICITY

Crystals can be classified into 32 point groups. These point groups can be divided into two classes: with and without a centre of symmetry. There are 21 point groups that do not have a centre of symmetry and 20 of these point groups are piezoelectrics. The relationship between ferroelectrics and piezoelectrics is shown in Figure 2.3. Thus it is seen that all pyroelectrics are piezoelectric while all ferroelectrics are pyroelectric, but the reverse may not be true (Jaffe et al. 1971).

A ferroelectric material exhibits a spontaneous polarization in the absence of an electric field and this polarization may be switched by the application of an external electric field (Mitsui et al. 1976). An important feature of ferroelectric materials is the ferroelectric hysteresis (or P-E) loop, i.e., the polarization P is a double-valued function of the applied electric field E. A typical P-E hysteresis loop in ferroelectrics is shown in Figure 2.4.

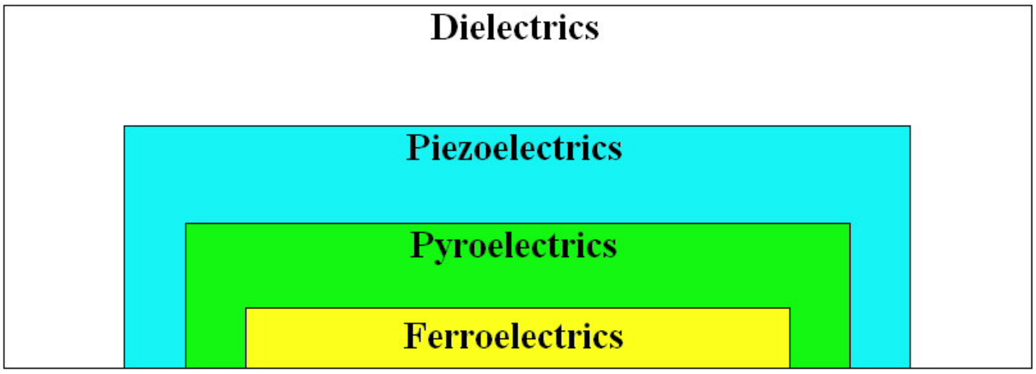

Figure 2.3 The relationship among dielectrics, piezoelectrics, pyroelectrics and ferroelectrics.

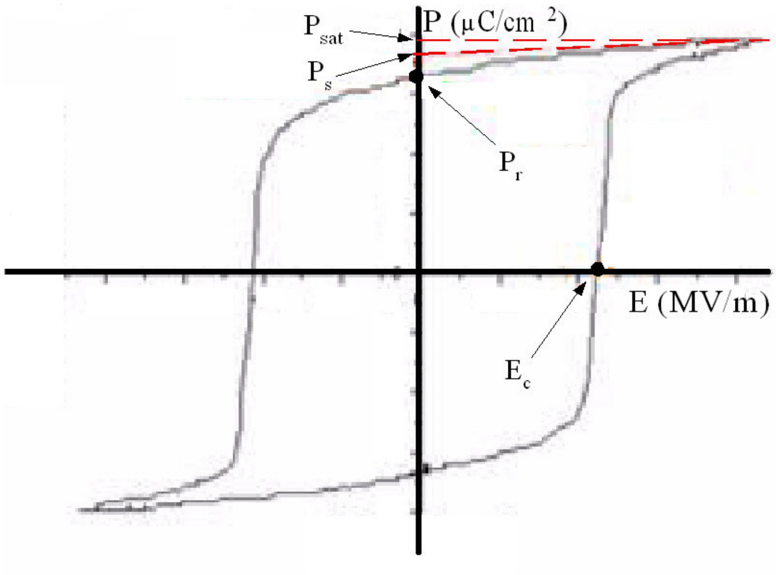

Figure 2.4 A typical ferroelectric hysteresis loop.

Polarization is the dipole moments per unit volume of the crystalline aggregate. In a poled ceramics or single domain crystal there is a net remnant polarization P_r. Values of the spontaneous polarization P_s can be observed by extrapolating the polarization at the highest field Psat back to the field axis along a tangent. The remnant polarization P_r in a crystal cannot be removed until an applied field in the opposite direction reaches a certain value. The strength of the field required to reduce the polarization P to zero is called the coercive field strength E_c.

Another important characteristic of ferroelectrics is the temperature of the phase transition call the Curie point T_c. When temperature decreases through the Cuire point, a ferroelectric crystal undergoes a structural phase transition from the paraelectric phase to the ferroelectric phase. When the temperature is above T_c the crystal does not exhibit ferroelectricity. On the other hand, when the temperature falls below T_c, the crystal exhibits ferroelectricity.

2.4. LEAD-FREE PIEZOELECTRIC MATERIALS

2.4.1. BARIUM TITANATE BASED MATERIALS

Barium titanate with the chemical formula $BaTiO_3$ (abbreviated as BT) was discovered in the 1940's. It was the first perovskite ceramics that found to be ferroelectric, and later on the first piezoelectric ceramic. Its Curie temperature is ~130^{o}C. It is widely used as capacitor material, but for piezoelectric applications the low T_c is a limitation, and it is basically substituted by PZT. Table 2.1 shows some of the important parameters of $BaTiO_3$.(Herbert 1982) and Figure 2.5 shows the change of structure in

BT with temperature.

Table 2.1 Some important parameters of BaTiO3 (Jaffe et al. 1971)

Curie Temperature T_c (^oC)	130
Density (kg/m^3)	5700
Relative permittivity ε_r (at 1 kHz)	1700
Dielectric loss tanδ (at 1 kHz)	0.01
Piezoelectric d_{33} coefficient (pC/N)	190
Piezoelectric d_{31} coefficient (pC/N)	-78
Electromechanical coupling coefficient k_{33}	0.49
Remnant polarization P_r ($\mu C/cm^2$)	13.3

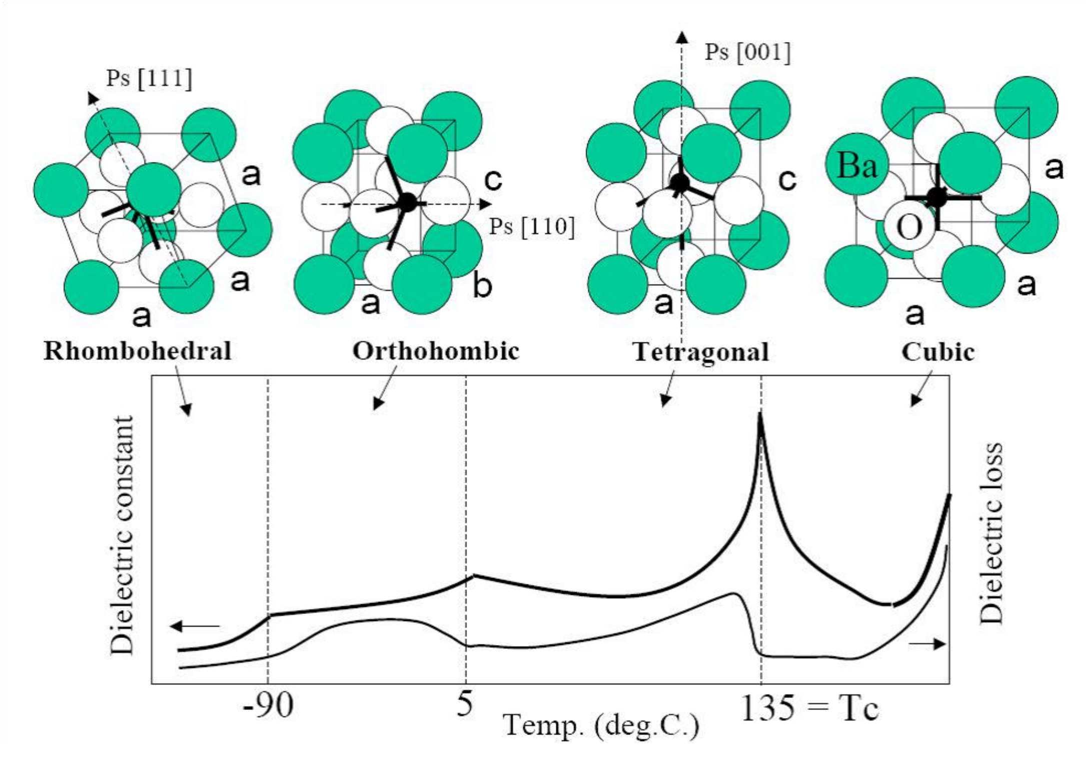

Figure 2.5 The structural change of $BaTiO_3$ with temperature (Kusumoto 2005).

As the low Curie temperature T_c of $BaTiO_3$ limited its piezoelectric application, shifting T_c to a higher temperature is one of the considerations. The properties of $BaTiO_3$ can be modified by using different additive and doping. The ferroelectric and piezoelectric properties can be improved by doping zirconium ion to form $Ba(Ti_{1-x}Zr_x)O_3$ (0>x>0.3) (Yu *et al.* 2002). For x = 0.05, the remnant polarization P_r, electromechanical coupling factor, k_{33}, and piezoelectric constant, d_{33}, are 13.3 C/cm^2, 0.565 and 236 pC/N, respectively. Barium titanate can also be modified by both adding zirconium and strontium ions with the chemical formula $Ba_{0.95}Sr_{0.05}Ti_{0.95}Zr_{0.05}O_3$ (BSZT) (Xu *et al.* 2006). Good piezoelectric properties have been found (d_{33} = 220 pC/N, $k_t = k_p$ =0.49) and it has been used in a stepped horn transducer application which produces performance comparable with PZT transducer. In addition, Takahashi et al reported that the piezoelectric d_{33} coefficient of pure barium titanate can be greatly enhanced by using microwave sintering (Takahashi *et al.* 2006). Barium titanate can also be used as dopant material in both bismuth-based perovskite structure and niobate-based perovskite structure materials. The review of those compositions will be presented in the following sections.

2.4.2. LEAD-FREE MATERIALS WITH TUNGSTEN-BRONZE (TB) STRUCTURE

The tungsten bronze ceramics have a general formulation $(A1)_2(A2)_4(C)(B)_{10}O_{30}$. Large cations (e.g. Na^+, K^+, Sr^{2+}, Ba^{2+}, Pb^{2+}, La^{3+}, Bi^{3+}, ...) occupy the 15 co-ordination number (C.N.) [A1] and the 12 C.N. [A2] sites, small cations like Li^+ are in the 9 C.N. [C] sites and small and highly charged cations (e.g. Nb^{5+}, Ta^{5+}, ...) are in the octahedral [B] sites. Tungsten bronze solid solutions can be obtained with either tetragonal (*4mm*) symmetry in the ferroelectric phase or orthorhombic (*mm2*) symmetry, which can be both ferroelectric and ferroelastic (Lines and Glass 1977). The polar unit of tungsten bronze compounds is the NbO_6 octahedron, and the polar axis of tetragonal bronzes is parallel to the c-axis or [001](Lines and Glass 1977). Figure 2.6 shows the structure of $Ba_2NaNb_5O_{15}$. $BaBiNb_5O_{15}$ was one of the candidates in this system which exhibits relaxor ferroelectric properties that has maximum relative permittivity at 295 K (Simon and Ravez 2003). Neurgaonkar et al. (Neurgaonkar *et al.* 1985; Neurgaonkar *et al.* 1987; Neurgaonkar *et al.* 1988a; Neurgaonkar *et al.* 1988b; Neurgaonkar *et al.* 1988c; Neurgaonkar 1989) have systematically investigated tungsten bronze ferroelectric crystals and demonstrated encouraging piezoelectric properties in such compounds. $(1-x)Sr_2NaNb_5O_{15}-(x)\ CaNaNb_5O_{15}$ system is one of the most promising materials with tungsten bronze structure having good piezoelectric properties. Xie et al (Xie and Akimune 2002; Xie *et al.* 2002a; Xie *et al.* 2002b) successfully fabricated

$Sr_{2-x}Ca_xNaNb_5O_{15}$ system (abbreviated SCNN) with over 97% relative density by using a spark plasma sintering technique. SCNN system with the composition x = 0.15 exhibited the highest ferroelectric and piezoelectric properties, where the remnant polarization (P_r), piezoelectric d_{33} constant, electromechancial coupling coefficients k_p and k_t are $9.1\mu C/cm^2$, 96pC/N, 0.344 and 0.081, respectively. In the meantime, Matsuo, K. et al. reported a dense $Sr_{2-x}Ca_xNaNb_5O_{15}$ (x = 0.1) ceramics with good piezoelectric properties (Matsuo *et al.* 2002), and the properties can be improved by lanthanum oxide doping (1 wt% La_2O_3). The radial-mode and thickness-mode electromechanical coupling coefficient, k_p and k_t, are 0.137 and 0.386 for the undoped sample, and 0.096 and 0.42 for the La-doped sample. The average piezoelectric constant d_{33} is 119 pC/N for the undoped sample, and it increases to 138 pC/N for La-doped sample. Barium doped $Sr_2NaNb_5O_{15}$ single crystal has also been reported to have high electromechanical coupling k_{33} coefficient of 0.57 (Jiang *et al.* 2005).

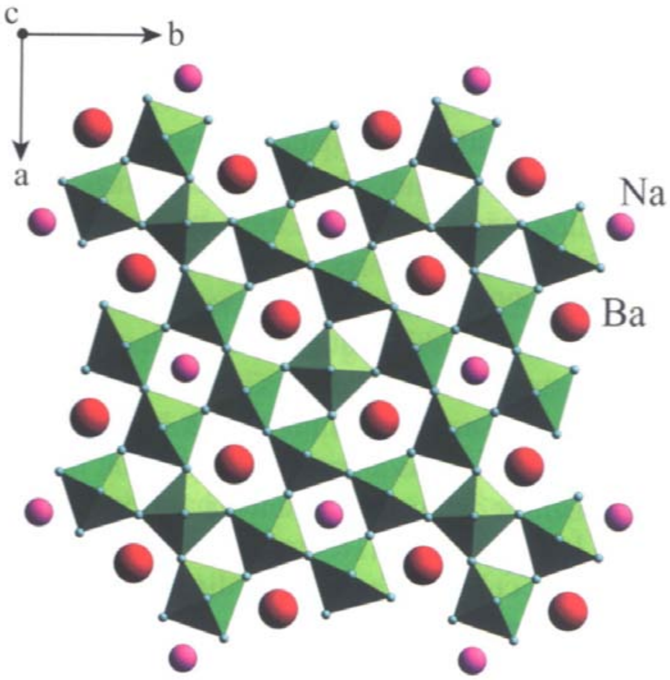

Figure 2.6 The structure of tetragonal tungsten bronzoid $Ba_2NaNb_5O_{15}$ (Mitchell 2002).

2.4.3. BISMUTH-LAYER (BI-LAYER) STRUCTURE

The bismuth layered derivatives of the perovskite structure were first described by Aurivillius (Aurivullius 1949). This structure can generally be represented by the following formula: $(Bi_2O_2)^{2+}$ $(A_{m-1}B_mO_{3m+1})^{2-}$, where A is a combination of one or more mono-, di- and trivalent ions and B is a combination of tetra, penta and hexavalent ions, and the integer m takes any value from 1 to 5 (Figure 2.7). The bismuth oxide layer have structures based on corner linked perovskite-like sheets, separated by bismuth oxide $(Bi_2O_2)^{2+}$ layers. Bismuth layer-structured ferroelectrics (BLSFs) have been studied continually by a lot of researchers since 1950s (Subbarao 1962a; Subbarao 1962b;

Aparna *et al.* 2002). Due to its structure interleaved with pseudo-perovskite blocks along the c axis, the BLSFs usually have a long c axis where the remnant polarization P_r originated.

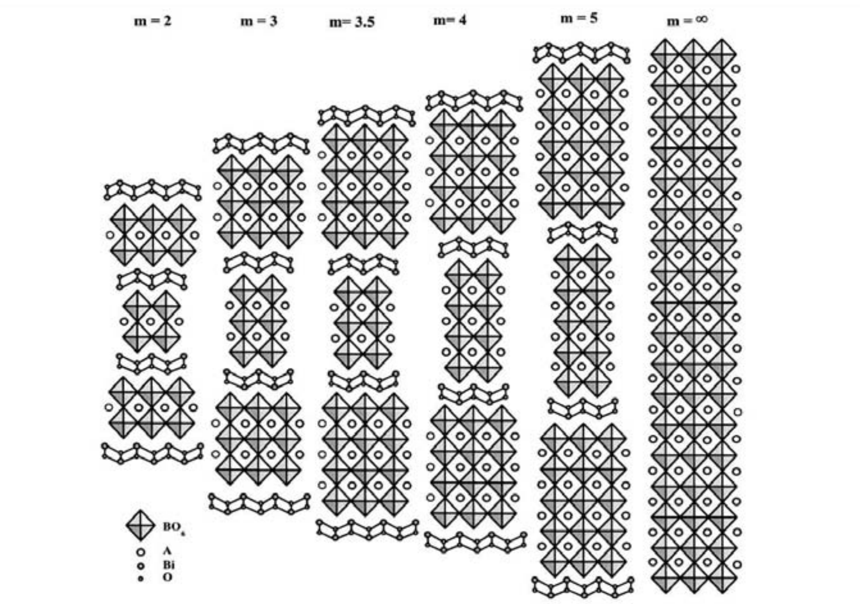

Figure 2.7 The general representation of bismuth-layered structure (Sanson and Whatmore 2002).

In BLSFs, Ti^{4+} ion is mostly occupies the B-site of $(Bi_2O_2)^{2+}(A_{m-1}B_mO_{3m+1})^{2-}$ with $(M^{2+}{}_{1/3}Bi^{3+}{}_{2/3})$ at the A-site. When m equals to 4, $(Bi_2O_2)^{2+}(A_{m-1}B_mO_{3m+1})^{2-}$ becomes $MBi_4Ti_4O_{15}$, where M can be Ca^{2+}, Ba^{2+}, Sr^{2+}, etc. $MBi_4Ti_4O_{15}$-based piezoelectric ceramic is one of the most important bismuth layer-structured piezoelectric ceramics, the patents on it is near 40% of those for all the bismuth layer-structured piezoelectric ceramics (Lin *et al.* 2003). $SrBi_4Ti_4O_{15}$ (SBT), $CrBi_4Ti_4O_{15}$ (CBT) and $BaBi_4Ti_4O_{15}$

(BBT) have been widely studied in previous years due to its relatively good ferroelectric properties. Many researchers have been working on modifying SBT (Hirose *et al.* 1999; Oka *et al.* 2000; Ogawa 2004), CBT (Lin *et al.* 2003) and BBT (Miranda *et al.* 2001) by adding different ions (e.g. Ca^{2+}, La^{3+} and Sm^{3+} ion), additives (e.g. MnO_2, Cr_2O_3) or mixed BLSFs systems to achieve a better ferroelectric and/or piezoelectric properties.

Other than the $MBi_4Ti_4O_{15}$ systems, bismuth titanate is also an important candidate in BLSFs as it is a typical ferroelectric material with useful properties for optical memory, piezoelectric and electro-optic devices. Figure 2.8 shows the structure of $Bi_4Ti_3O_{12}$ (m=3). It also has an Aurivillius structure and the symmetry is pseudotetragonal. The crystal structure of $Bi_4Ti_3O_{12}$ can be described as a stacking of layers of Bi_2O_2 and $Bi_2Ti_3O_{10}$ along the c axis. In the $Bi_2Ti_3O_{10}$ units, Ti ions are enclosed by oxygen octahedrons, which are linked through corners forming O-Ti-O linear chains. Bi ions occupy the spaces in the framework of TiO_6 octahedrons. Thus, $Bi_2Ti_3O_{10}$ units possess a remarkable similarity to the perovskite-type structure. The height of the perovskite-type layer sandwiched between Bi_2O_2 layers in $Bi_4Ti_3O_{12}$ is equal to six Ti-O distance or approximately equals to three ABO_3 perovskite units (Subbarao 1961; Subbarao 1962a).

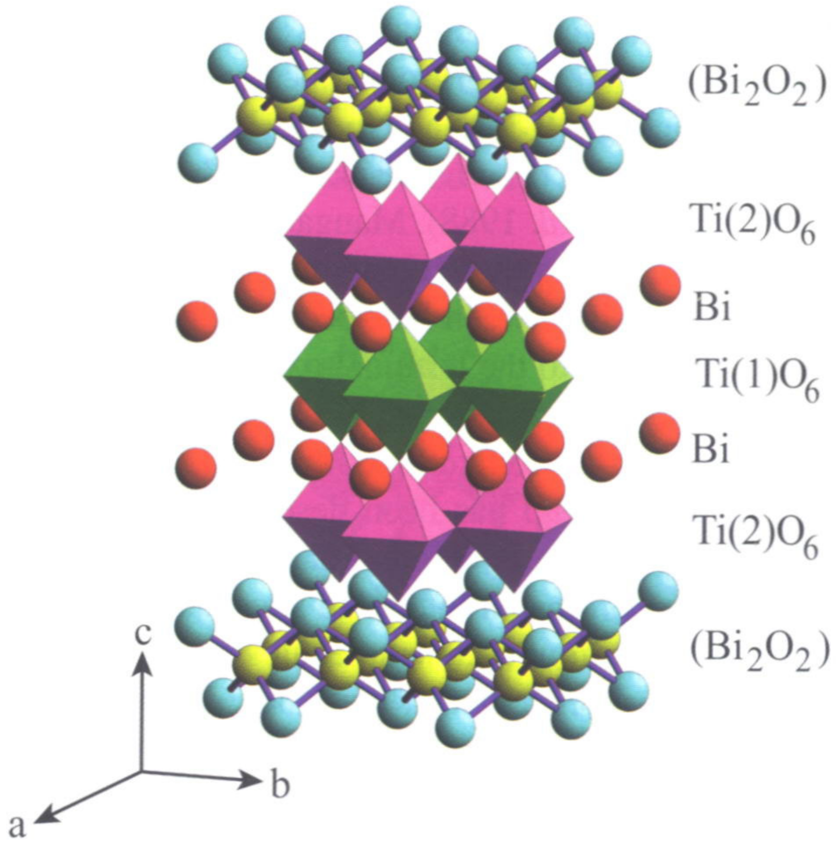

Figure 2.8 Structure of $Bi_4Ti_3O_{12}$ (Mitchell 2002).

Bismuth titanate has a low relatively permittivity and high Curie temperature (T_c = 948K, (Jovalekic *et al.* 1998)), which can have a broarder temperature range for stable properties, compared with other ferroelectric materials such as lead zirconate titanate and barium titanate which can be a potential candidate for memory devices, ceramics capacitors, piezoelectric transducers, sensors, high-density dynamic random access memories (DRAMs), nonvolatile memories and other high temperature applications.

2.4.4. NIOBATE-BASED PEROVSKITE STRUCTURE

The research on alkali niobate perovskite structure is mainly focusing on sodium niobate ($NaNbO_3$) and potassium niobate ($KNbO_3$). Matthias and Remeika have studied the dielectric properties of both single crystal and concluded that both are ferroelectric materials (Matthias and Remeika 1949).

Potassium niobate has the same sequence of phase changes as barium titanate during cooling: cubic, tetragonal, orthorhombic, rhombohedral, but with all the transition temperatures occur at higher temperature. The Curie temperature of $KNbO_3$ is 435 ^{o}C and the space group is ***2mm*** at room temperature which is an orthorhombic ferroelectric form.

Compared with potassium niobate, sodium niobate is having a more complicated phase transition (Lefkowitz ***et al.*** 1966; Sakowski-Cowley ***et al.*** 1969; Darlington and Megaw 1973). The room temperature form of $NaNbO_3$ is orthorhombic antiferroelectric, space group ***Pbam*** with the c axis 4 times the simple perovskite cell edge, and a and b axes rotated 45^{o} with respect to the simple cell (Jaffe ***et al.*** 1971), the structure is shown in Figure 2.9.

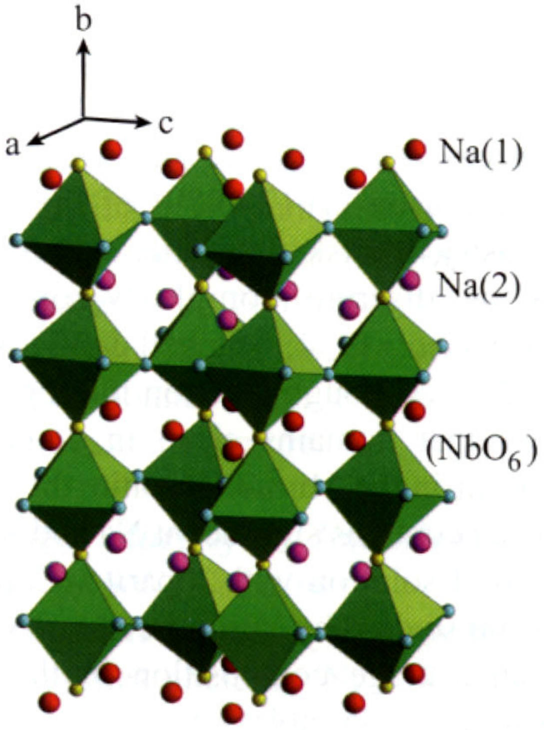

Figure 2.9 Clinographic representation of the structure of $NaNbO_3$ at room temperature (after (Sakowski-Cowley *et al.* 1969)) (Mitchell 2002).

The solid solution of $NaNbO_3$ and $KNbO_3$ is a very complicated system, which have some compositional phase boundaries detectable by X-ray diffraction or calorimetry. The detail phase diagram of $NaNbO_3$ – $KNbO_3$ is shown in Figure 2.10. The piezoelectric properties are more or less the same as $PbZrO_3$ – $PbTiO_3$ system. The piezoelectric properties have a maximum near the $(Na_{0.5}K_{0.5})NbO_3$ (namely NKN) composition. But due to the significant volatility of K_2O from phases other than $KNbO_3$, or the potassium niobate not having 1:1 ratio, the final product may not be in stoichiometric composition. So it is very difficult to obtain dense and stoichiometric

$(Na_{0.5}K_{0.5})NbO_3$ sample by using conventional sintering method. In early years, using hot press is a solution to produce dense NKN sample, and in recent years the spark plasma sintering (SPS) method is an alternative. Table 2.2 shows the characteristics of NKN ceramics with different fabrication methods. It is easy to observe that dense samples fabricated by either hot-pressing or SPS technology have better piezoelectric properties than the one fired in air.

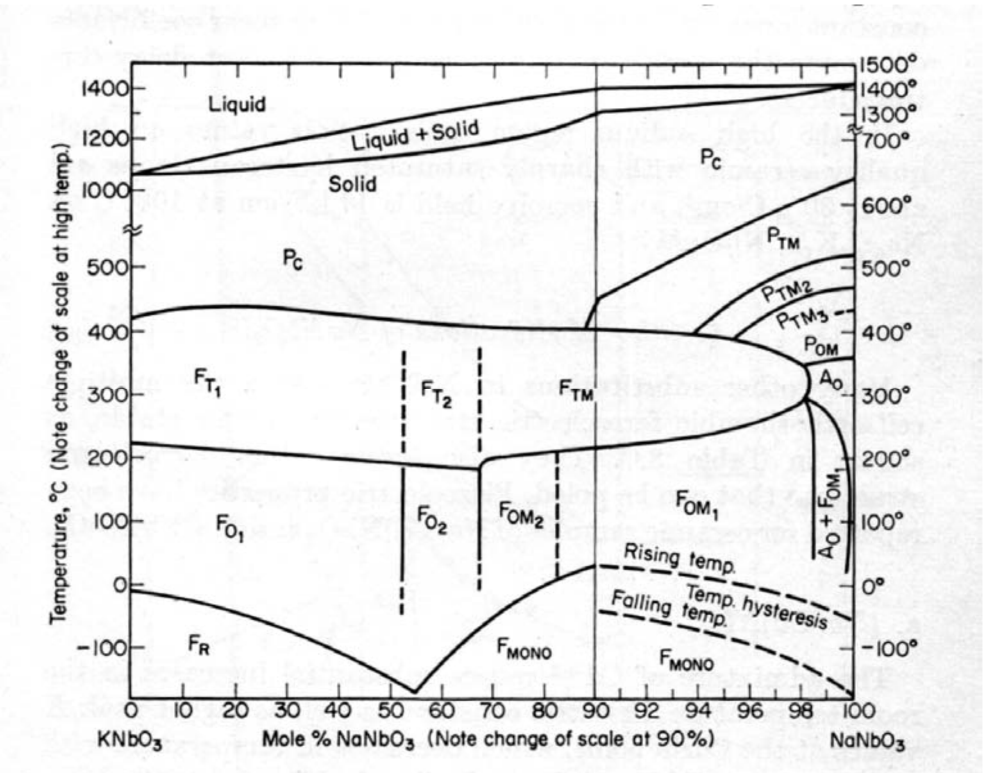

Figure 2.10 Phase diagram of the system $NaNbO_3$ – $KNbO_3$ (Jaffe *et al.* 1971).

Table 2.2 Characteristics of (Na, K)NbO$_3$ ceramics at room temperature.

	$(Na_{0.5}K_{0.5})NbO_3$ Air-fired (Jaeger and Egerton 1962)	$(Na_{0.5}K_{0.5})NbO_3$ Hot-pressed (Jaeger and Egerton 1962)	$(Na_{0.5}K_{0.5})NbO_3$ SPS (Li *et al.* 2006)	$(Na_{0.5}K_{0.5})NbO_3$ Attrition-milling (Zuo *et al.* 2006)
Dielectric constant	290 (100kHz)	420 (100kHz)	606 (1kHz)	605(1kHz)
Dielectric loss tanδ	2% (100kHz)	1.4% (100kHz)	3.6% (1kHz)	4.36% (1kHz)
Density (kg/m^3)	4250	4460	4470	4440
d_{33} (pC/N)	~80	160	148	102
k_p	0.36	0.45	0.39	0.38

As the sintering condition of sodium potassium niobate is very critical thus the repeatability and the yield is low. By the assistance of doping and/or additives, the sintering window of the sodium potassium niobate could be broaden and dense samples with good properties can be easier to obtain. Many work have been done in the recent years, Guo et. al. suggested different dopants including barium titanate BaTiO$_3$ (Guo *et al.* 2004c), lithium niobate LiNbO$_3$ (Guo *et al.* 2004b) , strontium titanate SrTiO$_3$ (Guo *et al.* 2004a) and lithium tantalate LiTaO$_3$ (Guo *et al.* 2005) and results are summarised in Table 2.3. The LiNbO$_3$ doped NKN seems to have the best piezoelectric properties over the other dopings. But the drawback of the NKN system is that the dielectric loss is relatively high. For pure NKN, the dielectric loss (tan δ) is over 6% at room temperature at 10 kHz and reduced to over 3% loss in the best doped composition in the doping.

Table 2.3 Summary of the properties of NKN doped with different compounds by Guo et. al..

Chemical formula	Best composition	d_{33} (pC/N)	k_t	k_p
Pure NKN	-	98	0.38	0.295
(1-x) NKN – x $LiTaO_3$	x = 0.05	~ 200	-	~ 0.36
(1-x) NKN – x $LiNbO_3$	x = 0.06	~ 235	0.48	0.42
(1-x) NKN – x $BaTiO_3$	x = 0.02	104	0.38	0.29
(1-x) NKN – x $SrTiO_3$	x = 0.005	96	0.438	0.325

Another breakthrough in NKN system was reported in Nature in 2004 by Saito et. al. (Saito *et al.* 2004). $(Na_{0.5}K_{0.5})NbO_3$ was added with hexagonal pseudo-ilmenite-type $LiTaO_3$ to form a morphotropic phase boundary (MPB) and also based on the Cohen’s calculation (Cohen 1992) for the titanate perovskite system to exploit the hybridization of covalency onto ionic bonding for further improvement in piezoelectricity. In addition to $LiTaO_3$, $LiSbO_3$ was used as an end member for the compositional study with $(Na_{0.5}K_{0.5})NbO_3$, because the higher electronegativities of Sb and Ta compared to Nb were expected to make the alkaline niobate-based perovskite more covalent. A pseudo-ternary system $Na_{0.5}K_{0.5}NbO_3$ – $LiTaO_3$ – $LiSbO_3$, namely LF4, was formed and the reported Curie temperature is 253°C and the piezoelectric d_{33} constant is about 300 pC/N using normal fabrication method. The performance of the ceramics can be further improved by using a reactive-templated grain growth (RTGG) route, textured polycrystal of LF4 was formed, namely LF4T. The Lotgering’s factor of the LF4T in the <001> orientation is 91% and the d_{33} factor has been raised to 416 pC/N, which is comparable with PZT ceramics and BNBT single crystal. The detail comparison between LF4T and PZT is listed in Table 2.4. To fabricate textured ceramics with high d_{33} values, the most important technologies is the preparation of plate-like template particles. However, the grain oriented routine is not commonly used in industrial production.

Table 2.4 Piezoelectric properties of LF4T and PZT (Saito *et al.* 2004)

	LF4T	PZT4
Curie Temperature T_c (^oC)	253	250
Relative permittivity ε_r (at 1 kHz)	1570	2300
Piezoelectric d_{33} coefficient (pC/N)	416	410
Piezoelectric d_{31} coefficient (pC/N)	152	170
Piezoelectric g_{33} coefficient (mV・m / N)	29.9	20.2
Piezoelectric g_{31} coefficient (mV・m / N)	11.0	8.3
Electromechanical coupling coefficient k_p	0.61	0.60
Normalized strain, Smax/Emax, (pm/V)	750	700

2.4.5. BISMUTH-BASED PEROVSKITE STRUCTURE

The bismuth-based perovskite lead-free materials is based on bismuth sodium titanate $(Bi_{0.5}Na_{0.5})TiO_3$ (BNT). Smolenskii et al. discovered BNT in 1961 (Smolenskii *et al.* 1961) and reported that BNT exhibits a relatively large remnant polarization P_r = 38μC/cm^2 and coercive field E_c = 7.3MV/m at room temperature. It also has a rhombohedral structure at room temperature with a high Curie temperature (T_c =

320^{o}C) (Suchanicz *et al.* 1988). But due to its large coercive field and relatively high conductivity, pure BNT is hard to pole thus the piezoelectric properties are not good enough. Another important bismuth-based perovskite material is bismuth potassium titanate, $(Bi_{0.5}K_{0.5})TiO_3$ (BKT), which is a typical ferroelectric material with tetragonal structure at room temperature and has a higher Curie temperature (T_c = 380^{o}C) (Buhrer 1962) than BNT. BKT has a remnant polarization P_r = 22.2 C/cm^2 and coercive field E_c = 5.25 MV/m at room temperature. The crystal structure of BKT ceramic was studied by Ivanova et al.(Ivanova *et al.* 1962) by X-ray diffraction, which is shown in Figure 2.11. Table 2.5 summarises the properties of pure BNT and pure BKT.

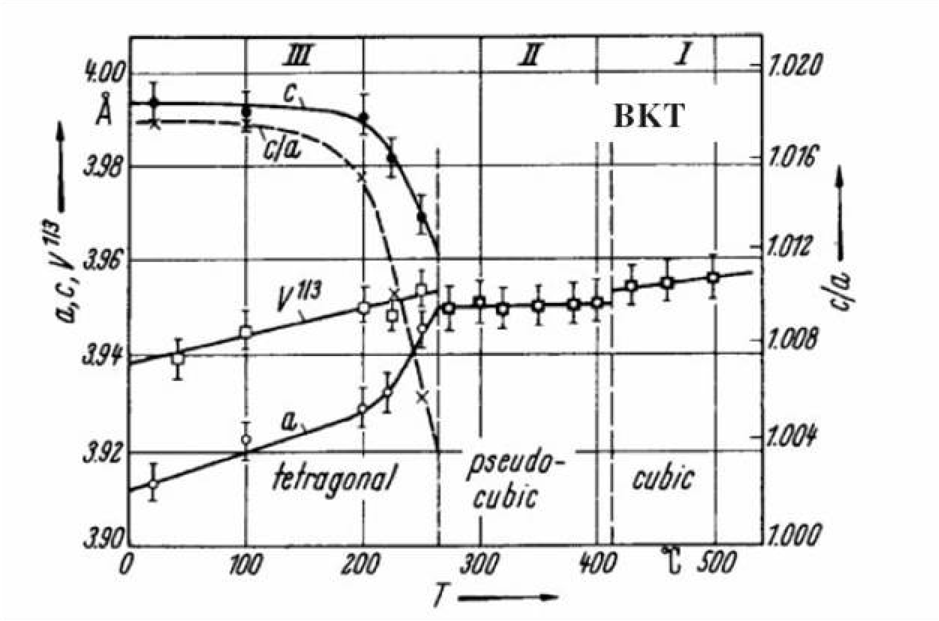

Figure 2.11 The temperature dependence of lattice constant a and c of BKT reported by Ivanova et al. (Ivanova *et al.* 1962).

Table 2.5 Some properties of pure $(Bi_{0.5}Na_{0.5})TiO_3$ and$(Bi_{0.5}K_{0.5})TiO_3$.

	ε_r	tanδ	k_{33}	d_{33} (pC/N)	P_r (μC/cm2)	E_c (MV/m)
$(Bi_{0.5}Na_{0.5})TiO_3$ (Jaffe *et al.* 1971)	300	1.1	0.4	70	38	7.3
$(Bi_{0.5}K_{0.5})TiO_3$ (Hiruma *et al.* 2005)	517	7.1	0.28	69.8	22.2	5.25

Due to the environmental concern of lead pollution since 1990s, BNT becomes an important group of lead-free ceramics which is a potential candidate to replace lead-based ceramics. Many work have been carried out to improve the properties of BNT. The most important work is to reduce the conductivity of BNT and this could be solved by using dopings and additives. Takanaka et. al. firstly report the $(1-x)(Bi_{0.5}Na_{0.5})TiO_3 – (x) BaTiO_3$, namely BNBT-100x, system in 1991 (Takanaka *et al.* 1991). As pure BNT has a rhombohedral structure and $BaTiO_3$ has a tetragonal structure at room temperature, the solid solution of the two ceramics forms the MPB when x=0.06. The detail phase diagram is shown in Figure 2.12. Similar to other systems; the formation of MPB can greatly improve the piezoelectric properties of the solid solution. Similar work on BNBT system has been done by different research groups (Kaewkamnerd *et al.* 1997; Chu *et al.* 2000; Chu *et al.* 2002; Cho *et al.* 2004; Gomah-Pettry *et al.* 2004; Zhao *et al.* 2004; Wang *et al.* 2005c). Other than $BaTiO_3$ (BT), different materials were used as dopants in pure BNT to form binary systems, including $(Bi_{0.5}K_{0.5})TiO_3$ (BKT) (Sasaki *et al.* 1999) , $NaNbO_3$ (Takenaka *et al.* 1997), $Bi_2O_3 \cdot Sc_2O_3$ (Nagata and Takanaka 1997), $BiFeO_3$ (Nagata *et al.* 1999), $Ba(Cu_{0.5}W_{0.5})O_3$ (Wang *et al.* 2003a) and etc.. The effect of additives on pure BNT system and on the binary systems has also been widely investigated. Table 2.6 gives a brief summary on the work.

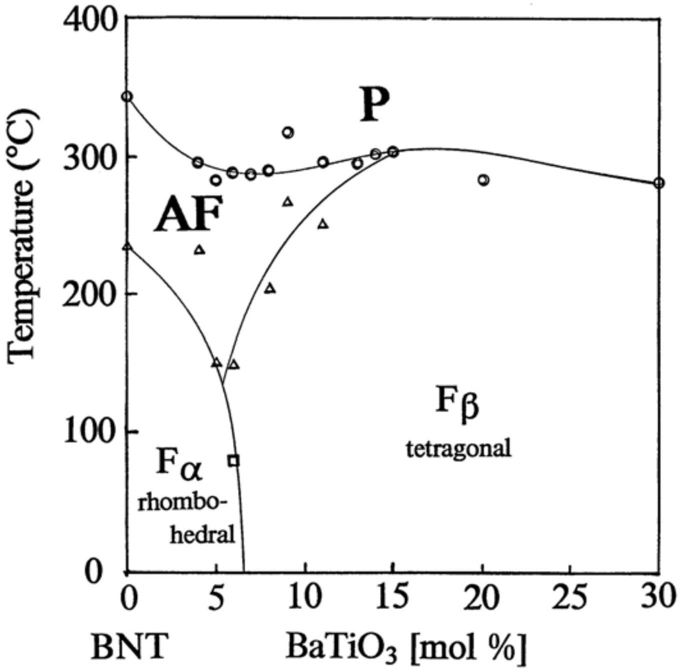

Figure 2.12 Phase relationship among $(Bi_{0.5}Na_{0.5})TiO_3$ and $BaTiO_3$ in the $(Bi_{0.5}Na_{0.5})_{1-x}$ Ba_xTiO_3 (BNBT-100x) system. (F_α: Ferroelectric rhombohedral phase, F_β: ferroelectric tetragonal phase, AF: antiferroelectric phase, P paraelectric phase).

Table 2.6 Properties of some reported BNT binary systems and systems with additives.

Compositions reported	ε_r	tanδ	k_{33} or k_t	k_p	d_{33} (pC/N)	P_r (μC/cm^2)	E_c (MV/m)
$(Bi_{0.51}Na_{0.51})Sc_{0.02}Ti_{0.98}O_3$ (Nagata and Takanaka 1997)	431	5.11	k_{33}=0.418	0.144	74.7	33.41	4.24
0.997BNT – 0.03 $NaNbO_3$ (Takenaka *et al.* 1997)	-	-	k_{33}=0.43	~0.1	71	33	4.25
BNT + 0.5 wt% MnO_3 (Kaewkamnerd *et al.* 1997)	524	-	k_{33}=0.536	0.289	-	-	-
$Bi_{0.5}(Na_{0.8}K_{0.2})_{0.5}TiO_3$ (Sasaki *et al.* 1999)	1030	2	k_t =0.418	0.27	-	19.9	-
0.995 BNT – 0.05 Ba $(Cu_{0.5}W_{0.5})O_3$ (Wang *et al.* 2003a)	328	1.5	-	0.181	-	-	-
BNBT6+ 0.4wt% CeO_2 (Wang *et al.* 2003b)	653	1.2	-	0.34	152	37.7	3.7
BNBT6 + 0.5 mol% CeO_2 + 0.5 mol% La_2O_3 (Wang *et al.* 2005a)	831	2.0	-	-	162	~38	~3.5
BNBT6 + 1 at.% La^{3+} (Li *et al.* 2004)	1576	4.5	k_t =0.38	0.24	118	-	-
BNBT6 + 1 at.% Nb^{5+} (Li *et al.* 2004)	1614	4.6	k_t =0.38	0.20	118	-	-
BNBT6 + 1 at.% Co^{3+} (Li *et al.* 2004)	1200	2.3	k_t =0.46	0.27	139	-	-

The improvement in piezoelectric properties, other than the formation of MPB, is related to the reduction in conductivity so the BNT samples can be fully poled. Based on the studies of BNT-based binary systems, many researchers started to investigate different BNT-based ternary systems. Those systems are generally based on the $(Bi_{0.5}Na_{0.5})TiO_3$ – $BaTiO_3$ and $(Bi_{0.5}Na_{0.5})TiO_3$ –$(Bi_{0.5}K_{0.5})TiO_3$ systems. Table 2.7 listed some important ternary systems.

Table 2.7 Properties of some BNT-based ternary solid solution systems.

Compositions reported	ε_r	tan δ	k_{33} or k_t	k_p	d_{33} (pC/N)	P_r ($\mu C/cm^2$)	E_c (MV/m)
$0.99(Bi_{0.5}Na_{0.5})TiO_3$ – 0.05KNbO3 – 0.05 $(0.5(Bi_2O_3 \cdot Sc_2O_3)$ (Nagata and Takenaka 1998)	483	5.12	k_{33}= 0.434	0.166	82.1	-	-
$0.852(Bi_{0.5}Na_{0.5})TiO_3$ – $0.028BaTiO_3$ – $0.12(Bi_{0.5}K_{0.5})TiO_3$ (Nagata *et al.* 2003)	1141	-	k_{33}= 0.56	0.33	191	-	-
$0.95(Bi_{0.5}Na_{0.5})TiO_3$ – $0.03NaNbO_3$ – 0.02 $BaTiO_3$ (Wu *et al.* 2003)	1050	~5	k_t = 0.52	-	110	-	-
$0.9(Bi_{0.5}Na_{0.5})TiO_3$ – $0.05BaTiO_3$ – $0.05(Bi_{0.5}K_{0.5})TiO_3$ (Wang *et al.* 2004; Wang *et al.* 2005b)	700	2	k_t = 0.492	0.34	148	35.9	~3.7
$Bi_{0.5}(Na_{0.7}K_{0.25}Li_{0.05})_{0.5}TiO_3$ (Lin *et al.* 2004a; Lin *et al.* 2004b; Lin *et al.* 2006)	1276	4.1	-	0.221	145	-	-
$Bi_{0.5}(Na_{0.84}K_{0.16})_{0.5}TiO_3$ + $0.02SrTiO_3$ + 0.3wt% Nb_2O_5 (Yoo *et al.* 2004)	868	-	k_t = 0.453	0.34	185	-	-
$0.91(Bi_{0.5}Na_{0.5})TiO_3$ – $0.09Ba(Ti_{0.942}Zr_{0.058})TiO_3$ (Peng *et al.* 2005)	881	7	-	-	147	~15	~2.5
$[Bi_{0.5}(Na_{0.94}Ag_{0.06})_{0.5}]_{0.94}Ba_{0.06}TiO_3$ (Wu *et al.* 2005)	920	2.96	k_t = 0.516	0.31	168	-	-
0.96 $Bi_{0.5}(Na_{0.84}K_{0.16})_{0.5}TiO_3$ - 0.04 $SrTiO_3$ + 0.2wt% La_2O_3 (Yoo *et al.* 2006)	768	~4.8	-	0.40	215	~15	~4

Most of the piezoelectric properties were improved in ternary system compared with the binary system. Many studies were carried out on BNT-BKT-BT system which is focusing on the locating MPB position or looking for a composition having better properties (Nagata ***et al.*** 2003; Wang ***et al.*** 2004; Li ***et al.*** 2005; Makiuchi ***et al.*** 2005; Wang ***et al.*** 2005b). Figure 2.13 shows the phase relationship of BNT-BKT-BT system. Most of the reported systems are close to the MPB for better performance, but there is a drawback that the useable temperature range will be reduced. In BNT system, referring to the phase diagram of Takenaka et al. early work in Figure 2.12. the pure BNT will change from ferroelectric rhombohedral phase (F_α) to antiferroelectric phase when temperature was increased to ~230 ^oC. The ferroelectric properties will disappear at that temperature and thus do not have any piezoelectric properties. This transition temperature is referring to the depolarization temperature (T_d). The T_d in the BNBT-100x system rapidly decreases as the amount of $BaTiO_3$ increases and becomes a minimum at the MPB region which is ~130 ^oC. Depolarization temperature will dominate the useable temperature range in different device applications. It is important to consider the both piezoelectric properties and depolarization temperature improvement at the same time. In the previous work, only a few researchers reported this important factor (Wang ***et al.*** 2004; Wang ***et al.*** 2005b).

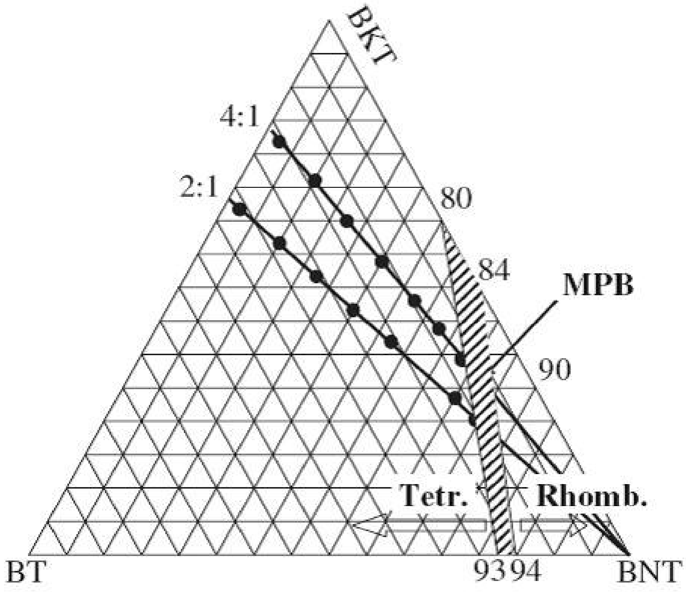

Figure 2.13 Phase relationship among $(Bi_{0.5}Na_{0.5})TiO_3$ (BNT), $(Bi_{0.5}K_{0.5})TiO_3$ (BKT) and $BaTiO_3$ (BT) in the (1-x-y)$(Bi_{0.5}Na_{0.5})TiO_3$ – (x)$(Bi_{0.5}K_{0.5})TiO_3$ –(y) $BaTiO_3$ system. (Rhomb: Ferroelectric rhombohedral phase, Tetr: ferroelectric tetragonal phase, MPB: morphotropic phase boundary (Makiuchi *et al.* 2005).

CHAPTER 3 MATERIALS FABRICATION AND CHARACTERIZATIONS

3.1. INTRODUCTION

In the previous Chapter, review of different types of lead-free piezoelectric ceramics were given, showing that each type of ceramics has its own characteristics and advantages. Among those lead-free ceramic systems, the bismuth sodium titanate based perovkite system has drawn great attention from researchers due to its good piezoelectric properties. In addition, the relatively simple technique and procedure in the fabrication, especially sintering in air, attracts industrial manufacturer to use this in commercial products. The properties of the BNT-based lead-free ceramics were improved by using doping or additives. Ternary BNT-based systems were developed based on some promising binary systems, for example $(Bi_{0.5}Na_{0.5})TiO_3$ – $BaTiO_3$ (Takanaka *et al.* 1991) and $(Bi_{0.5}Na_{0.5})TiO_3$ – $(Bi_{0.5}K_{0.5})TiO_3$ (Buhrer 1962). $(Bi_{0.5}Na_{0.5})TiO_3$ – $(Bi_{0.5}K_{0.5})TiO_3$ – $BaTiO_3$ (BNT-BKT-BT) system is one of the most promising systems. The BNT-BKT-BT system still has areas for improvement, including enhancement in the piezoelectric coefficients, electromechanical coupling coefficients, mechanical quality factors, ferroelectric remnant polarization, also in reduction of dielectric loss and conceive field. Another important factor to be improved is to increase the depolarization temperature which can broaden the useable temperature range for device applications. Based on our previous work, $0.90(Bi_{0.5}Na_{0.5})TiO_3$ – $0.05(Bi_{0.5}K_{0.5})TiO_3$ – $0.05BaTiO_3$ (BNKBT-5) system has good all round properties (Wang *et al.* 2005b). BNKBT-5 was chosen as a basic chemical formula in our study. Three different materials were chosen as the additives/dopings in our system, including cerium oxide (CeO_2), dicalcium ferrite ($Ca_2Fe_2O_5$) and bismuth lithium titanate $(Bi_{0.5}Li_{0.5})TiO_3$.

Cerium oxide is a common additive in $BaTiO_3$ (Jaffe *et al.* 1971) and PZT (Xu 1991; Yoo *et al.* 1998; Srimaungsong *et al.* 2005). Wang et al. (Wang *et al.* 2003b) reported the effect of CeO_2 in BNBT-6 system. The result shows that addition of CeO_2 can improve the piezoelectric properties and also reduce the dielectric loss.

Dicalcium ferrite is a doping used in PZT (Belding and M.G. 1970; Xu 1991) which is a “hard” dopant. Most “hard” dopants can enhance the mechanical quality factor of the ceramics and reduce the dielectric loss.

In BNT system, when the Li^+ ions replace part of the Na^+ composition, the chemical formula of the solid solution can be expressed as $(1-x)(Bi_{0.5}Na_{0.5})TiO_3$ – $(x)(Bi_{0.5}Li_{0.5})TiO_3$. A ternary BNT system was reported by Lin et al. (Lin *et al.* 2004a; Lin *et al.* 2004b; Lin *et al.* 2006) which have the chemical formula of $Bi_{0.5}(Na_{1-x-y}K_xLi_y)_{0.5}TiO_3$ exhibiting good piezoelectric properties. Therefore bismuth lithium titanate (BLT) was chosen as a dopant in our study.

In this Chapter, BNKBT-5 and the modified BNKBT-5 ceramics were prepared by a conventional mixed-oxide method. The ferroelectric, dielectric and piezoelectric properties of the ceramics were measured and reported.

3.2. FABRICATION OF CERAMICS

In general, four steps are included in the fabrication of BNKBT ceramics, including powder preparation, dry pressing, binder burnout and sintering. All equipments are cleaned by pure ethanol and acetone before the experiment which aimed to avoid contamination by impurities that could affect the properties of the samples. In this study, 3 different systems of ceramic powder based on BNKBT-5 have been fabricated; the chemical formulas are listed below:

(a) $0.90(Bi_{0.5}Na_{0.5})TiO_3 – 0.05(Bi_{0.5}K_{0.5})TiO_3 – 0.05BaTiO_3$ (BNKBT-5)

(b) BNKBT5 + x mol% CeO_2, with x ranged from 0 to 1 mol%.

(c) (1-x) BNKBT5 – (x) $Ca_2Fe_2O_5$, with x ranged from 0 to 1 mol%.

(d) $(0.90-x)\ (Bi_{0.5}Na_{0.5})TiO_3 – 0.05(Bi_{0.5}K_{0.5})TiO_3 – (x)(Bi_{0.5}Li_{0.5})TiO_3 – 0.05BaTiO_3$ with x ranged from 0 to 2.5 mol%. (BNKLBT-100x)

3.2.1. PREPARATION OF THE BNKBT-BASED POWDER

The raw materials used in the powder preparation are reagent grade metal oxides or carbonate powders, including Bi_2O_3 (99.9%, ACROS Organics), Na_2CO_3 (99.95%, International Laboratory USA), K_2CO_3 (99%, Pcanreac Quinica SA), Li_2CO_3 (99+%, International Laboratory USA), TiO_2 (99.9%, Sigma-Aldrich), CeO_2 (99.9%), $CaCO_3$ (99+%, Sigma-Aldrich) and Fe_2O_3 (99%, Sigma-Aldrich). Dicalcium ferrite is prepared by ball-milling $CaCO_3$ and Fe_3O_4 then mixed well in correct molar ratio and calcinated at 900 ^{o}C. All the alkali metal carbonates have been heated up to 300 ^{o}C then kept in an oven with temperature higher than 100 ^{o}C since all the alkali metal carbonates are highly water absorbing.

3.2.1.1. Preparations, calcination, sintering and surface finishing of ceramic samples

The powders were weighed and mixed well in alcohol using zirconia balls for 10h. The calcination was conducted at 800 ^{o}C for 2 h. The calcinated powder was ball-milled again in alcohol using zirconia balls for 10h.

Before the dry pressing procedure, the dried calcinated powder was mixed with polyvinyl alcohol (PVA) as binder for granulation. The concentration of the PVA solution is about 5wt% in water and the mixing ratio with the powder and PVA is 1: 0.18. The PVA and the powder were mixed continuously to obtain a homogeneous mixture. A required amount of powder was put into a stainless steel pressing mould and evenly distributed inside the mould. A uni-axial pressure of ~30 MPa was applied for several minutes. Under such pressure, excess air inside the mould was driven out and the ceramic powder became a well-packed disc. After compacting into disc, it was taken out for the next processing step. The dimensions of the green discs are 11.5 mm in diameter and ~1.2 mm in thickness.

Heat treatment is an essential and important procedure in fabricating ceramic samples and it is usually carried out in a computer controlled furnace. The PVA contained in the pressed discs should be removed before sintering. The organic binder inside the sample can be burnt out at around 600 ^{o}C. During the binder burnout, the samples were placed on an alumina plate which had a layer of sintered BNKBT ceramic powder on top without covering. Carbon dioxide was produced instead of carbon monoxide when an oxygen-rich atmosphere was used. The organic burnout process was carried out with a low heating rate of 2 ^{o}C/min and the temperature was kept for 2h to ensure the complete elimination of the binder. After the heat-treatment, the specimens were cooled down naturally.

After the organic burnout process, the samples were covered by an alumina crucible and placed into a high temperature furnace (Carbolite RHF1400) for sintering. The temperature of the furnace was firstly increased to 800 ^{o}C with the heating rate of 5 ^{o}C/min. The temperature was kept for 2h for calcinations and pre-sintering. During calcination, a solid-state reaction will happen to form a partially crystallized specimen.

During the pre-sintering process, the internal stresses of the sample can be released thus preventing the sample from cracking. Sintering is used to densify the ceramic and change the size of the pores between the particles. During sintering, the pores become smaller and more spherical in shape (Callister 1997) and the properties of the sample can be enhanced. The sintering process was carried out at 1170 ^{o}C for 2h with a heating rate of 3 ^{o}C/min. The samples were cooled down to room temperature with a cooling rate of 5 ^{o}C/min. The sintered ceramic discs had the dimension of ~10mm in diameter and ~1mm in thickness.

Polishing is an essential step for ceramics fabrication since ceramics have shrinkage after the sintering process, and polishing can refine the surface roughness and ensures the two flat surfaces are parallel to each other. The ceramics were polished with fine wet silicon carbide abrasive papers until the thickness becomes uniform. If the thickness is not uniform, it will easily break down during poling as the thinner part experiences a higher electric field. In addition, non-uniform thickness will affect the performance of the ceramics in the thickness mode. After polishing, a thin layer of silver paste was applied on both surfaces of the discs and fired at 650 ^{o}C for 15mins as electrodes for subsequent measurements.

3.2.1.2. Poling Procedures

A sintered BNKBT/BNKBT-based ceramic disc does not have any piezoelectric property without poling. The domains are all randomly oriented and the material is isotropic thus no piezoelectric effect occurs. During poling, the dipoles inside the ceramics are aligned when a d.c. electric field is applied. After poling, the electric field is removed and a remnant polarization appear to make the sample piezoelectric (Xu 1991). The poling conditions are different for different materials. The poling field of the material can be estimated from its hysteresis loop. Poling time and poling temperature can be optimized by a poling test. The poling circuit is shown in Figure 3.1.

The sample was mounted on a holder and placed in a silicone oil bath during the poling process. The oil bath was heated up to the poling temperature and was kept constant during the process. The applied voltage, V_{app} can be calculated by the following equation:

$$V_{app} = (\text{Poling Field}) \times (\text{Thickness of the disc}) \qquad (3.1)$$

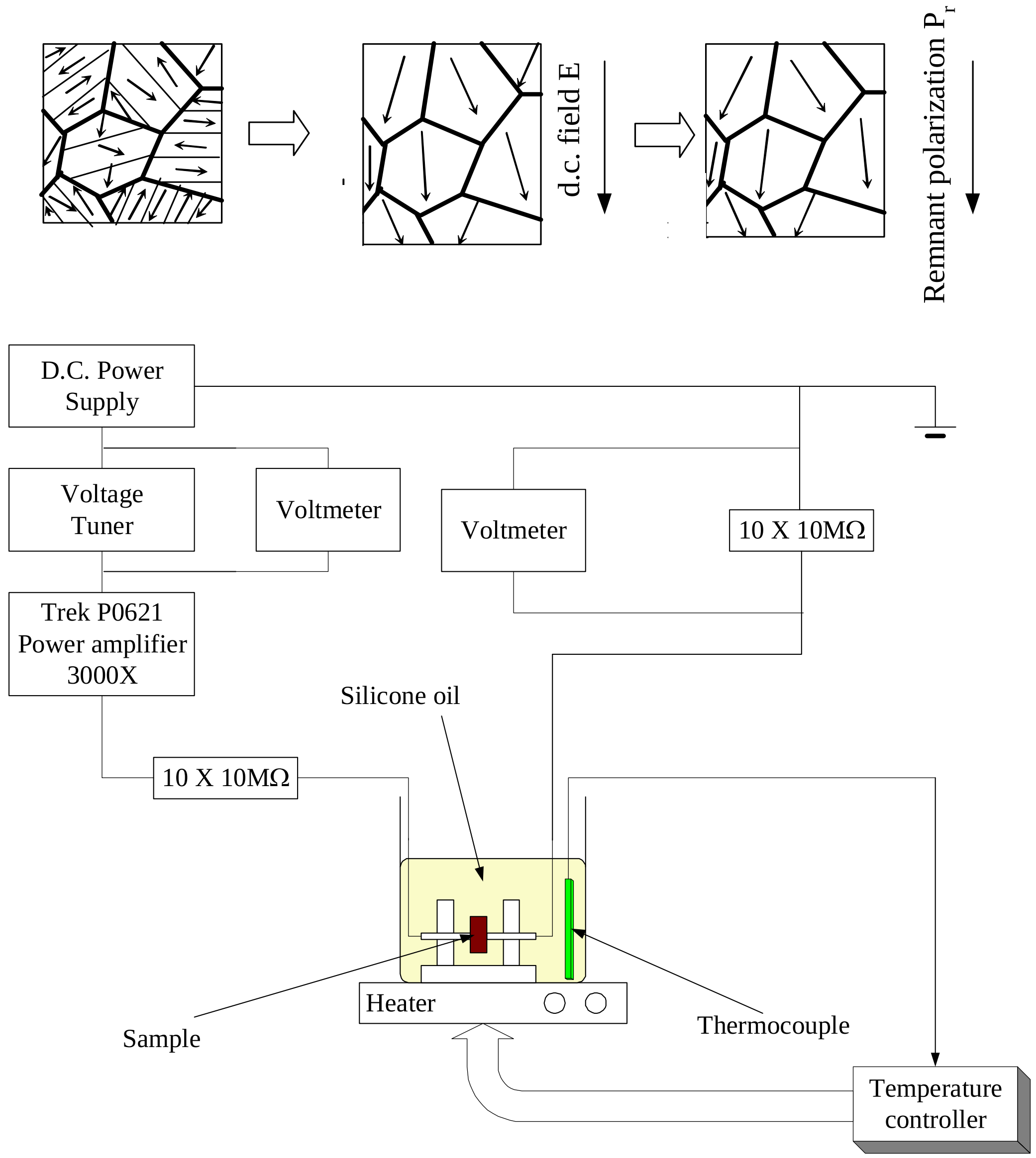

Figure 3.1 Schematic diagram of the d.c. poling circuit for bulk ceramic sample.

The voltage was increased slowly until the applied voltage V_{app} was reached and the voltage was kept for a designated time. After the poling time, the silicone oil bath was cooled down. During cooling, the voltage was kept constant.

After poling, a lot of surface charges were generated on the surfaces of the sample and short-circuit was required. The poled sample was wrapped in an aluminium foil and placed at room temperature for 24 hours.

3.2.2. CHARACTERIZATION OF BNKBT/BNKBT-BASED CERAMICS

3.2.2.1. Density measurement

The density of a ceramic is an indicator of its quality which is very much dependent on the amount of defects, such as impurities and pores, in the sample. It is also affected by the fabrication parameter, for example, the sintering temperature. If the ceramic density is low compared with its theoretical value then its performance will be degraded. According to the Archimedes principle, dry mass of the sample in air (m_{dry}) and the mass of the same sample suspended in water (m_{water}) are measured using an electronic balance. With those two parameters, density of the sample can be calculated by the following equation:

$$\rho = \frac{m_{dry}}{m_{dry} - m_{water}} \cdot \rho_{water} \qquad (3.2)$$

where is the density of the sample and $_{water}$ is the density of water which is assumed to be 1000 kg/m^3.

3.2.2.2. X-ray diffraction and microstructural analysis

The crystal structure of the crystalline materials can be studied by X-ray diffraction (XRD). The X-ray beam incident on a material is partly scattered, partly absorbed and the rest is transmitted. The scattering of X-ray is related to the interaction between X-ray and crystal lattice of the materials. The X-ray scattered from different lattices interfere with each other and produces a diffraction pattern upon the change of incident angle of the X-ray beam. The X-ray reflectivity measurement configuration consists of the incident beam impinging on the sample material on a flat substrate and the X-ray reflected at the same angle as the incident radiation being detected. Peak detected intensity will appear when Bragg' Law is satisfied (Figure 3.2), which is:

$$2d_{hkl} \sin\theta_{hkl} = n\lambda \tag{3.3}$$

where d_{hkl} is the interplanar spacing of the { hkl } set of lattice planes with Miller indices h, k, l; θ_{hkl} the incident angle; n the integer order of the diffraction peak and λ is the wavelength of the radiation.

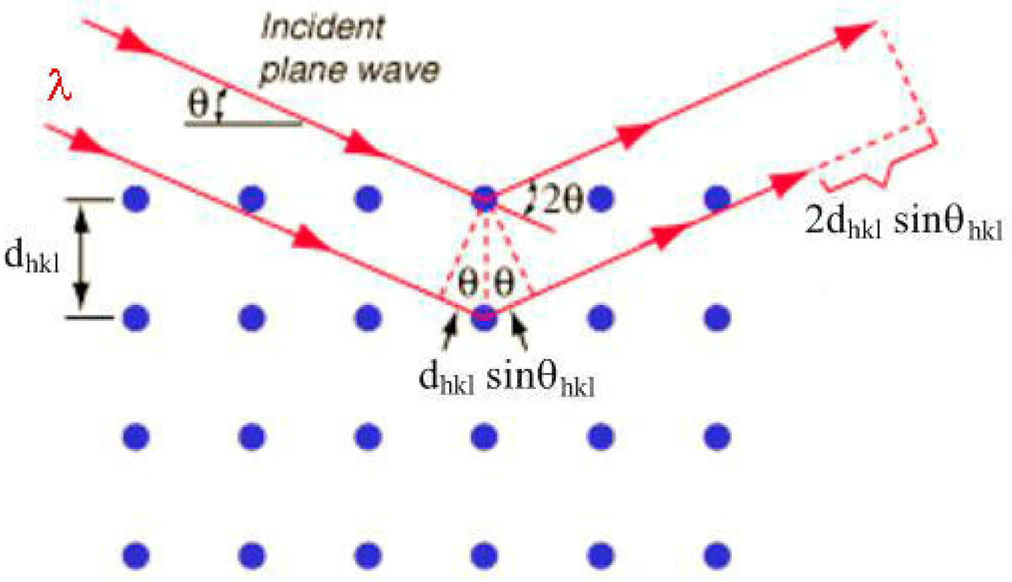

Figure 3.2 Schematic diagram of X-ray diffraction in crystal

Due to the system geometry, only those reflections from lattice places parallel to the surface are detected where the atoms in these planes are acting as a diffraction grating. X-ray diffraction may be used to determine the lattice parameters of a unit cell, identify unknown compounds and gives information on the structural development as a material is formed.

In this study, the crystalline structure of the lead-free ceramics was investigated by wide-angle X-ray diffraction. A Philips X'pert X-ray diffractometer system was used. It was operated in a four-circle mode and equipped with a pole figure attachment. The CuK_α radiation of $\lambda = 0.154$ nm was used.

The microstructure of the ceramic sample can be investigated by using scanning electron microscopy. The scanning electron micrographs (SEM) of the lead-free ceramics were obtained by a Leica Stereoscan 440 SEM. The top surface of the samples was observed after a thin layer of gold coating was deposited.

3.2.2.3. Ferroelectric hystersis loop measurement

For ferroelectric materials, the P-E hysteresis loop is one of the most important characteristics. The definition of a ferroelectric hysteresis loop has already been described in Chapter 2. The coercive field (E_c) and remnant polarization (P_r) can be obtained from the loop. This information can act as a reference for determining the required d.c. poling field. Usually, a poling field of two to three times that of the coercive field is applied during the d.c. poling process.

In this project, the ferroelectric hysteresis loops are measured using a Sawyer-Tower circuit (Sawyer and Tower 1930). A typical Sawyer-Tower bridge circuit contains two capacitors C_F and C_{Ref}, which are the ferroelectric capacitor (the sample) and a reference capacitor, respectively. In the P-E loop measurements, the value C_{Ref} should be larger than that of C_F (typically around 1000 times). The resultant hysteresis loop cannot be formed if this requirement is not satisfied.

The experimental setup of the hysteresis measurement is shown in Figure 3.3. The setup is controlled by a computer. During the measurement, the sample was placed in a silicone oil bath. An a.c. signal with designated amplitude was generated by a function generator (HP 8116A). The signal was amplified by a voltage amplifier (Trek 609D-6) before applied to the sample. The input and output signals from the Sawyer-Tower circuit were recorded by a digital oscilloscope (HP 5465A). The recorded data were stored in the computer for further analysis.

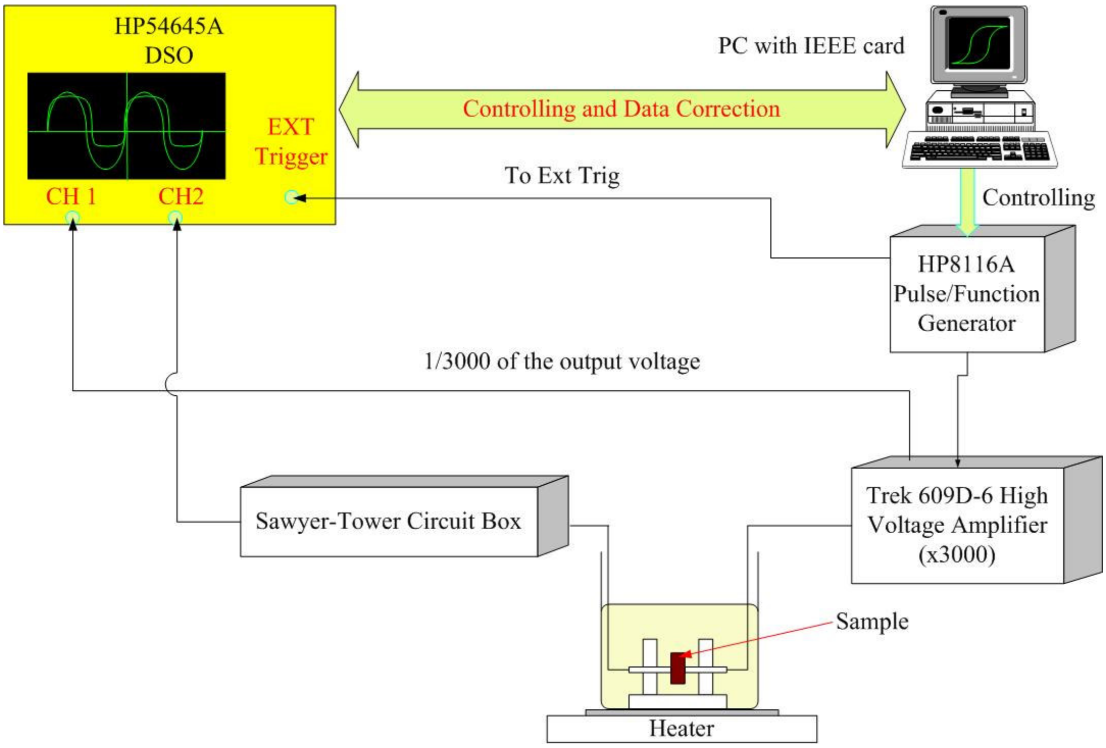

Figure 3.3 Schematic diagram of the hysteresis loop measurement.

The ferroelectric P-E loops were measured at different temperatures, including room temperature (~25 ^{o}C), 140 ^{o}C and 160 ^{o}C, respectively.

3.2.2.4. Dielectric properties

The dielectric properties of the ceramic samples, including the relative permittivity ε_r and dielectric loss tanδ, can be measured by a Schering bridge-based HP 4192A impedance analyzer. The measurement setup is shown in Figure 3.4.

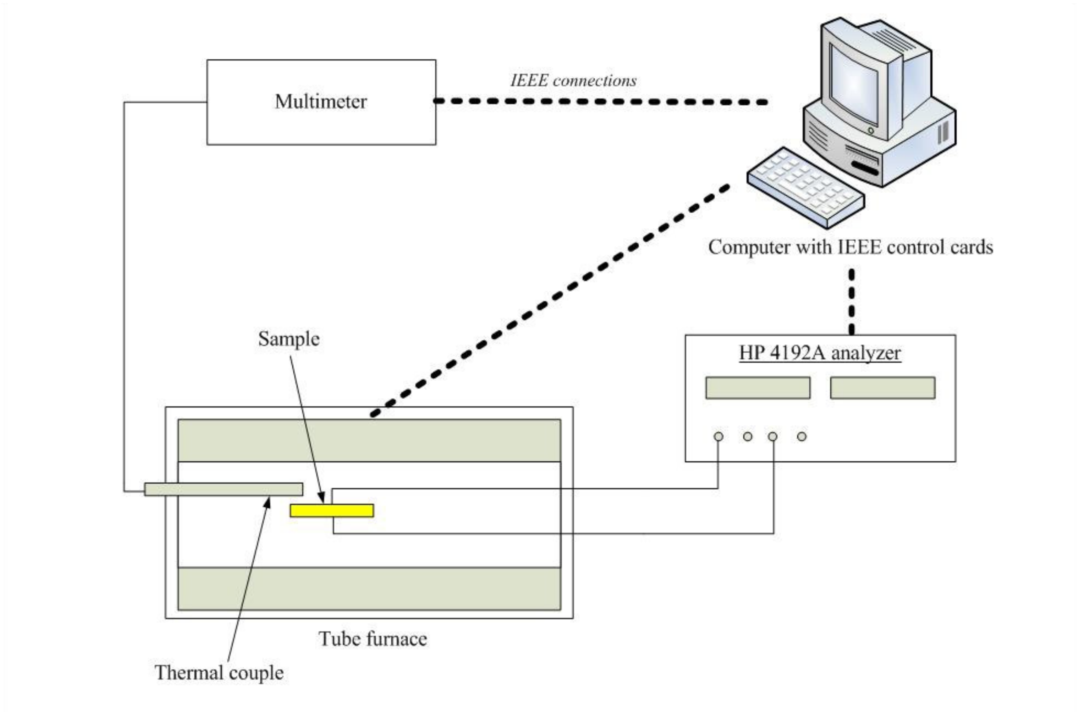

Figure 3.4 Dielectric measurement setup.

A computer equipped with IEEE control cards was used to control the equipment in the dielectric measurement. The ceramic sample was connected to the HP 4192A analyzer and placed inside a Carbolite furnace thus the capacitance of the sample can be measured up to over 400 ^{o}C. The temperature profile of the furnace was programmed in the computer and the data of capacitance and loss tangent were recorded in a computer file. The recorded capacitance was used to calculate the relative permittivity of the sample by the equation: $C = \frac{\varepsilon_0 \varepsilon_r A}{t}$, where C is the measured capacitance, ε_0 the permittivity of free space, A the electroded area and t is the thickness of the sample.

Dielectric materials absorb electrical energy under an alternating electric field and thus have dielectric loss. The relative permittivity can be expressed in a complex form:

$$\varepsilon_r = \varepsilon' - \varepsilon'' \qquad (3.4)$$

where ε’ is the real part of permittivity and the ε’’ is the imaginary part of permittivity. The dielectric loss is given by the following equation

$$\tan\delta = \frac{\varepsilon''}{\varepsilon'} \qquad (3.5)$$

Typically, an impedance analyzer can only measure the impedance down to about 40 Hz. The dielectric properties in the low frequency range is also important, especially in pyroelectric devices since the figure of merit of the devices is directly related to the relative permittivity in that range. Although the pyroelectric properties of the samples will not be presented there, the low frequency dielectric measurement can act as a reference for future uses of these materials. The low-frequency dielectric measurement is conducted in a Broadband dielectric spectrometer (Novocontrol GmbH Germany) which can measure dielectric properties at frequency down to mHz.

3.2.2.5. Piezoelectric properties

The piezoelectric constants related to the mechanical strain produced by an applied electric field are the “d” coefficient. The unit of the “d” coefficient can be expressed by meter per volt or coulomb per newton. The unit comes from the definition of the “d” coefficient.

$$d = \frac{\text{strain}}{\text{applied electric field}} \ (\text{m/V}) \tag{3.6}$$

$$= \frac{\text{short circuit charge density}}{\text{applied mechancial stress}} \ (\text{C/N}) \tag{3.7}$$

The piezoelectric d coefficient is closely related to mechanical displacement. Three axes are used to identify the direction in piezoelectric sample. The axes are defined similar to the Cartesian coordinate which 1, 2 and 3 representing the x, y and z directions. The 3-axis is used to indicate the direction parallel to the polarization direction of the sample. The first subscript of d_{ij} represents the direction of the polarization and the second subscript represents the direction of mechanical stress.

Among the “d” coefficients, only d_{33} coefficient was measured in the present work. The other d coefficients were calculated. A ZJ-3D d_{33} meter from Beijing Institute of Acoustics is used to measure the d_{33} values. The ceramic sample is placed in between the two measuring probes in the meter and the magnitude of d_{33} can be obtained from the meter directly. Figure 3.5 shows the schematic diagram of the d_{33} meter.

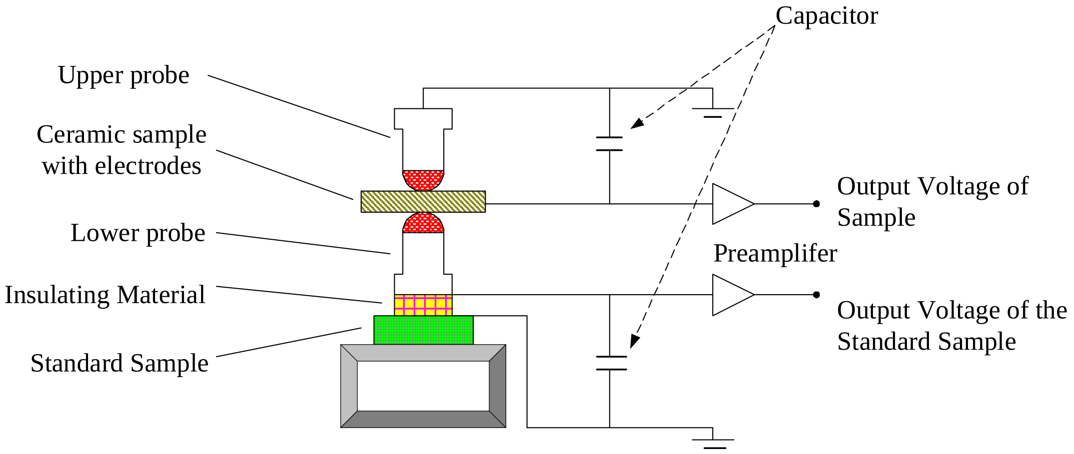

Figure 3.5 Schematic diagram of a d_{33} meter.

3.2.2.6. Impedance and phase spectra measurement

It is important to know the impedance of a piezoelectric material in order to match the impedance between the driving circuit and the transducer. Most properties of the piezoelectric samples can be evaluated by using the impedance and phase versus frequency spectra, which are measured by an impedance / gain phase analyzer (Hewlett Packard 4294A). When a poled piezoelectric sample disc is subjected to an a.c. signal, vibrational modes are excited. Two vibrational modes, the radial and thickness modes and their harmonics of a piezoelectric ceramic disc are observed from the impedance spectrum. The behaviours of the piezoelectric materials can be characterized in terms of an equivalent circuit with corresponding resonant and anti-resonant frequency. For a low loss ceramics, the series resonant frequency (f_s) and parallel frequency (f_p) are approximately equal to the frequency of minimum impedance (f_r), and the frequency of maximum impedance (f_a), respectively. For a circular disc, two main vibrational modes are excited, which are the radial mode (f_{rr}) and the thickness mode (f_{rt}) (Berlincourt *et al.* 1964).

Radial mode $$f_{rr} = \frac{1}{2r}\sqrt{\frac{1}{\rho s_{11}^{E}}} \tag{3.8}$$

Thickness mode $$f_{rt} = \frac{1}{2t}\sqrt{\frac{1}{\rho s_{33}^{E}}} \tag{3.9}$$

where 2r and t are the diameter and the thickness of the ceramic disc, the density of the ceramic, s^E_{11} and s^E_{33} are the elastic compliance of the ceramic material measured under a short circuit condition.

By using the information obtained from the impedance/phase frequency spectra, including the resonance frequency, anti-resonance frequency, impedance at resonance frequency etc at the corresponding resonance mode, the electromechanical coupling coefficient can be calculated by using the IEEE standard on Piezoelectricity (ANSI/IEEE 1987). The planar electromechanical coupling coefficient k_p was obtained from the k_p versus $(f_a-f_r)/f_r$ curve following the Standard, and the thickness electromechanical coupling coefficient k_t was calculated according to the equation:

$$k_t^{\ 2} = \frac{\pi}{2}\frac{f_r}{f_a}\tan\left(\frac{\pi}{2}\frac{f_a - f_r}{f_a}\right) \qquad (3.10)$$

Other than the electromechanical coupling coefficients, the mechanical quality factor Q_M can also be found from this method. Mechanical quality factor Q_M is the ratio of the reactance to the resistance in the series equivalent circuit. Therefore, it can be determined by the equivalent circuit analysis function built-in to the HP 4294 impedance/gain phase analyzer. Figure 3.6 shows the equivalent circuit for determining Q_M.

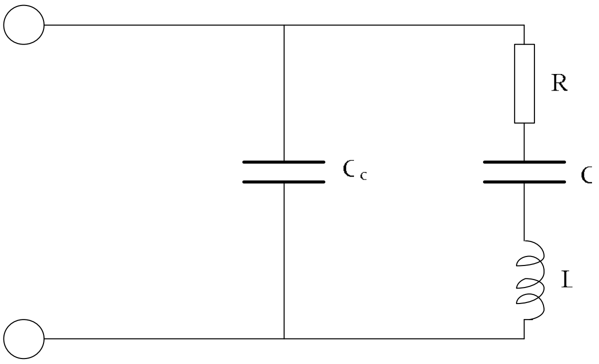

Figure 3.6 Equivalent circuit of a piezoelectric device.

C_o is the free electrical capacitance (at 1 kHz). C_1, L_1 and R_1 are the electrical capacitance, inductance and resistance respectively, which represent the converted compliance, effective mass and mechanical loss. Mechanical quality factor in specified resonance mode can also be calculated by the following equations:

$$Q_M = \frac{\omega L_1}{R_1} = \frac{1}{2\pi \cdot f_r \cdot R_1 \cdot (C_o + C_1)} \cdot \frac{f_a{}^2}{f_a{}^2 - f_r{}^2} \tag{3.11}$$

where ω is the angular frequency.

3.2.3. RESULTS AND DISCUSSION

3.2.3.1. BNKBT-5 + x mol% CeO$_2$, with x ranged from 0 to 1 mol% system

The density of BNKBT-5 with different amounts of CeO$_2$ as additive is shown in Figure 3.7. The density of the samples does not have much variation due to the addition of CeO$_2$.

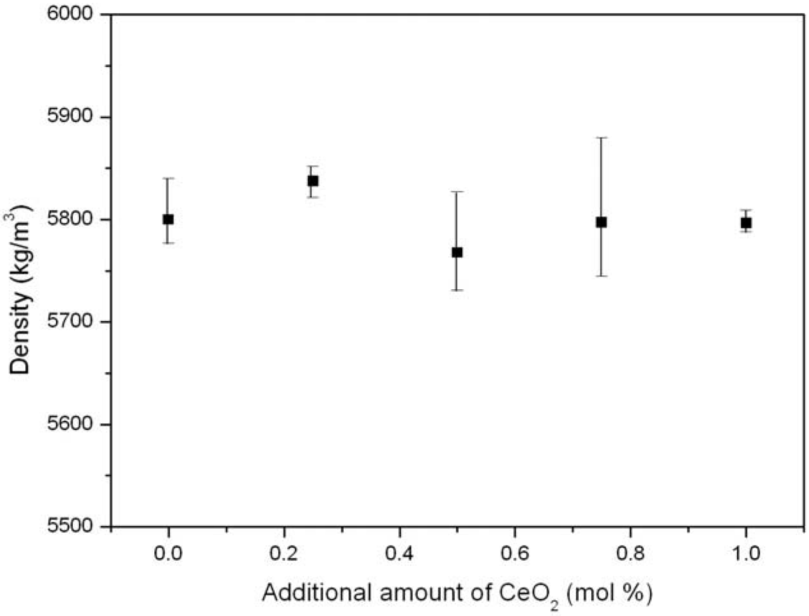

Figure 3.7 Density of BNKBT-5 with different amounts of CeO_2.

Figure 3.8 show the SEM micrographs of BNKBT-5 with various amounts of CeO_2 additive. From the SEM micrographs, dense samples can be obtained and it is noted that pure BNKBT-5 is more “rhomboid” shaped and after adding CeO_2, the grains become round in shape. This maybe due to the coexistence of both tetragonal and rhombohedral phases in similar amount. In addition, the average grain size is increasing after adding CeO_2.

)

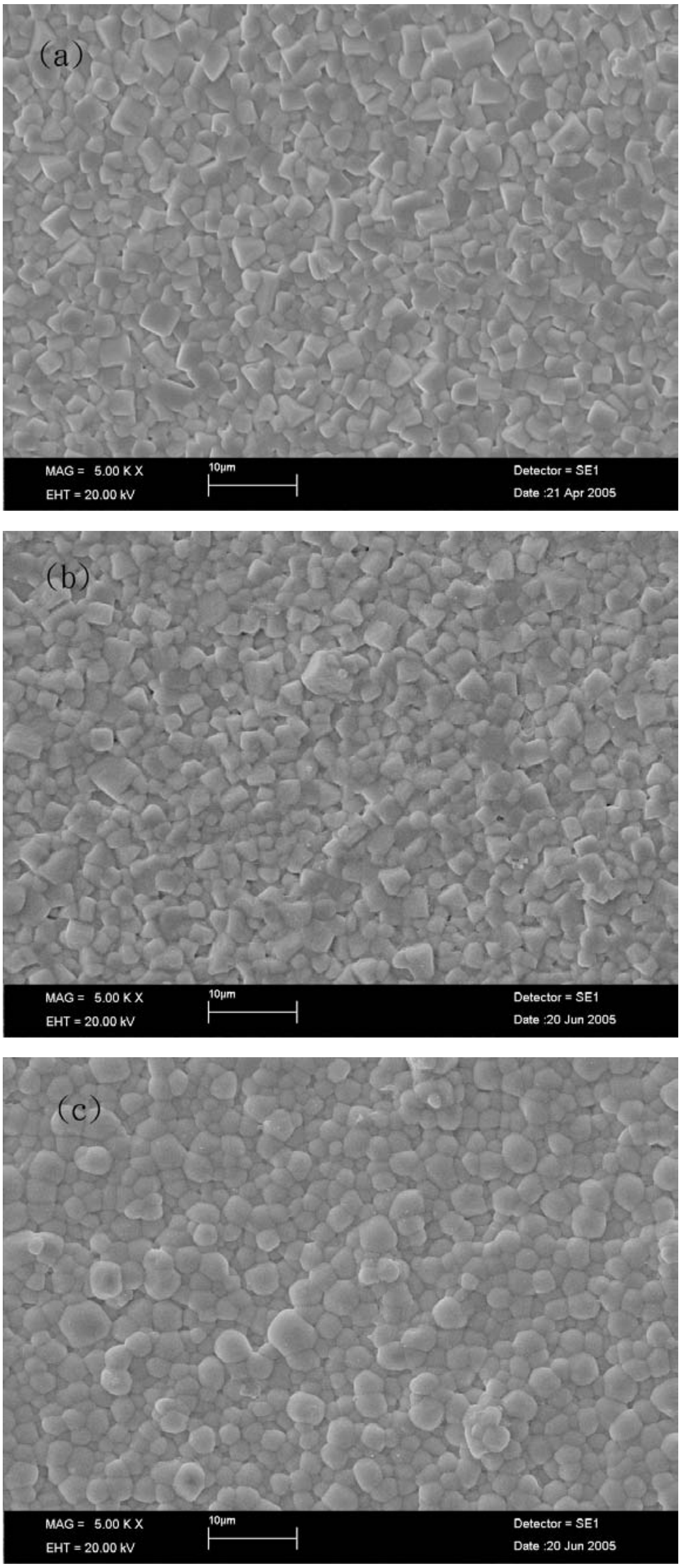
(a)
MAG = 5.00 K X
EHT = 20.00 kV
10μm
Detector = SE1
Date :21 Apr 2005
(b)
MAG = 5.00 K X
EHT = 20.00 kV
10μm
Detector = SE1
Date :20 Jun 2005
(c)
MAG = 5.00 K X
EHT = 20.00 kV
10μm
Detector = SE1
Date :20 Jun 2005

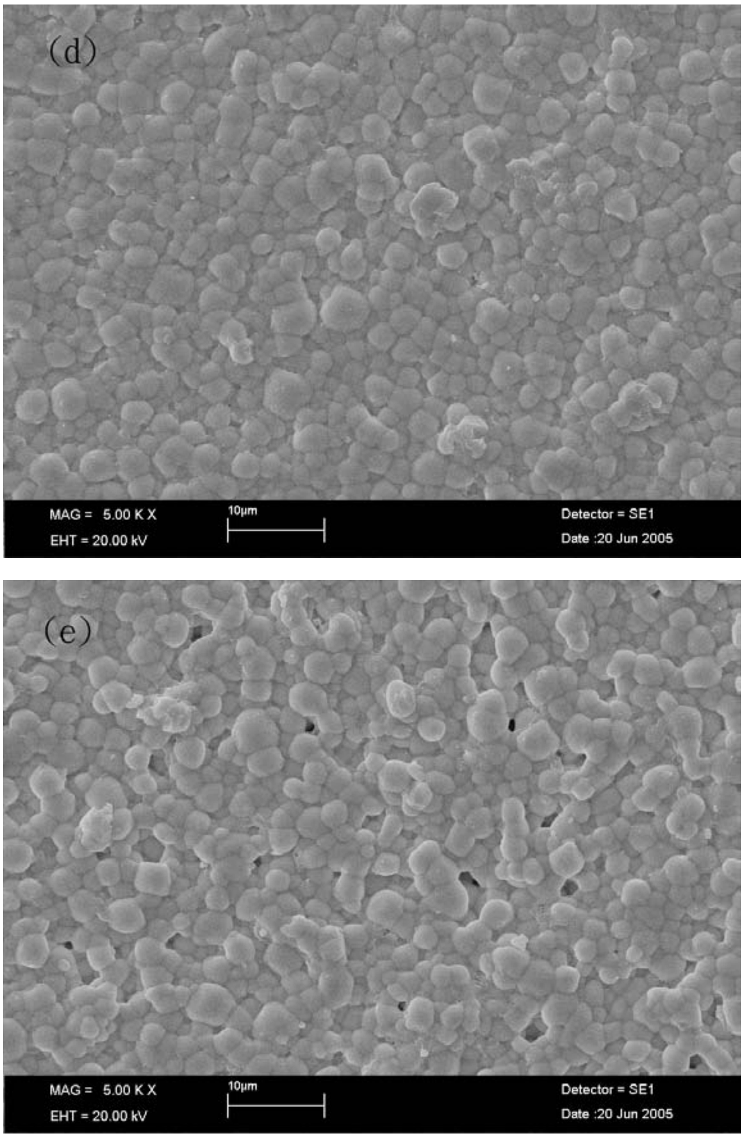

Figure 3.8 SEM micrographs of BNKBT-5 with various amounts of CeO_2 sintered at 1170^{o}C: (a) pure BNKBT-5; (b) 0.25 mol% CeO_2; (c) 0.5 mol% CeO_2; (d) 0.75 mol% CeO_2 and (e) 1 mol% CeO_2, respectively.

Good piezoelectric properties of BNT-based materials arise from the perovskite structure thus it is important to make sure that the sintered ceramic samples possess a single perovskite phase. Figure 3.9 shows the XRD pattern of BNKBT-5 and the compositions with addition of CeO_2. A single perovskite phase is found in the entire composition and no pyrochlore phase is observed in the system. As BNKBT-5 has the composition close to the phase boundary between BNT (rhombohedral), BKT (tetragonal) and BT (tetragonal), so both rhombohedral and tetragonal phases coexist in BNKBT-5, which broaden the (002) / (200) phase angle. The addition of CeO_2 slightly changes the phases which increases tetragonality in the BNKBT-5 and gives rise to larger separation between rhombohedral and tetragonal phases for increasing amount of CeO_2.

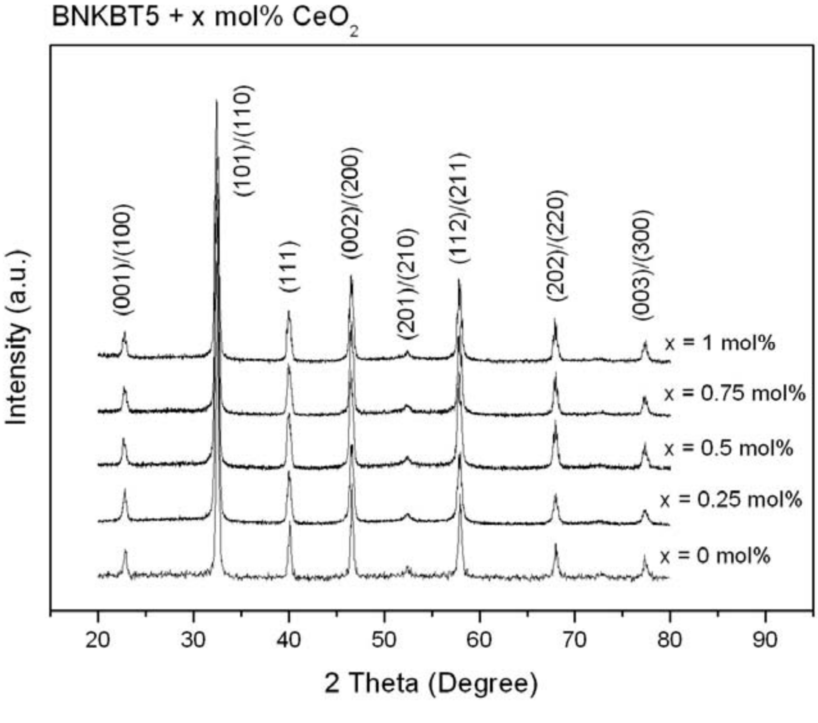

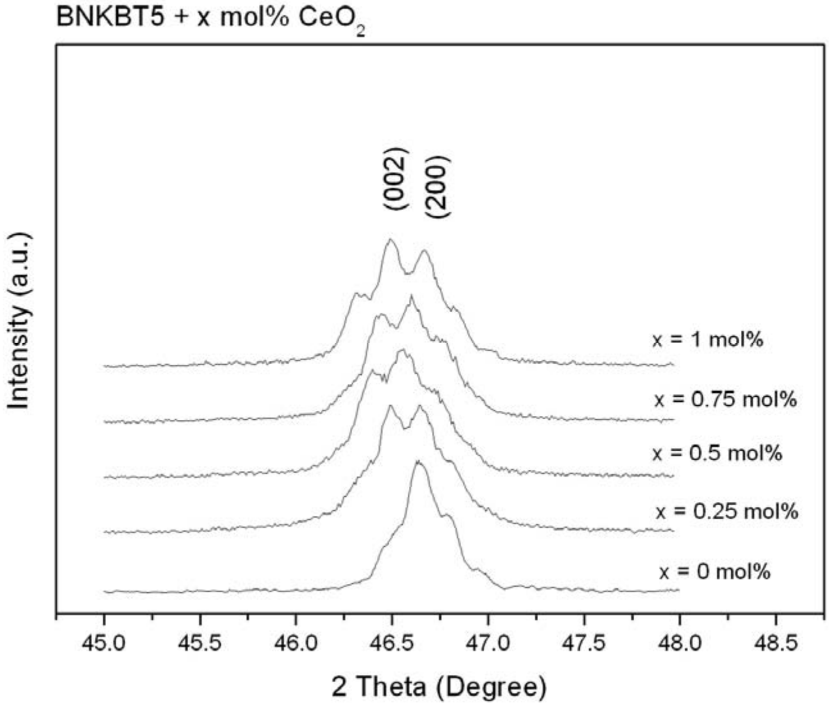

Figure 3.9 X-ray diffraction pattern of BNKBT-5 with different amounts of CeO_2 sintered at 1170 ^oC, (a) 20^o-80^o and (b) 45^o-48^o.

Figure 3.10 shows the ferroelectric hysteresis P-E loop of BNKBT-5 with different weight percentages of CeO_2 as additive at different temperatures. At room temperature, the remnant polarization P_r and the coercive field E_c of pure BNKBT-5 is 28.23 $\mu C/cm^2$ and 3.45 MV/m, respectively. The coercive field of the BNKBT-5 is reducing for increasing amount of CeO_2, which indicates that the ceramics can be poled at a lower poling field. The remnant polarization has been improved by adding CeO_2 and has reached the maximum value 31.1 $\mu C/cm^2$ for 0.25mol% CeO_2. The remnant polarization starts to reduce when more CeO_2 has been added. When the measuring temperature increases to 140 ^{o}C, the remnant polarization of all samples reduce to about 3 - 5 μC/cm^2. The pure BNKBT-5 exhibits P-E loop with “antiferroelectric-like” shape, other than the normal ferroelectric loop. This is mainly because BNT has a depolarization temperature T_d. As mentioned in previous Chapter, Takenaka et al (Takenaka *et al.* 1991) reported that BNT changed from a ferroelectric state to an antiferroelectric state at T_d. BNKBT-5 has similar properties as pure BNT but has a lower depolarization temperature than BNT. The antiferroelectric- like P-E loop indicates that the measuring temperature is close to the depolarization temperature. It is easily observed that the normal ferroelectric loops are changing to antiferroelectric-like P-E loops when the CeO_2 amount is increasing. The phenomena show that the addition of CeO_2 decreases the depolarization temperature of the BNKBT-5 system.

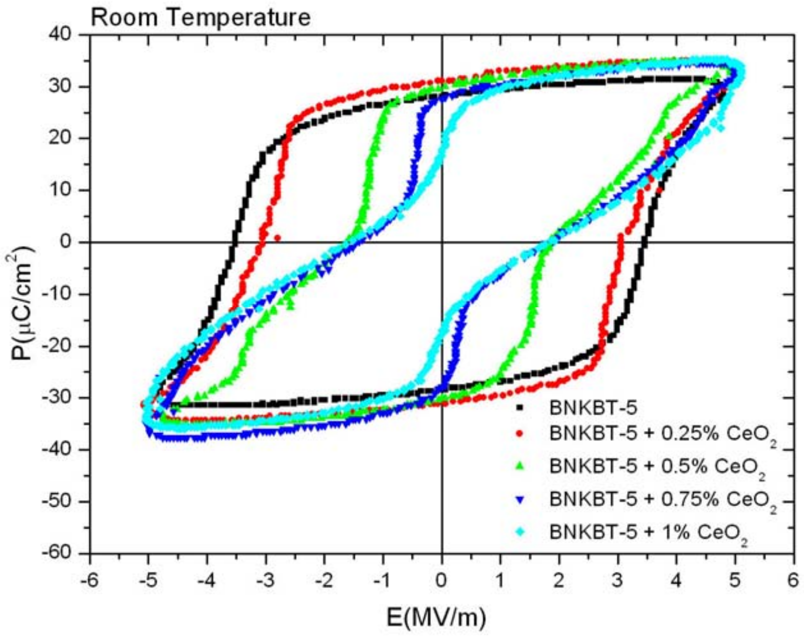
Room Temperature
P(μC/cm^2)
E(MV/m)
40
30
20
10
0
-10
-20
-30
-40
-50
-60
-6
-5
-4
-3
-2
-1
0
1
2
3
4
5
6
BNKBT-5
BNKBT-5 + 0.25% CeO$_2$
BNKBT-5 + 0.5% CeO$_2$
BNKBT-5 + 0.75% CeO$_2$
BNKBT-5 + 1% CeO$_2$

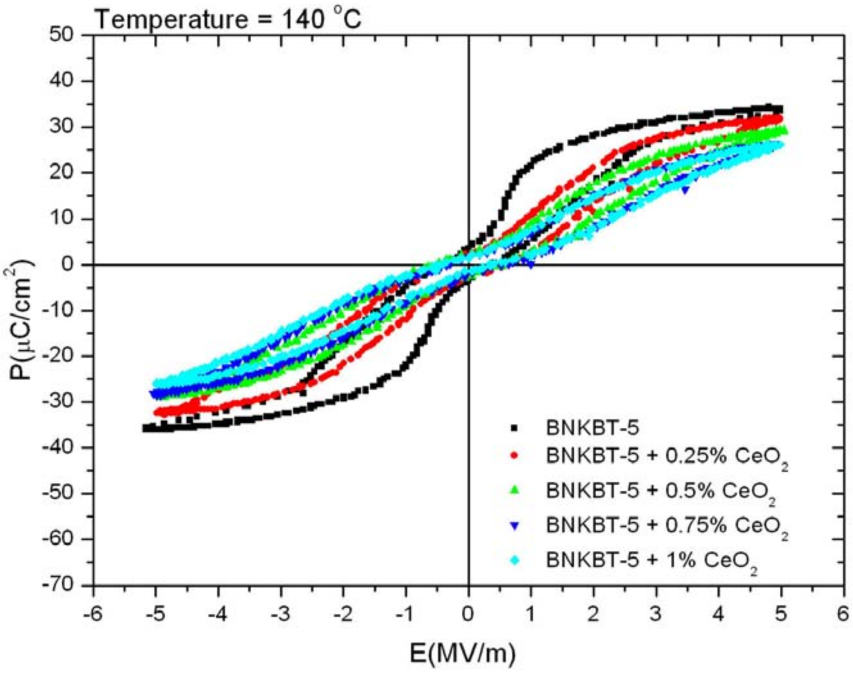
Temperature = 140 °C
P(μC/cm^2)
E(MV/m)
50
40
30
20
10
0
-10
-20
-30
-40
-50
-60
-70
-6
-5
-4
-3
-2
-1
0
1
2
3
4
5
6
BNKBT-5
BNKBT-5 + 0.25% CeO$_2$
BNKBT-5 + 0.5% CeO$_2$
BNKBT-5 + 0.75% CeO$_2$
BNKBT-5 + 1% CeO$_2$

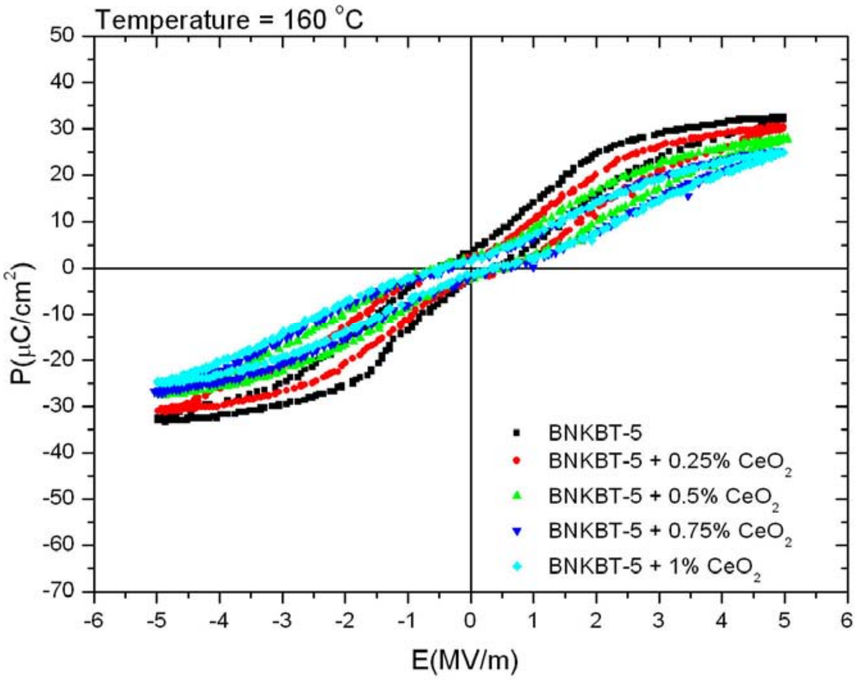

Figure 3.10 Ferroelectric hysteresis loops of BNKBT-5 with various amounts of CeO_2 measured at different temperatures, (a) room temperature, (b) 140 ^{o}C and (c) 160 ^{o}C, respectively.

Temperature dependence of relative permittivity ε_r and dielectric loss tanδ at 100 kHz with various amounts of CeO_2 as additive in BNKBT-5 is shown in Figure 3.11. All compositions have similar Curie temperature, which is ~300^{o}C. The amount of CeO_2 does not affect T_c but changes the depolarization temperature T_d. The T_d of pure BNKBT-5 is about 110 ^{o}C and slightly decreases to ~100 ^{o}C when 0.25 mol% CeO_2 has been added. A huge drop in T_d occurs when more than 0.25 mol% CeO_2 is added into BNKBT-5. T_d of BNKBT-5 with 1 mol% CeO_2 is ~50 ^{o}C which is very close to room temperature. The ferroelectric hysteresis loops show a good agreement with the temperature dependent dielectric properties. The result supports and explains the reason why antiferroelectric-like P-E loop occurs at room temperature for increased amount of CeO_2 additive.

The frequency dependence of ε_r and tanδ is shown in Figure 3.12 in the frequency range of 1 mHz to 100 kHz. All compositions have a similar performance beyond 1 kHz. The dielectric properties of this system at 1 kHz is shown in Figure 3.13. The relative permittivity increases steadily for increased amount of CeO_2. The dielectric loss reaches the lowest value (tanδ ~1.5%) after 0.5 mol% of CeO_2 has been added into BNKBT-5, which is about 40% reduction in the loss. The dielectric loss increases and remains steady below 0.5 mol% CeO_2 addition. This shows that CeO_2 can effectively reduce the dielectric loss in the BNKBT-5 system.

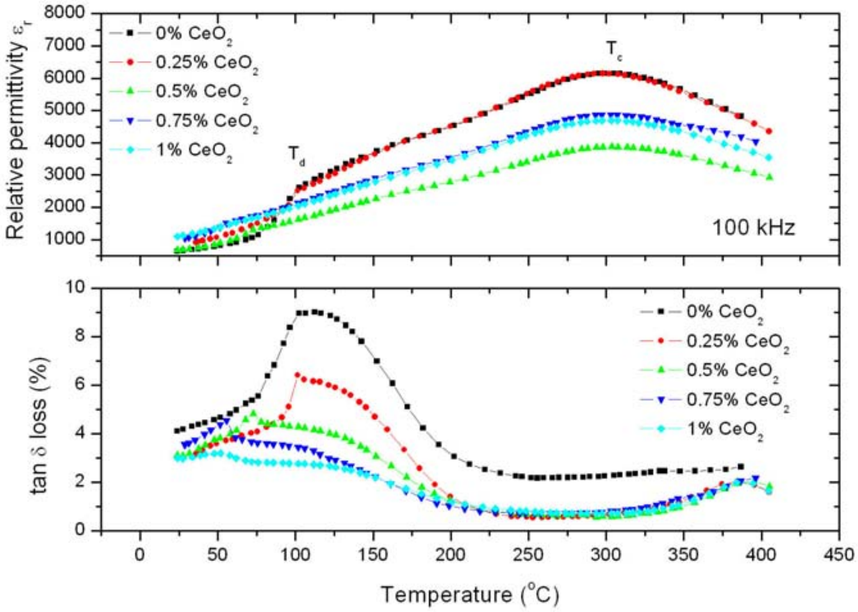

Figure 3.11 Temperature dependence of relative permittivity ε_r and dielectric loss tanδ at 100 kHz with various amount of CeO_2 as additive in BNKBT-5.

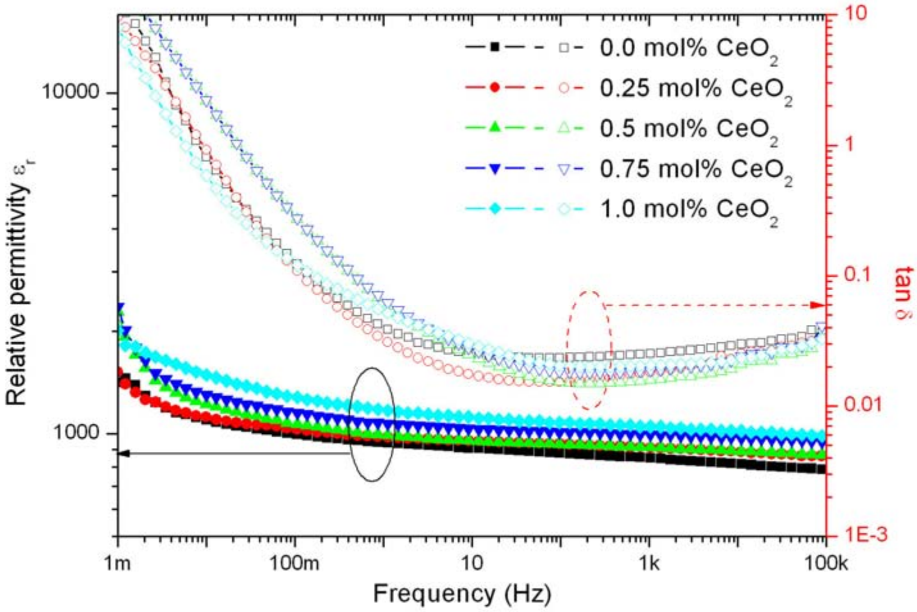

Figure 3.12 Frequency dependence of relative permittivity ε_r and dielectric loss tanδ measured under room temperature from 1 mHz to 100 kHz.

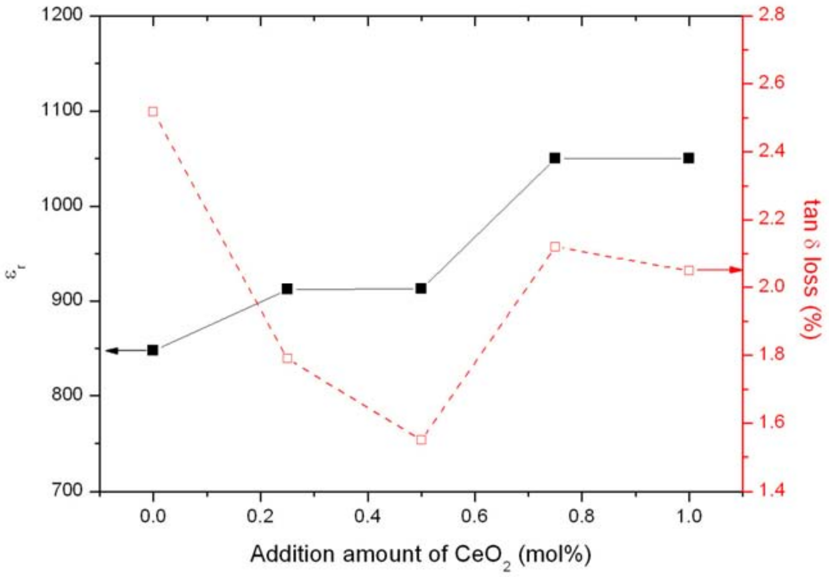

Figure 3.13 Relative permittivity ε_r and dielectric loss tanδ of BNKBT-5 with CeO_2 measured at 1 kHz.

The piezoelectric properties of the samples have been measured after d.c. poling. The poling field of the sample is depended on its coercive field measured in the P-E hysteresis loop. The poling field of pure BNKBT-5 is 4 MV/m under room temperature for 10 mins.

The piezoelectric properties of the CeO_2 added BNKBT-5 system are reported in Figure 3.14, including both the electromechanical coupling coefficient and mechanical quality factor in planar and thickness modes, and also the d_{33} piezoelectric constant. The electromechanical coefficients, k_p and k_t, both have the peak value at 0.25 mol% CeO_2 additive then drop rapidly for higher amounts. The same trend is seen in the mechanical quality factor in thickness mode also. The piezoelectric d_{33} constant also increases from 165 pC/N to 178 pC/N for addition of 0.25 mol% CeO_2 and reaches a maximum of 180 pC/N when 0.5 mol% CeO_2 has been added.

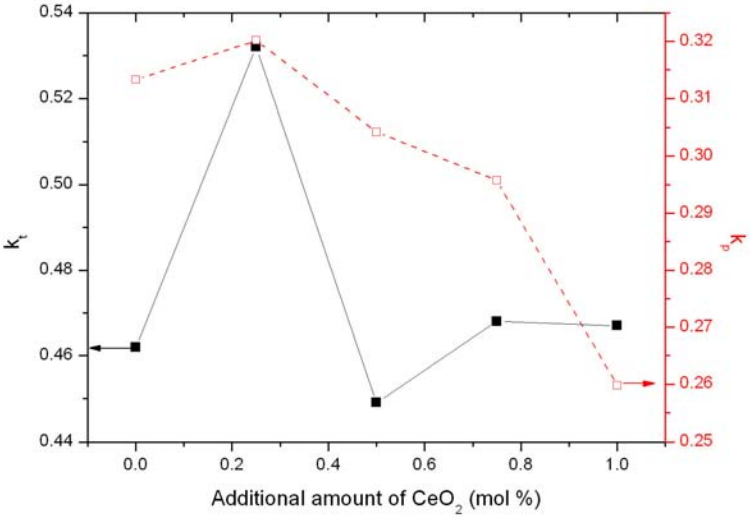

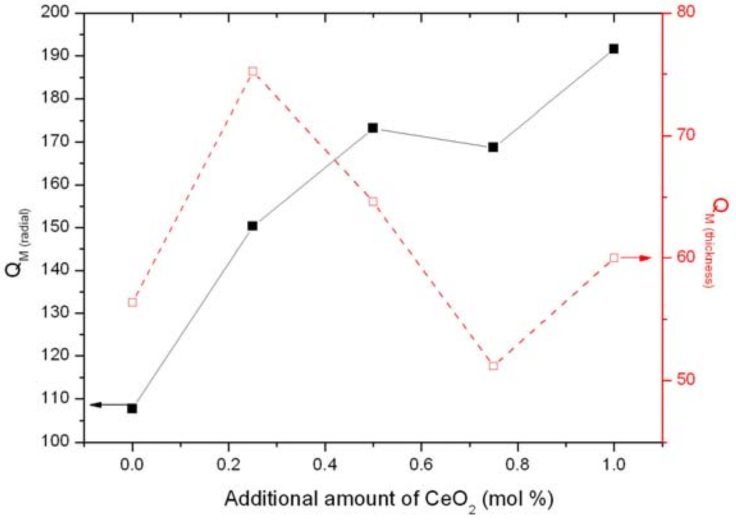

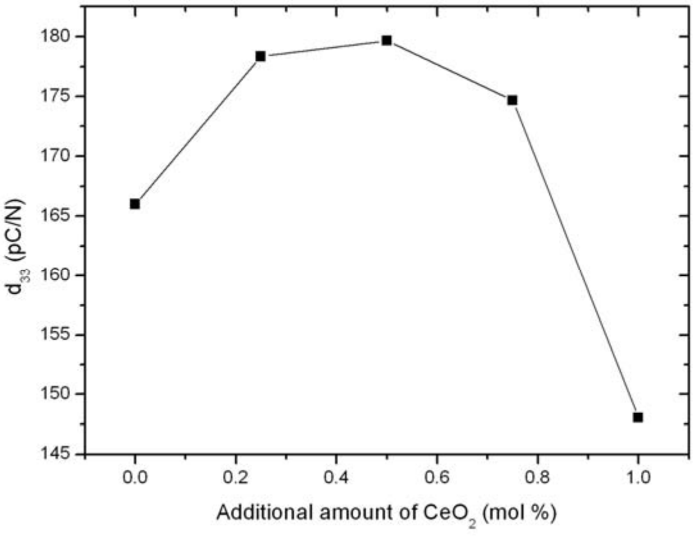

Figure 3.14 Piezoelectric properties of BNKBT-5 with CeO_2 added.

It is well known that CeO_2 is a commonly used additive for lead-base $Pb(Zr,Ti)O_3$ ceramics. It can cause a double effect on the $Pb(Zr,Ti)O_3$ ceramics, namely, decreasing the dissipation factor and improving the piezoelectric properties at the same time. The mechanism giving rise to the effect of CeO_2 is very complicated. Ce ion possibly exists in the BNKBT structure in two valence states: Ce^{4+} with a radius of 0.94 Å and Ce^{3+} with a radius of 1.18 Å. The result, hence, may be related to the simultaneous effect analogous to that in $Pb(Zr,Ti)O_3$ ceramics (Xu 1991). In view of the radius, it is obvious that Ce^{3+} cannot enter into the B site of BNKBT perovskite, but can occupy the A site. Here, there are two cases. One is that Ce^{3+} goes to the Bi^{3+} site in BNKBT. It is known that Bi_2O_3 is volatile at high temperature. During sintering, Bi^{3+} in BNKBT may leave the ceramics and form some vacancies in the lattice. It is possible for Ce^{3+} to fill in Bi^{3+}

vacancies. However, Bi^{3+} has a radius of 1.2 Å which is very close to 1.18 Å of Ce^{3+}. When Ce^{3+} enter into the Bi^{3+} site of BNKBT ceramics, the replacement of Bi^{3+} by Ce^{3+} almost does not cause deformation in the BNKBT lattice to make any evident contribution to enhance the domain movement. Another one is that Ce^{3+} occupies A site to replace Ba^{2+} in the BNKBT composition. In this case, Ce^{3+} functions as a donor leading to some vacancies of A site in the lattice, which facilitates the movements of domain walls so as to improve the piezoelectric properties significantly. In contrast with Ce^{3+}, Ce^{4+} has a smaller radius and may occupy the Ti^{4+} site. The occupation of Ce^{4+} in the Ti^{4+} site may change the space charges to suppress the domain movement, resulting in a decrease in the dissipation factor.

The most optimum composition in the system is BNKBT-5 with 0.25 mol% CeO_2. In this composition, it has the lowest dielectric loss and almost highest values in most of the piezoelectric properties. Furthermore, the T_d in this composition is over 100 ^oC which is in the acceptable temperature range for real application.

3.2.3.2. (1-x)BNKBT - (x) $Ca_2Fe_2O_5$ system with x ranged from 0 mol% to 1 mol%

The result of the density measurement in (1-x) BNKBT – (x) $Ca_2Fe_2O_5$ system is shown in Figure 3.15. The density of the samples is around 5700-5800 kg/m^3 and the density is decreasing with increasing amount of $Ca_2Fe_2O_5$.

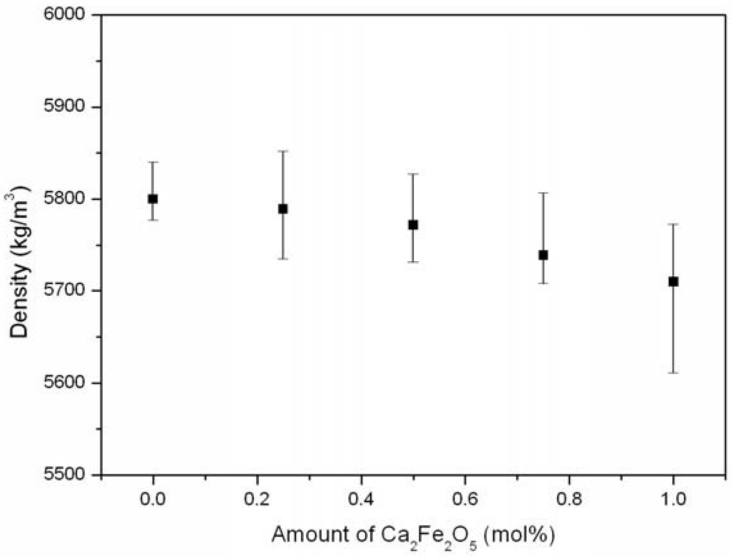

Figure 3.15 Density measurement of BNKBT-5 doped with $Ca_2Fe_2O_5$ system.

Although the density measurement shows that the density slightly decreases when doped with $Ca_2Fe_2O_5$, the ceramic sample are dense as seen in the SEM micrographs, as shown in Figure 3.16. It is easily observed that the grain size of the sample is increasing with the doping amount of $Ca_2Fe_2O_5$, which indicates that $Ca_2Fe_2O_5$ is acting as a sintering aid to reduce the sintering temperature in the BNKBT-5 system.

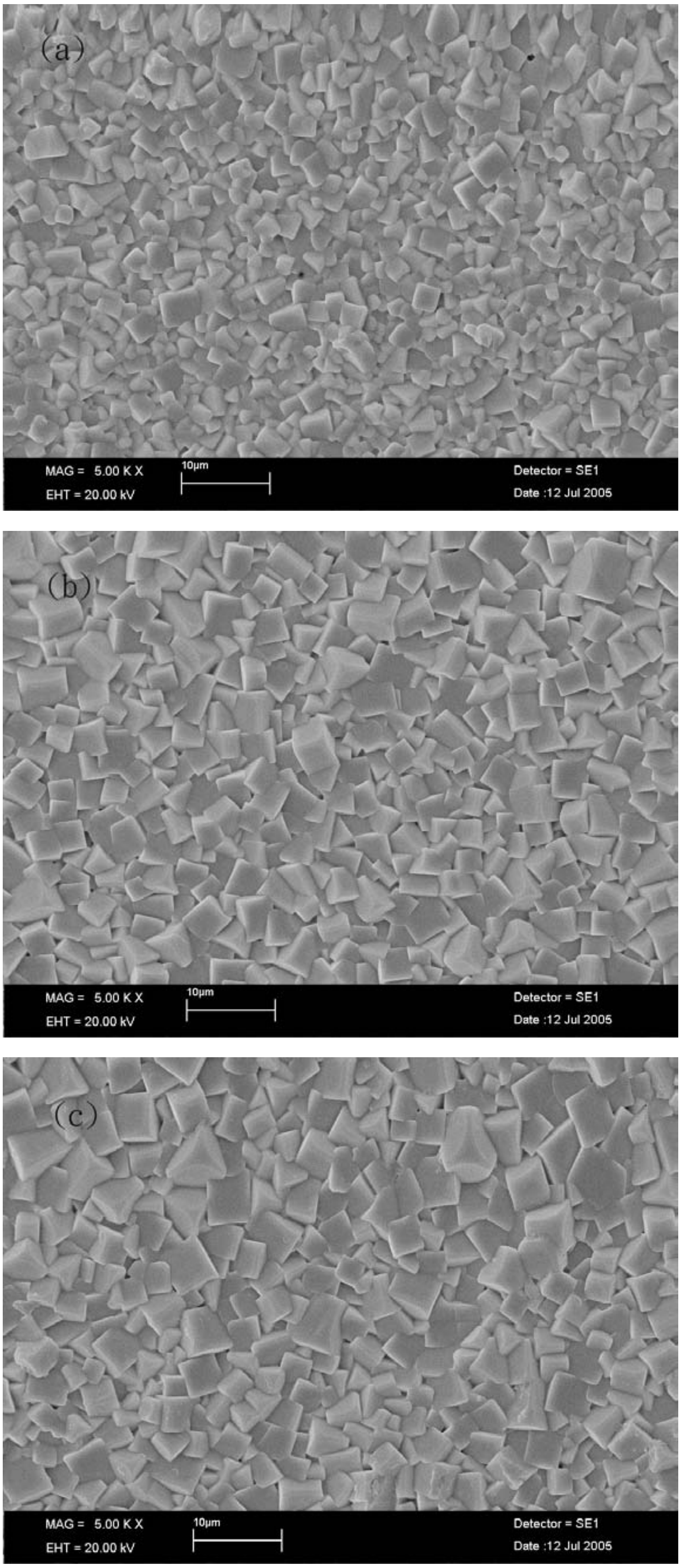
(a)
MAG = 5.00 K X
EHT = 20.00 kV
10μm
Detector = SE1
Date :12 Jul 2005
(b)
MAG = 5.00 K X
EHT = 20.00 kV
10μm
Detector = SE1
Date :12 Jul 2005
(c)
MAG = 5.00 K X
EHT = 20.00 kV
10μm
Detector = SE1
Date :12 Jul 2005

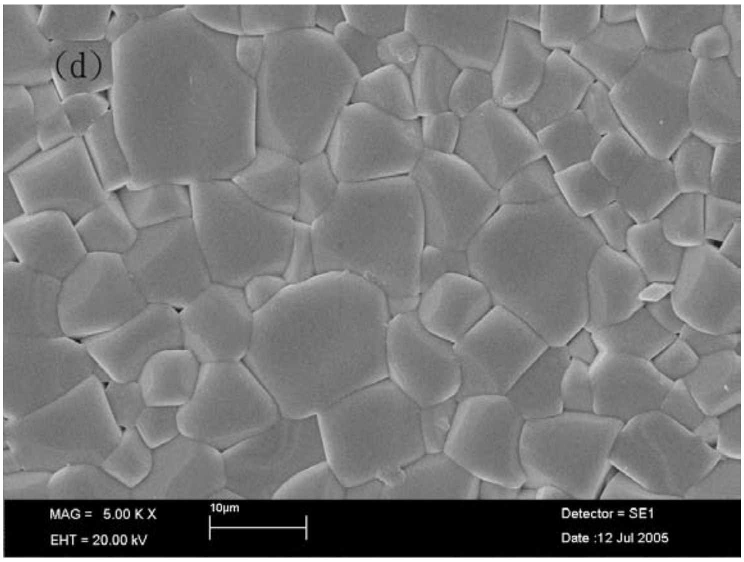

Figure 3.16 SEM micrographs of BNKBT-5 doped with different amounts of $Ca_2Fe_2O_5$, (a) 0.25 mol%, (b) 0.50 mol%, (c) 0.75 mol% and (d) 1.00 mol%, respectively.

The XRD patterns of different amounts of $Ca_2Fe_2O_5$ are shown in Figure 3.17. A single perovskite phase is found in the entire composition and no pyrochlore phase has been observed in the system. A small amount of $Ca_2Fe_2O_5$ increases the tetragonality and shift the (200) peak to a lower diffraction angle which indicates a lattice expansion along this axis.

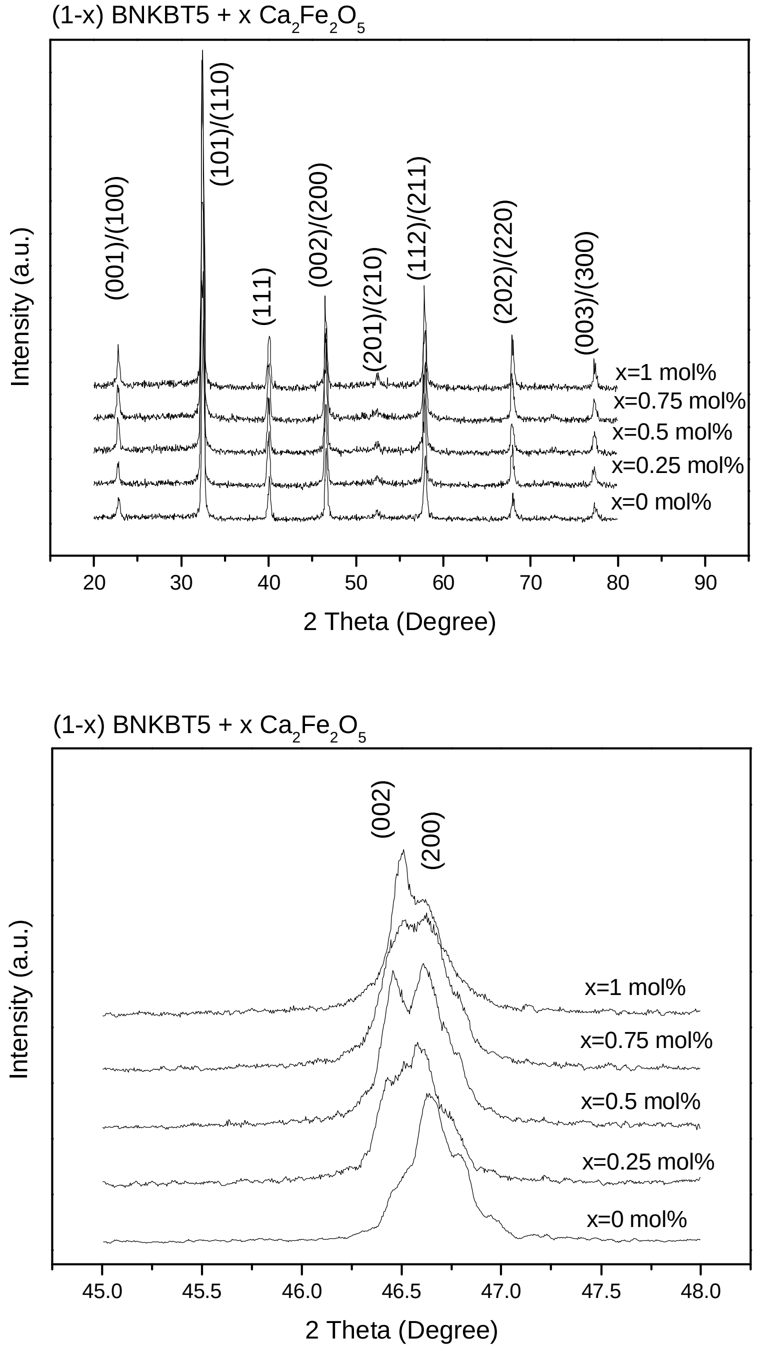

Figure 3.17 X-ray diffraction patterns of BNKBT-5 doped with different amounts of $Ca_2Fe_2O_5$ sintered at 1170°C, (a) 20°-80° and (b) 45°-48°.

The ferroelectric hysteresis P-E loops of the (1-x) BNKBT – (x) $Ca_2Fe_2O_5$ system is shown in Figure 3.18. All compositions have normal ferroelectric P-E loops at room temperature. The remnant polarization remains nearly the same for increasing amount of $Ca_2Fe_2O_5$. After the amount of $Ca_2Fe_2O_5$ is more than 0.5 mol%, the remnant polarization dropped slightly. After doping with $Ca_2Fe_2O_5$, the coercive field jumps to ~4 MV/m from ~3.5 MV/m for pure BNKBT-5 and retains higher E_c for all compositions. Based on the P-E loop measurements, the poling field of the samples in this system has been increased to over 4 MV/m to make sure the samples are fully poled. The ferroelectric P-E loops have also been conducted at 140 ^oC and 160 ^oC to investigate the ferroelectric properties in this temperature range. Results similar to that of BNKBT-5 with CeO_2 additive can be observed in this temperature range. Almost all the compositions doped with $Ca_2Fe_2O_5$ have the antiferroelectric-like P-E loops at 140 ^oC and the antiferroelectric-like loop is diminishing at higher doping level or at higher temperature. This is mainly due to $Ca_2Fe_2O_5$ lower the T_d of the sample, and this phenomenon can be clarify from the dielectric measurement.

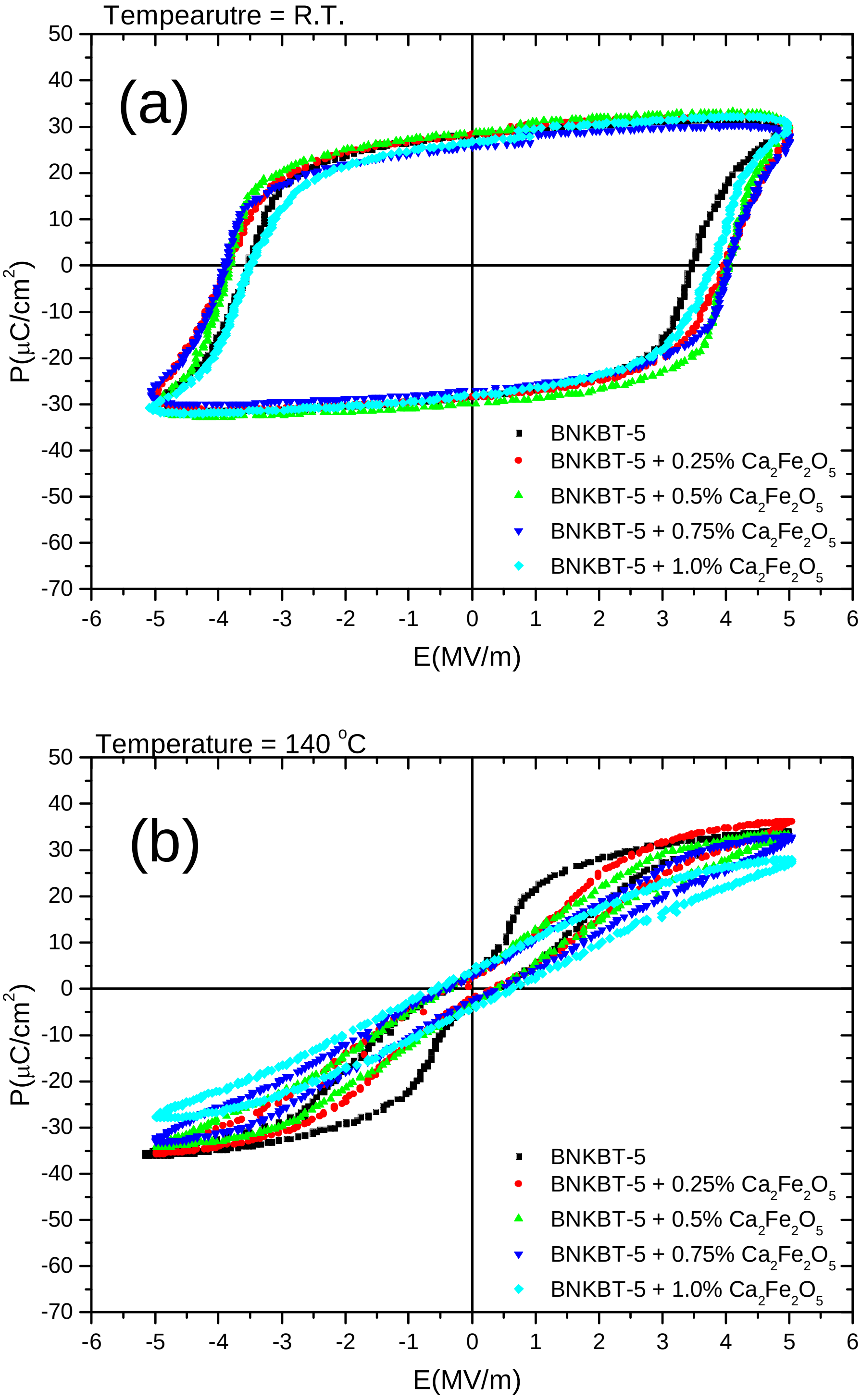
Tempearutre = R.T.
(a)
P(μC/cm2)
E(MV/m)
50
40
30
20
10
0
-10
-20
-30
-40
-50
-60
-70
-6
-5
-4
-3
-2
-1
0
1
2
3
4
5
6
BNKBT-5
BNKBT-5 + 0.25% Ca2Fe2O5
BNKBT-5 + 0.5% Ca2Fe2O5
BNKBT-5 + 0.75% Ca2Fe2O5
BNKBT-5 + 1.0% Ca2Fe2O5
Temperature = 140 °C
(b)
P(μC/cm2)
E(MV/m)
BNKBT-5
BNKBT-5 + 0.25% Ca2Fe2O5
BNKBT-5 + 0.5% Ca2Fe2O5
BNKBT-5 + 0.75% Ca2Fe2O5
BNKBT-5 + 1.0% Ca2Fe2O5

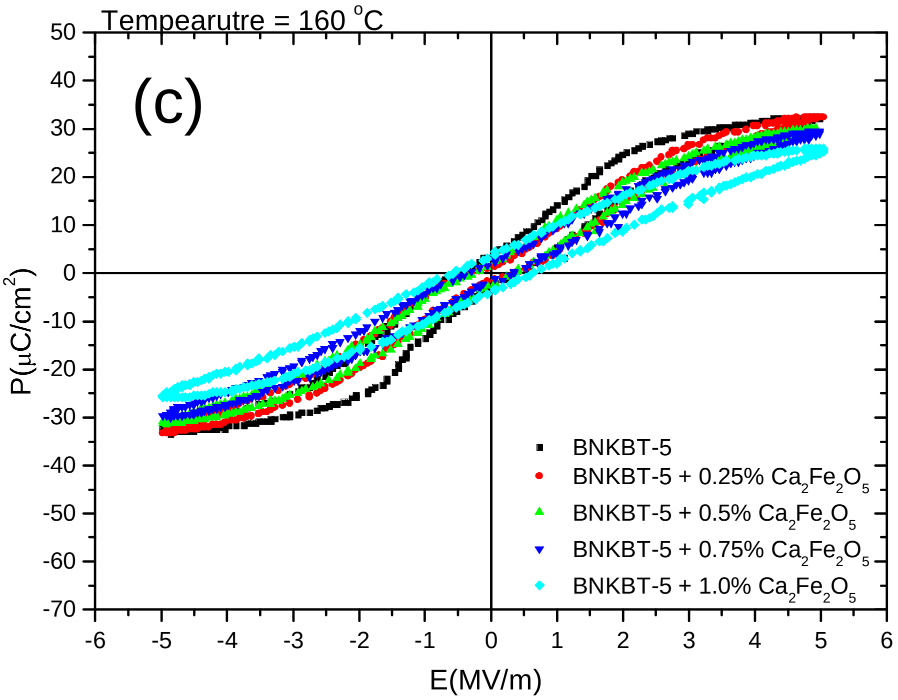

Figure 3.18 Ferroelectric P-E loops of BNKBT-5 doped with different amounts of $Ca_2Fe_2O_5$ measured at (a) room temperature, (b) 140 °C and (c) 160 °C, respectively.

The temperature dependence of relative permittivity ε_r and dielectric loss tanδ at 100 kHz with various doping concentration of $Ca_2Fe_2O_5$ in BNKBT-5 are shown in Figure 3.19. All compositions have similar Curie temperature, which is ~300 °C except for the composition with 1 mol% $Ca_2Fe_2O_5$ which has T_c ~290 °C. The T_c does not have a significant change upon doping of $Ca_2Fe_2O_5$. $Ca_2Fe_2O_5$ doping shifts the T_d of BNKBT-5 to a lower temperature, but the reduction is not as significant as adding CeO_2. The T_d reduces to a minimum value of ~95 °C when 1 mol% of $Ca_2Fe_2O_5$ has been added. Based on this information, it is relatively easy to explain the observation of normal hysteresis loops at room temperature and antiferroelectric-like loops above 140 ^{o}C for all the compositions doped with $Ca_2Fe_2O_5$.

The frequency dependence of ε_r and tanδ is shown in Figure 3.20 with the frequency range of 1 mHz to 100 kHz. All compositions have a similar performance beyond 1 kHz. Both the relative permittivity ε_r and the dielectric loss tanδ decreases gradually with increasing doping level of $Ca_2Fe_2O_5$ at 1 kHz (Figure 3.21). This shows that the $Ca_2Fe_2O_5$ doping does not increase the dielectric loss of the BNKBT-5 system.

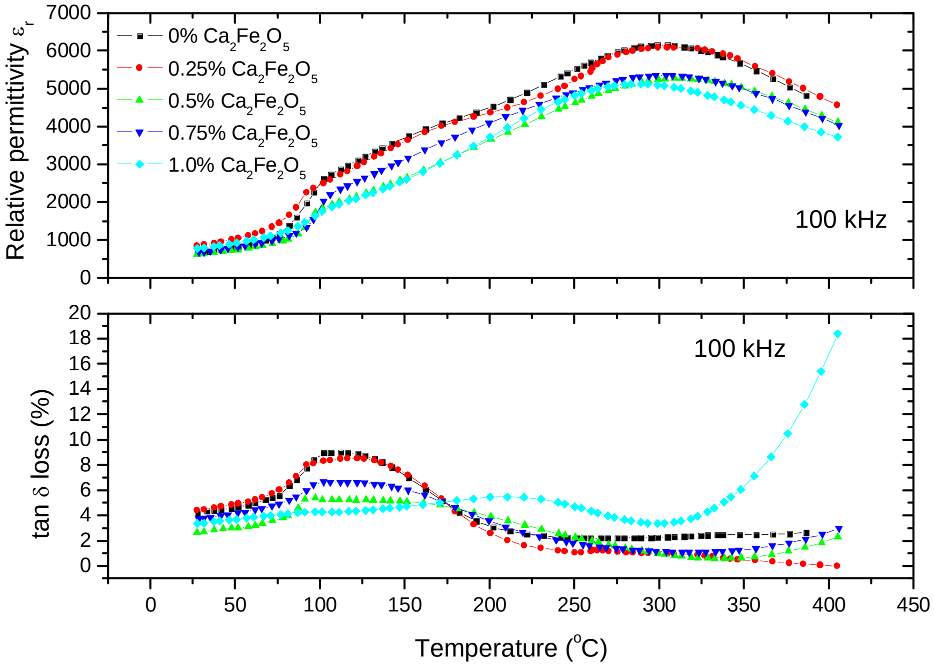

Figure 3.19 Temperature dependence of relative permittivity ε_r and dielectric loss tanδ at 100 kHz with various amounts of $Ca_2Fe_2O_5$.

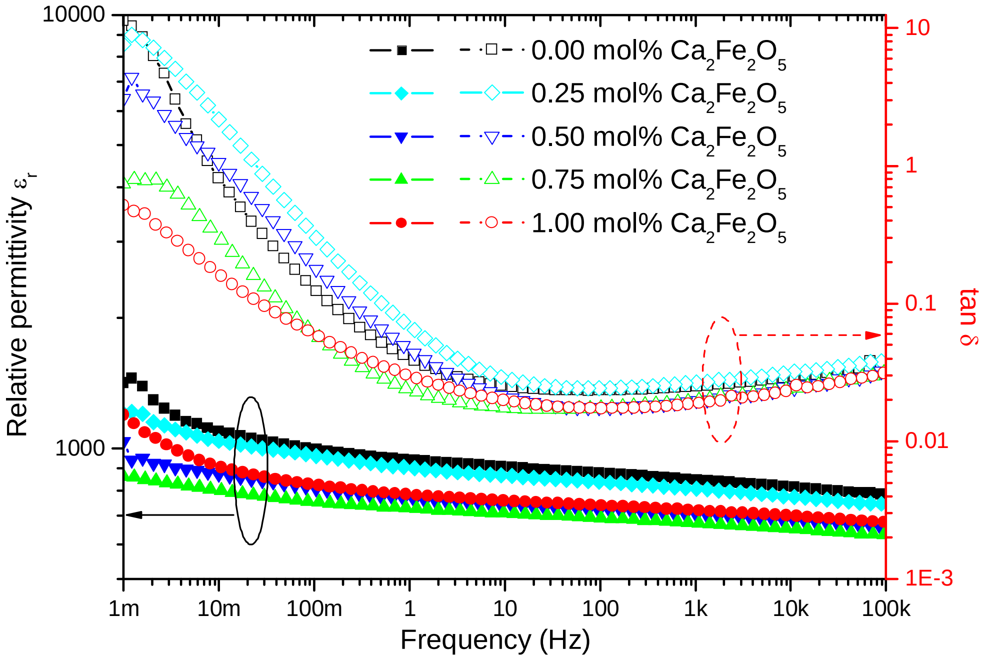

Figure 3.20 Frequency dependence of relative permittivity ε_r and dielectric loss tanδ of BNKBT-5 doped with $Ca_2Fe_2O_5$ measured at room temperature from 1 mHz to 100 kHz

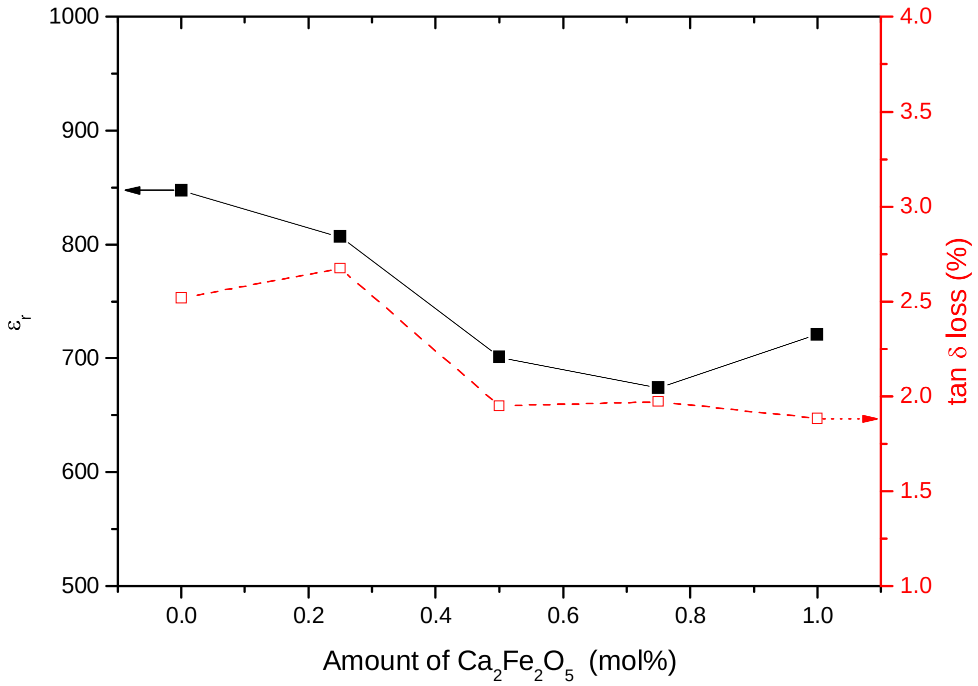

Figure 3.21 Dielectric properties of BNKBT-5 doped with various amounts of $Ca_2Fe_2O_5$ measured at 1 kHz.

Figure 3.22 reports the piezoelectric properties of BNKBT-5 with $Ca_2Fe_2O_5$ as dopant. Both electromechanical factors and mechanical quality factors increase as the doping level increases up to 0.5 mol% $Ca_2Fe_2O_5$. The electromechanical quality factors, k_p and k_t, reach their peak values of 0.35 and 0.48 at 0.25 mol% and 0.5 mol%, respectively. Both of them drop rapidly as the doping level exceeds 0.5 mol%. The mechanical quality factors in both radial and thickness modes have the peak values at 0.75 mol% doping which show over 70% and 100% increment, respectively, compared with pure BNKBT-5. But this effect disappeared for higher doping level. The piezoelectric d_{33} constant is found to be decreasing when doping with $Ca_2Fe_2O_5$.

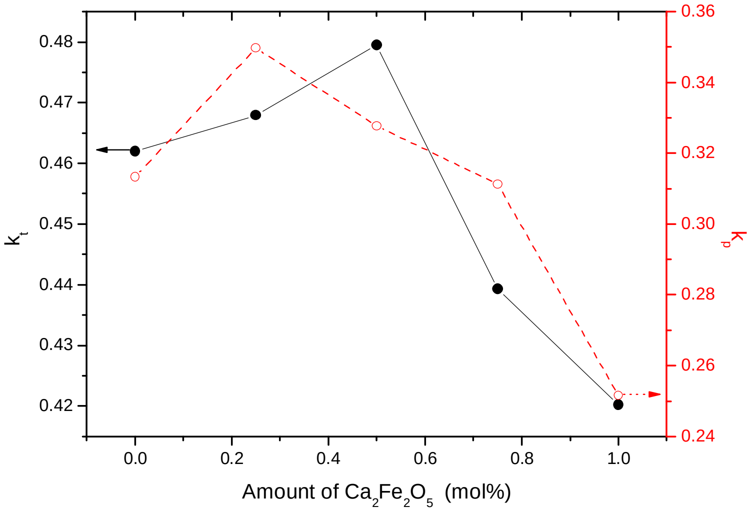

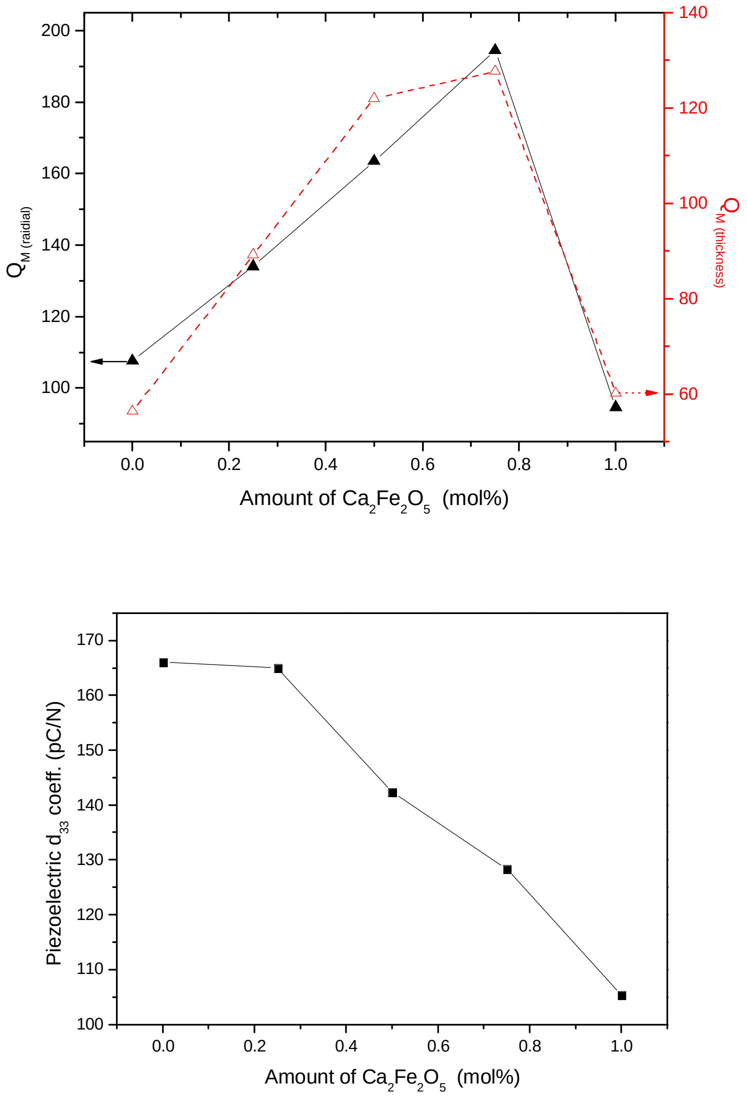

Figure 3.22 Piezoelectric properties of BNKBT-5 doped with different amounts of $Ca_2Fe_2O_5$.

The effect of $Ca_2Fe_2O_5$ in BNKBT-5 is a complex effect caused by both Ca^{2+} and Fe^{3+}. Firstly, Ca^{2+} has an ionic radius of 1.06Å, which is close to the ionic radius of both Bi^{3+}(1.03Å) and Na^{+}(1.02Å), and would substitute into the A sites occupied by Bi^{3+} and/or Na^{+}. This changes properties of the piezoelectric ceramics but maintains its perovskite structure. According to the elemental substitution experience in PZT, the experimental results show that (1) the Curie temperature is reduced slightly and k_p is increased slightly. (2) If the degree of elemental substitution is too high, the properties of the ceramics will be degarded. (3) Substitution may cause an increase in the density in PZT ceramics, owning to the fluxing effect of Ca^{2+} ions during the sintering period which facilitates the process of densification (Xu 1991). Secondly, Fe^{3+}(with ionic radius of 0.67Å) are commonly used in PZT as hard doping which occupy the B sites in the perovskite structure as the ionic radius of Ti^{4+} is 0.68Å. Hard doping changes the PZT properties, i.e., lowers the relative permittivity and dielectric loss, increases coercive field and Q_M and slightly lower k_p and d_{33}. Based on the finding of both calcium and iron ions on PZT, a very similar finding also appears in BNKBT-5 system with the doping of $Ca_2Fe_2O_5$. The characteristics such as improving sintering ability and density (by Ca^{2+}), lowering relative permittivity, and dielectric loss (by Fe^{3+}), increasing the coercive field and Q_M (by Fe^{3+}) etc. Based on the experimental results, it can be stated that $Ca_2Fe_2O_5$ has complex effect in improving the BNKBT-5 system for better mechanical properties and piezoelectric properties.

0.995 BNKBT-5 – 0.005 $Ca_2Fe_2O_5$ has the best properties in the system which has a relatively high d_{33} constant and has good mechanical properties.

3.2.3.3. (0.90-x) $(Bi_{0.5}Na_{0.5})TiO_3$ – $0.05(Bi_{0.5}K_{0.5})TiO_3$ – $(x)(Bi_{0.5}Li_{0.5})TiO_3$ – $0.05BaTiO_3$ system with x ranged from 0 to 2.5 mol%. (BNKLBT-100x)

Figure 3.23 shows density measurement results of the BNKLBT-100x system. The density of the samples is around 5750-5850 kg/m^3. From the SEM micrographs in Figure 3.24, dense samples without any pores can be observed. The average grain size is ~4-5 μm.

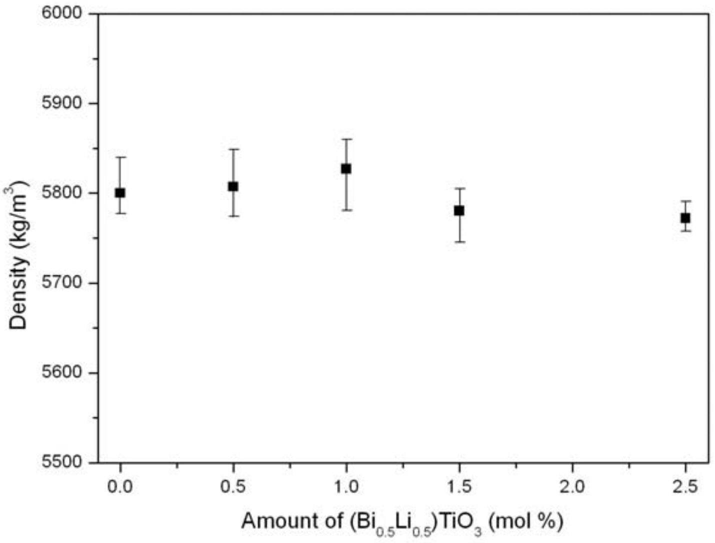

Figure 3.23 Density of the BNKLBT-(100x) system.

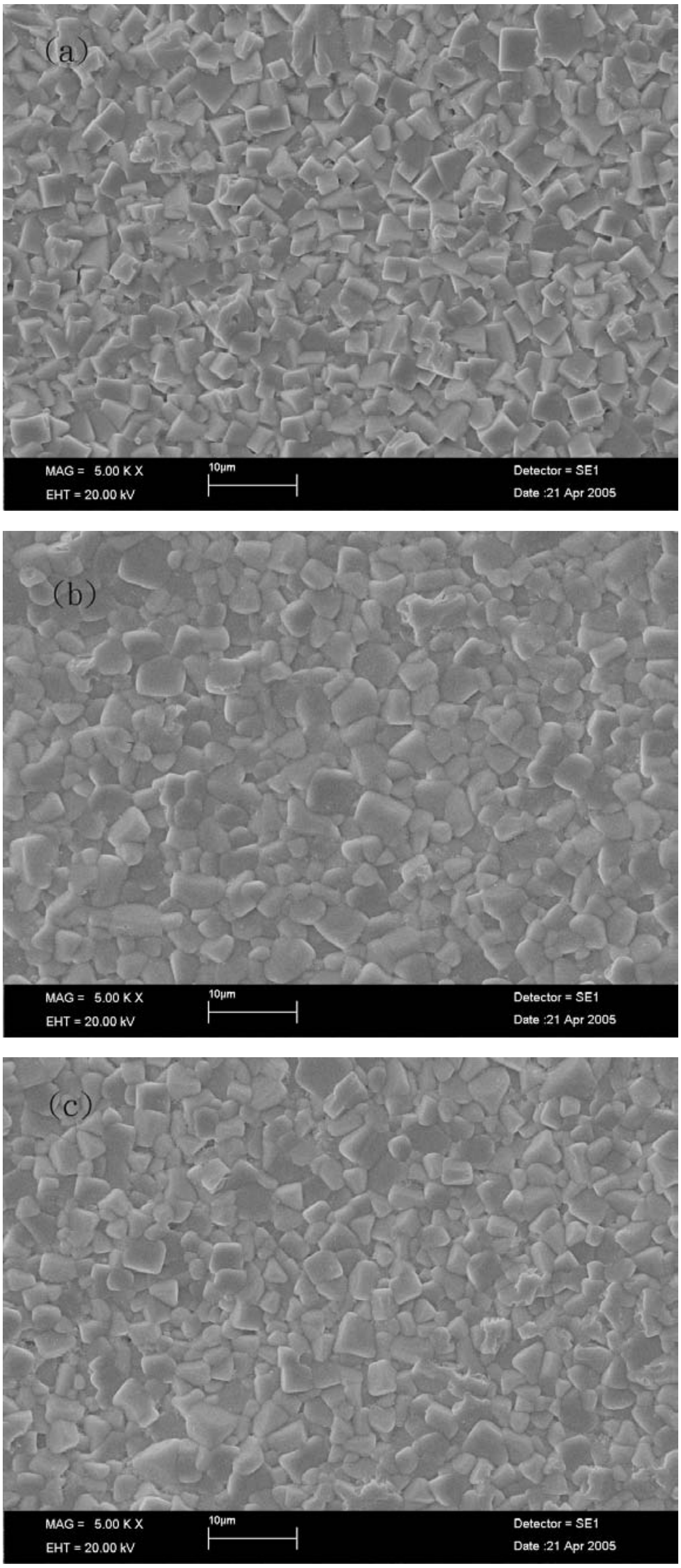
(a)
MAG = 5.00 K X
EHT = 20.00 kV
10μm
Detector = SE1
Date :21 Apr 2005
(b)
MAG = 5.00 K X
EHT = 20.00 kV
10μm
Detector = SE1
Date :21 Apr 2005
(c)
MAG = 5.00 K X
EHT = 20.00 kV
10μm
Detector = SE1
Date :21 Apr 2005

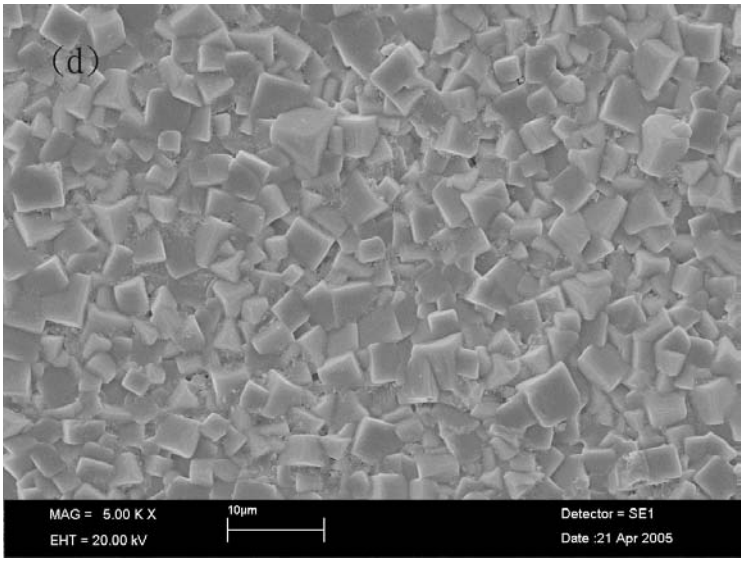

Figure 3.24 SEM micrographs of the BNKLBT-100x system with different doping amounts and sintered at 1170 ^{o}C, (a) x = 0.5 mol%, (b) x = 1 mol%, (c) x = 1.5 mol% and (d) x = 2.5 mol%, respectively.

XRD patterns of the BNKLBT-100x system are shown in Figure 3.25. A pure perovskite structure can be observed in all the compositions in this system and no pyrochlore phase has been found in the samples. BNKBT-5 contains both rhombohedral and tetragonal phases which can be observed in the XRD diffraction patterns. The BLT doping increases the tetragonality of BNKBT-5 which could enhance the piezoelectric properties.

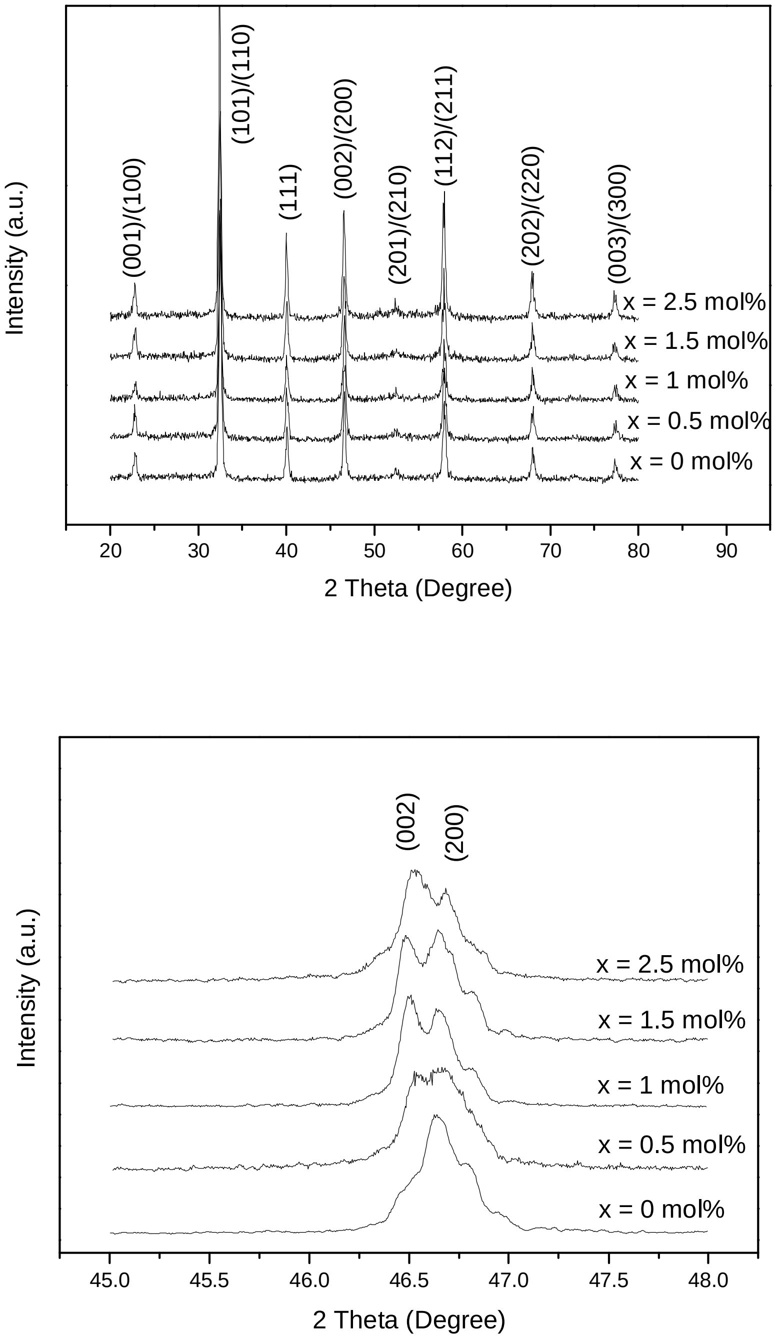

Figure 3.25 X-ray diffraction patterns of the BNKLBT-100x system sintered at 1170°C, (a) 20°-80° and (b) 45°-48°.

The ferroelectric P-E loop measurements have been conducted at room temperature, 140°C and 160 °C, respectively, and the results are shown in Figure 3.26. All the samples have normal P-E loops measured at room temperature. All BLT-doped samples have larger remnant polarization P_r than the pure BNKBT-5 and have nearly the same coercive field E_c as in BNKBT-5. The maximum P_r in BNKLBT-100x system is ~32.3 μC/cm^2 when x = 1.5 mol%, which shows 15% increment compared with P_r = 28 μC/cm^2 in pure BNKBT-5. The remnant polarization slightly decreases for further increase in doping level. For the P-E loop measurements at 140 °C and 160 °C, all the samples have antiferroelectric-like P-E loop which indicates that the measuring temperature is close to the depolarization temperature of those samples.

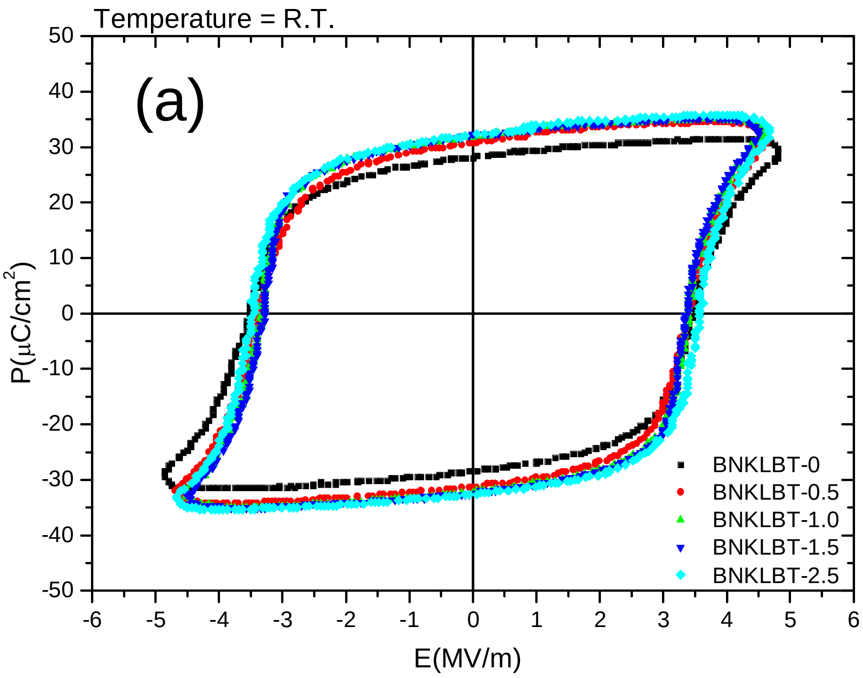

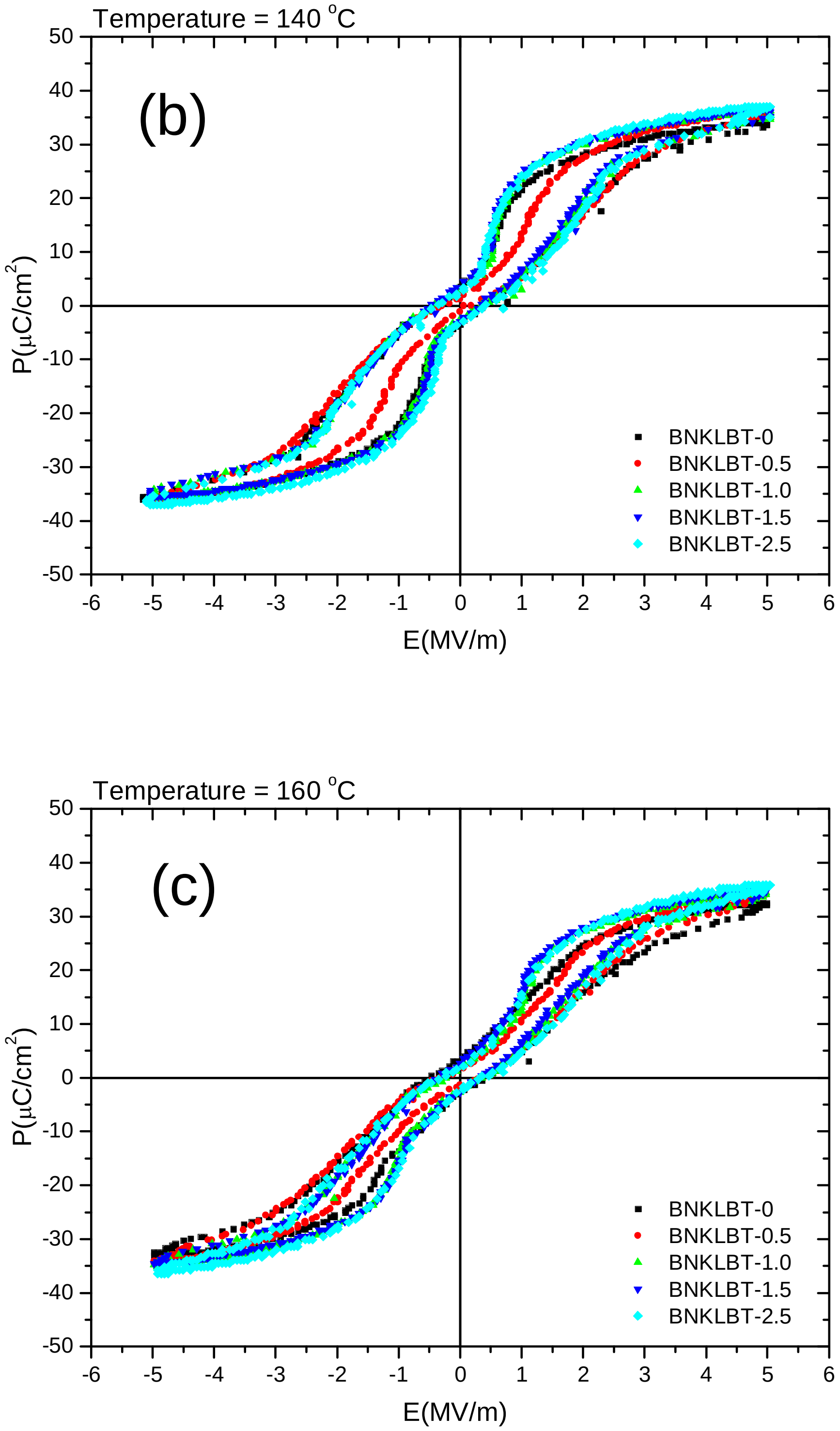

Figure 3.26 Ferroelectric P-E loop of the BNKLBT-100x system measured at (a) room temperature, (b) 140 °C and (c) 160 °C, respectively.

The temperature dependence of relative permittivity ε_r and dielectric loss tanδ at 100 kHz of the BNKLBT-100x system is shown in Figure 3.27. Increase in phase transition temperature has been observed in both Curie temperature T_c and depolarization temperature T_d. T_c slightly increases with the doping amount of BLT. T_c of the samples is around ~310 ^oC to ~320 ^oC for doping amount up to 1.5 mol%. After doping the BLT into BNKBT-5, the T_d increases gradually for a very small amount of doping (x = 0.5 mol%) and then greatly increase for more than 1 mol% BLT doping. BNKLBT-1.5 has the highest T_d in this system which is ~140 ^oC and is the highest value in our study. The antiferroelectric-like P-E loop in/over 140 ^oC is related to the relatively high T_d in this system.

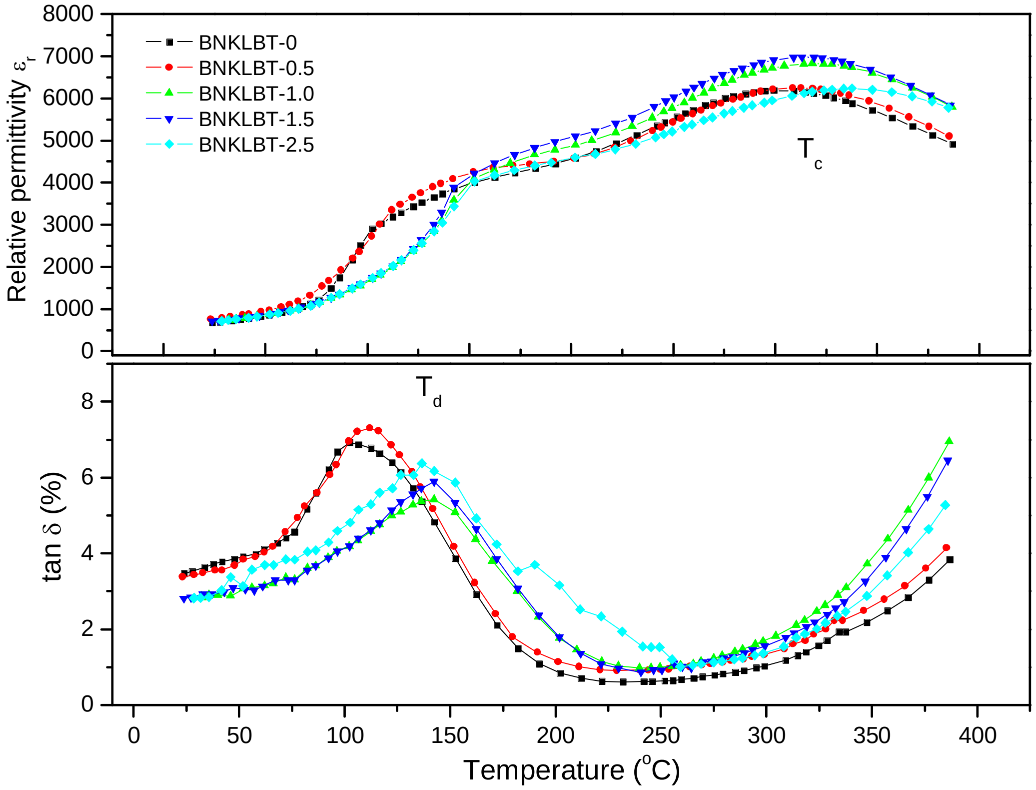

Figure 3.27 Temperature dependence of relative permittivity ε_r and dielectric loss tanδ at 100 kHz of the BNKLBT-100x system.

The frequency dependence of ε_r and tanδ is shown in Figure 3.28 in the frequency range of 1 mHz to 100 kHz. The result is similar to those in other systems presented before. Figure 3.29 shows the dielectric properties of BNKLBT-100x measured at 1 kHz. Both the relative permittivity and dielectric loss decrease with the increase in Li^+ concentration and reach the minimum value for 1 mol% Li^+ doping.

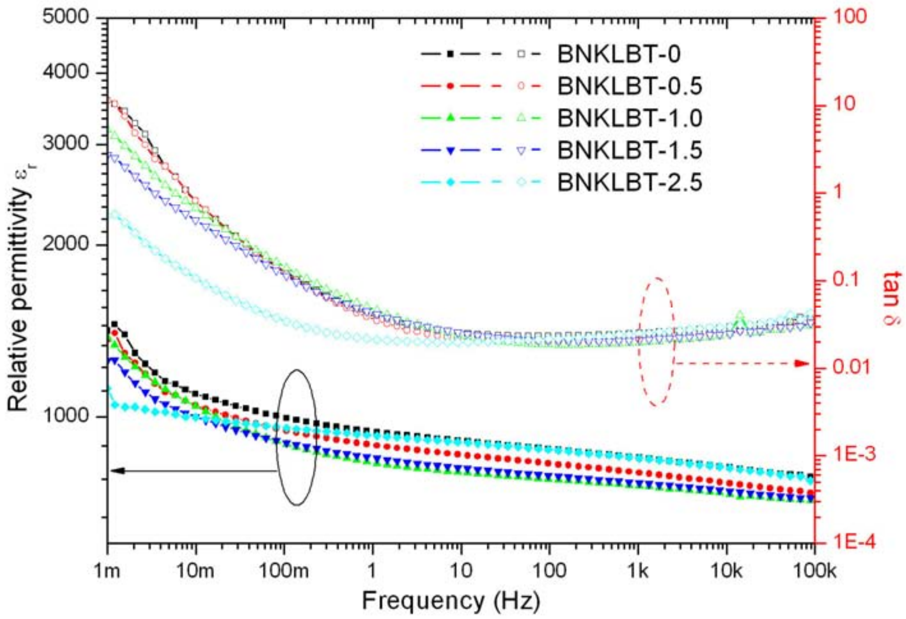

Figure 3.28 Frequency dependence of relative permittivity ε_r and dielectric loss tanδ of the BNKLBT-100x system measured under room temperature from 1 mHz to 100 kHz

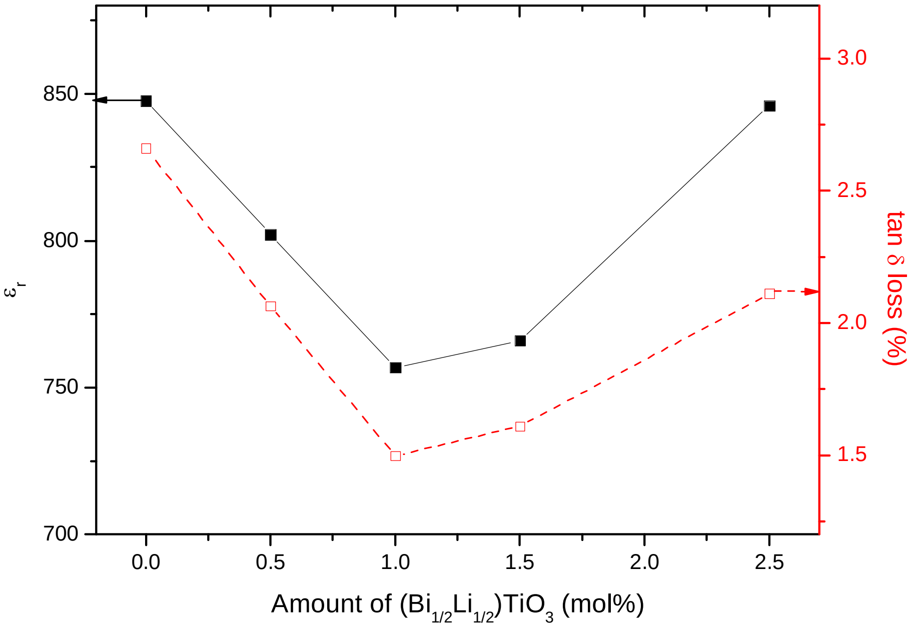

Figure 3.29 Dielectric properties of BNKBT-5 doped with various amounts of $(Bi_{0.5}Li_{0.5})TiO_3$ measured at 1 kHz.

Piezoelectric properties of the BNKLBT-100x system are shown in Figure 3.30. Both electromechanical coupling factor (k_p, k_t) and mechanical quality factor ($Q_{M(radial)}$, $Q_{M(thickness)}$) increases after doped with Li^+. Optimized properties are found in the BNKLBT-1.5 sample (1.5 mol% BLT), giving maximum k_t, $Q_{M(radial)}$ and $Q_{M(thickness)}$ values of 0.524, 142 and 102, respectively. Comparing with undoped samples, there are ~14%, 31% and ~81% increment in k_t, $Q_{M(radial)}$ and $Q_{M(thickness)}$ values, respectively. The k_t (=0.524) value is superior compared to most of the reported BNT-based lead-free materials. Another important factor, the d_{33} piezoelectric constant, does not have much variation after doping Li^+ and retains a relatively high value which ranges from 160-170 pC/N.

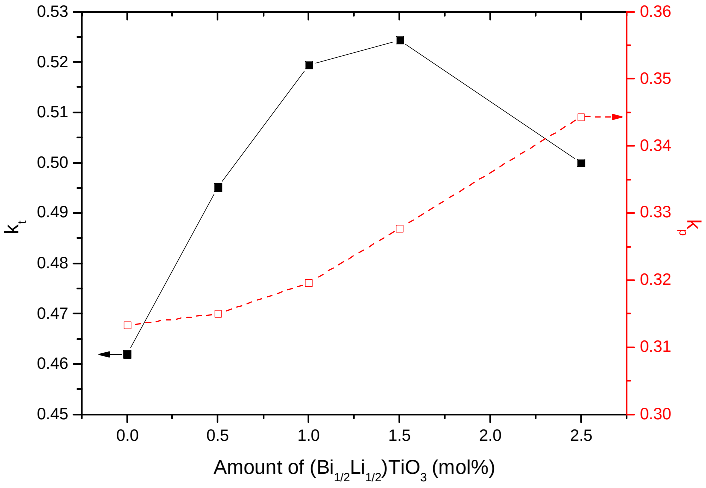

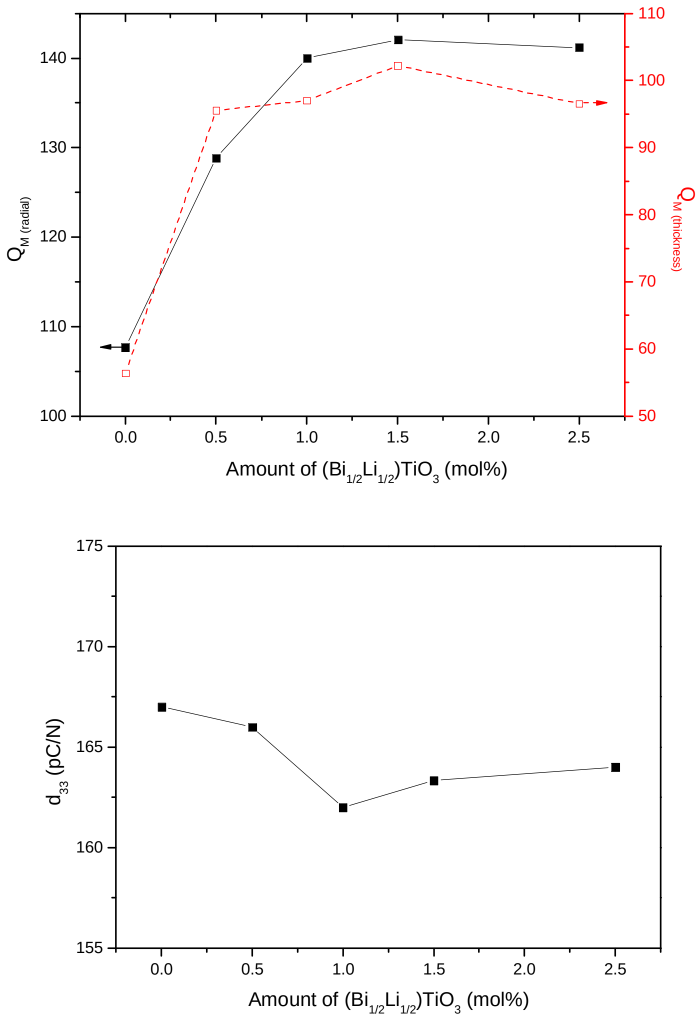

Figure 3.30 Piezoelectric properties of the BNKLBT-100x system.

Most of the piezoelectric properties and dielectric properties of BNKBT-5 have been greatly improved by doping small amount of Li^+ ions, i.e. BNKLBT-1.5 composition, to replace the Na^+ ion. The ionic radius of Li^+ is 0.76Å, which is much smaller than those ions in A-sites in the perovskite cell, for example, Na^+(1.02Å), K^+(1.38Å), Ba^{2+}(1.35Å) and Bi^{3+}(1.03Å). The presence of Li^+ ions in the perovskite structure introduces a higher degree of distortion which can improve the piezoelectric properties. Other than BNT-based lead-free ceramics, Li^+ ions were also used in sodium potassium niobate lead-free ceramics system and a great improvement in piezoelectric properties was found (Guo *et al.* 2004b). Although the detail mechanism of Li^+ in BNT-based system has not been developed, the result of this finding is promising.

The most promising composition in this system is BNKLBT-1.5 which has relatively high T_d and good overall piezoelectric properties.

3.2.3.4. Discussion

The effect of different additive/doping, including CeO_2, $Ca_2Fe_2O_5$, and $(Bi_{0.5}Li_{0.5})TiO_3$, on BNKBT-5 ceramics have been investigated. It has been found that different additives/dopings lead to different improvements in BNKBT-5, which may be in piezoelectric, ferroelectric, dielectric or mechanical properties. The most optimum composition has been chosen in each system which represents the most effective improvement of the system and they are:

(a) BNKBT-5 + 0.25 mol% CeO_2

(b) 0.995 (BNKBT-5) – 0.005 ($Ca_2Fe_2O_5$) and

(c) BNKLBT-1.5

The characteristics of each of the mentioned compositions have been presented. BNKLBT-1.5 has the most promising properties, including high remnant polarization P_r, high electromechanical coupling factors and mechanical quality factors, relatively high d_{33} constant and relatively low tanδ. Those factors are important when using them in piezoelectric devices. Another important factor is the relatively high depolarization temperature T_d which can broaden the useable range in different applications. BNKLBT-1.5 is a promising candidate to be used in different device applications and the results will be presented in subsequent Chapters.

3.3. CHARACTERIZATION OF BNKBT-5 AND BNKLBT-1.5 LEAD-FREE CERAMICS

In the previous section, the properties of BNKBT-5 added with different additives/dopings were investigated and it has been found that BNKLBT-1.5 has the most promising properties which can be used on different device applications. It is important to obtain more information on this material which is useful for designing different devices. For example, those data will be used for finite element analysis in the subsequence Chapter. Based on this point of view, a characterization of BNKBT-5 and BNKLBT-1.5 were done based on a resonance technique (IRE 1961; ANSI/IEEE 1987). With the measured resonance and anti-resonance frequencies of specified vibrational modes, most properties of the ceramics can be evaluated. Five samples with specified shapes and orientations, including a circular disc, a long bar, a thin rod, a thin square plate and a thin shear plate, were used in these measurements (Berlincourt *et al.* 1964). The samples were cut by a dicing saw (Disco DAD321). The assumption for specific samples is listed in Table 3.1. The dimensions of the BNKBT-5 and BNKLBT-1.5 samples are listed in Tables 3.2 and 3.3, respectively. All the measurements are based on the IEEE standard and the result of both BNKBT-5 and BNKLBT-1.5 are summarised in Table 3.4.

Table 3.1 The assumption for specific samples. [L – length, W – width, t – thickness, d - diameter]

Sample	Assumption
Circular Disc	d >> t
Square Plate	L, W >> t
Thin Rod	t >> L, W
Long Bar	L >> W, t
Shear plate	L, W >> t

Table 3.2 The dimensions of the BNKBT-5 samples used in resonant characterization.

Sample	Length (mm)	Width (mm)	Thickness (mm)	Resonance frequency, f_r (kHz)	Anti-resonance frequency, f_a (kHz)
Disc	Diameter = 10.14			295.125	309.525
Square plate	6.6	6.6	0.675	3500	3880
Thin Rod	-	-	1.85	213.25	269.5
Long Bar	8.55	-	0.819	265.269	271.175
Shear plate	-	-	0.78	2039	2214

Table 3.3 The dimensions of the BNKLBT-1.5 samples used in resonant characterization.

Sample	Length (mm)	Width (mm)	Thickness (mm)	Resonance frequency, f_r (kHz)	Anti-resonance frequency, f_a (kHz)
Disc	Diameter = 19.05		-	154.63	160.82
Square plate	10.21	10.21	1.025	2533.12	2887.38
Thin Rod			4.62	599.44	698.88
Long Bar	13.5	-	-	168.838	171.313
Shear plate	-	-	0.841	1740.88	1912.81

Table 3.4 Elastic, piezoelectric, dielectric constant and electromechanical coupling coefficients for BNKBT-5 and BNKLBT-1.5 samples measured by the resonance technique at room temperature.

Materials Parameters	**BNKBT-5**	**BNKLBT-1.5**
Electromechancial coupling factor		
k_{33}	0.504	0.553
k_{31}	-0.230	-0.188
k_{15}	0.424	0.451
k_t	0.487	0.519
k_p	0.313	0.309
Constant electric field elastic compliance ($10^{-12}m^2N^{-1}$)		
s_{11}^E	8.265	8.369
s_{12}^E	-2.217	-2.33
s_{13}^E	-3.955	-2.042
s_{33}^E	13.117	8.171
s_{44}^E	17.394	21.086
s_{66}^E	20.964	21.398
Constant electric displacement elastic compliance ($10^{-12}m^2N^{-1}$)		
s_{11}^D	7.826	8.073
s_{12}^D	-2.656	-2.626
s_{13}^D	-2.746	-1.181
s_{33}^D	9.789	5.669
s_{44}^D	14.26	16.801
s_{66}^D	20.964	21.398
Constant stress relative permittivity		
$\varepsilon_{33}^T/\varepsilon_o$ at 1 kHz	974.49	684.32
$\varepsilon_{11}^T/\varepsilon_o$ at 1 kHz	877.22	404.00
Constant strain relative permittivity		
$\varepsilon_{33}^S/\varepsilon_o$ at $2*f_p$	597.36	443.99
$\varepsilon_{11}^S/\varepsilon_o$ at $2*f_p$	378.47	258.27

Constant electric field elastic stiffness (10^9 Nm^{-2})		
c_{11}^E	184.198	146.376
c_{12}^E	88.797	52.907
c_{13}^E	79.913	41.792
c_{33}^E	125.88	147.281
c_{44}^E	57.49	47.425
c_{66}^E	47.701	46.734
Constant electric displacement elastic stiffness (10^9 Nm^{-2})		
c_{11}^D	185.485	147.662
c_{12}^D	90.083	54.193
c_{13}^D	5.783	27.29
c_{33}^D	161.327	201.457
c_{44}^D	70.127	59.52
c_{66}^D	47.701	46.734
Piezoelectric strain constant (10^{-12} CN^{-1})		
d_{33}	160.737	123.104
d_{31}	-58.423	-42.361
d_h	43.892	38.382
d_{15}	164.417	123.751
Piezoelectric voltage constant (10^{-3} m^2C^{-1})		
g_{33}	20.704	20.327
g_{31}	-7.525	-6.996
g_{15}	19.065	34.624
g_h	5.654	6.337
Mechanical quality factor		
Q_M	32.341	55.437
Q_E	29.751	60.54
Piezoelectric stress constant (Cm^{-2})		
e_{33}	10.896	14.59
e_{31}	-8.601	-3.905
e_{15}	9.451	5.869

Piezoelectric stiffness constant (10^9 NC^{-1})		
h_{33}	3.253	3.713
h_{31}	-1.954	-0.857
h_{15}	1.337	2.061
Frequency constant (Hz-m)		
N_1	2268	2279
N_{3t}	2362	2596
N_5	1591	1464
N_p	2993	2946
Acoustic velocity (ms^{-1})		
υ_{33}^D	4168	5539
υ_{33}^E	3601	4613
υ_{3t}^D	5238	5919
υ_{3t}^E	4627	5061
Acoustics Impedance (MRayl)	30.80	34.04
Poisson's ratio	0.268	0.278
Young modulus Y (10^{10} N m^{-2})	12.10	12.24

CHAPTER 4 LEAD-FREE PIEZOELECTRIC DEVICE APPLICATION 1: ACCELEROMETER

4.1. INTRODUCTION

Accelerometer or acceleration sensor is widely used in different applications to measure acceleration. The industrial applications for accelerometers include machinery vibration monitoring to diagnosis, for example, out-of-balance conditions of rotating parts. An accelerometer-based vibration analyzer can detect abnormal vibrations, analyze the vibration signature, and help identify its cause. Another application is in structural testing, where the presence of a structural defect, such as a crack, bad weld, or corrosion can change the vibration signature of a structure. The structure may be the casing of a motor or turbine, a reactor vessel, or a tank. The test is performed by striking the structure with a hammer to excite the structure with a known force function. This generates a vibration pattern that can be recorded, analyzed, and compared to a reference signature.

Typically, accelerometers use the mass of an element to convert acceleration into force, in accordance with Newton’s second law. Such an accelerometer contains an inertial mass, a spring-like system, a force or displacement sensing element and a damping element (Fraden 1997). Piezoelectric accelerometers contain piezoelectric materials sandwiched between the seismic mass and the sensor housing. The acceleration of the inertial mass generates a force on the crystal and thereby induces charge, which is detected by a charge amplifier and the acceleration can be found.

In this study, detailed descriptions of the prototype accelerometers are given. These include the accelerometer design, accelerometer components and its materials requirement. Three different materials were used as the transduction element in the prototype accelerometer, including BNKBT-5, BNKLBT-1.5 and APC PZT 840 (supplied by American Piezoceramics). The electrical performance of the prototype accelerometers is characterized using an impedance analyzer. The sensitivity of accelerometer is calibrated by a back-to-back method.

4.2. BASIC ACCELEROMETER DESIGN AND COMPONENTS

In this Section, the basic designs of accelerometer are reviewed and the practical designs are also presented. In a practical accelerometer, beside the sensing or transduction elements, there are also other components. The selection of materials for these components is important as they will affect the performance of the accelerometer. The components are listed in this Section together with the materials used in the prototype accelerometer.

4.2.1. DESIGN OF ACCELEROMETER

Accelerometers or acceleration sensors are basically force sensors with an attached mass. According to the Newton’s second law of motion ($F = m \cdot a$), the measured force is proportional to the acceleration. The mass m is constant and usually called “seismic mass”, a term taken from seismometers used for detecting earthquake. Force F is produced when the seismic mass is being accelerated and the force can be measured by the accelerometer. The relationship between F and a can be determined once after the sensor calibration.

Both piezoelectric accelerometers and force sensors are characterized by having a transduction (or sensing) element made of a piezoelectric material. In a piezoelectric accelerometer, the measurand is transmitted directly through the solid, rigid metal parts to the transduction element. The mechanical stress induces electric charges as output through the direct piezoelectric effect. Piezoelectric elements exploiting the longitudinal or shear piezoelectric effect are usually circular, ring-shaped or square. In all piezoelectric elements cut for the longitudinal effect and in most elements cut for the shear effect, the faces on which the force is applied and the faces on which the electric charges appear are the same. In some materials and for special applications, it is also possible to collect the electric charges from faces other than the mechanically loaded ones. A schematic diagram of some piezoelectric elements with different shapes is shown in Figure 4.1.

In some sensor configurations, the piezoelectric element is fitted between 2 metal blocks which transmit the force to the sensing element. These metal blocks usually also serve as electrodes to collect the output electric charges. A model of such a piezoelectric force sensor is shown in Figure 4.2. The piezoelectric element P in the form of a circular plate is sandwiched between 2 metal plates M1 and M2. The radius r_P of the piezoelectric element is equal to the radius of the 2 plates. The thickness of the piezoelectric element is l_P, the height of the plates $l_{M1} = l_{M2}$.

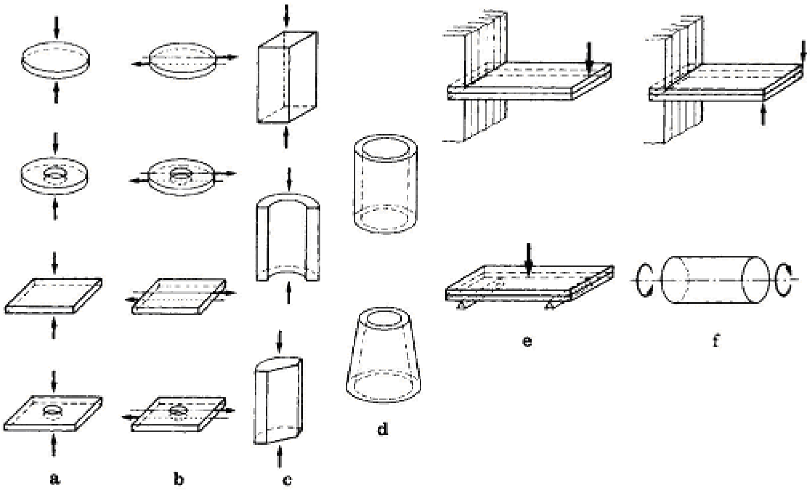

Figure 4.1 Piezoelectric transduction elements (a) plate-shaped elements for the longitudinal effect, (b) plate-shaped elements for the shear effect, (c) rod-shaped elements for the shear or torsional effect, (d) elements in the shape of a hollow cylinder or a truncated cone, (e) bimorph elements as bending beams (exploiting the bending effect), (f) torsion-sensitive elements (exploiting the shear or torsional effect) (Gautschi 2002).

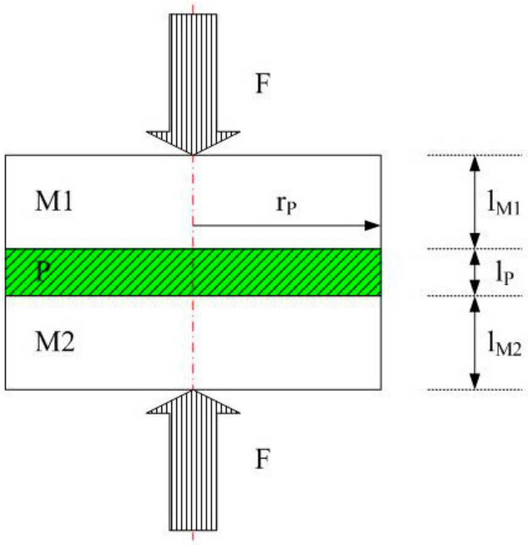

Figure 4.2 Model of a basic sensor with a piezoelectric element.

In this simple configuration, if some assumptions are made, including (1) the force being applied normal to the end face and distributed evenly over the surface. (2) Only compressive force is transmitted by the plates to the piezoelectric element and (3) homogenous charge distribution is produced when stress is applied. Then, for a piezoelectric element with thickness along the z-axis, the only stress component on the piezoelectric element is:

$$T_3 = \frac{F}{\pi r_P{}^2} \qquad \textbf{(4.1)}$$

Provided the electrodes are short-circuited, the electric field strength E = 0 and from the linear piezoelectric equation of state, the electric displacement in the piezoelectric element can be expressed as:

$$D_3 = d_{33} T_3 = \frac{d_{33} F}{\pi r_P{}^2} \qquad \textbf{(4.2)}$$

The charge Q on the electrodes is obtained by multiplying Equation (4.2) with the area of the electrode, which is $\pi r_p{}^2$ and therefore:

$$Q = d_{33} F \qquad \textbf{(4.3)}$$

The measured charge is proportional to the acting force and the proportionality constant is the piezoelectric coefficient d_{33} of the material which determines the sensitivity of the sensor. Since acceleration is proportional to the acting force, so it is also proportional to the measured charge. Hence, using a material with a higher piezoelectric d_{33} coefficient can increase the sensitivity of the compressive type force sensor.

The simple model shown in Figure 4.2 is a simplified and idealized model which needs to be modified before it can be used in practical application. A common way to fix the various components together is to mount the piezoelectric element under mechanical preload between the metal parts. The mechanical preload not only assures that the parts are properly fixed together but also has the important purpose of eliminating micro-gaps between the contacting faces. This configuration can provide a good linearity and the rigidity necessary for a high resonance frequency. The electric charges yielded by the piezoelectric transduction element are collected by electrodes. Usually, the ground electrode is connected to the sensor housing through one of the force transmitting parts in contact with the housing, while the other electrode is connected to the center pin of the coaxial connector. The housing or case of the sensor has 2 functions: it mechanically holds together the inner parts of the accelerometer and it protects the sensor parts against environmental influences. Thus, the essential parts of an accelerometer are: piezoelectric sensing or transduction element, electrodes, seismic mass as preloading elements, housing and connector. Detail illustration of these components will be discussed in the next Section.

Figure 4.3 shows the schematic diagram of a simple compressive type accelerometer (Gautschi 2002). The transduction element is a piezoelectric plate (1), cut for the longitudinal effect with the poling axis of each plate oriented in opposite directions. The transduction elements have been pre-stressed by a bolt (2) which serves as a very rigid spring between seismic mass (3) and base plate (4). The electrode (5) collects the electric charges yielded by the transduction element and feeds it to the connector (6). The housing (7) acts as a protection shield to the environment and having a mounting thread (8). When the base plate is accelerated, the seismic mass exerts a proportional force on the transduction element.

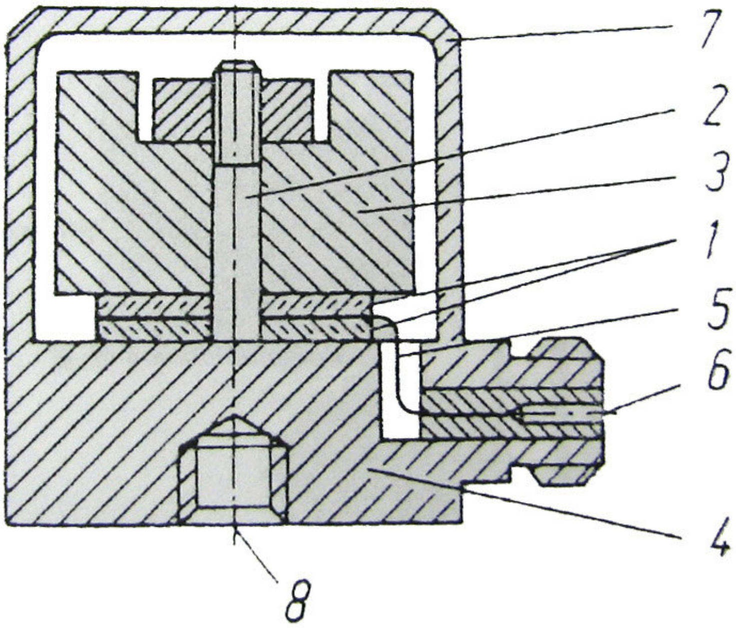

Figure 4.3 Cross-section of a simple compressive type accelerometer.

4.2.2. ACCELEROMETER COMPONENTS

As mentioned in the previous Section, the essential parts of an accelerometer are: piezoelectric sensing or transduction element, electrodes, seismic mass and/or preloading elements, housing and the connector which are briefly discussed in the following sections.

4.2.2.1. Transduction element

Piezoelectric single crystals or piezoelectric ceramics have been used as transduction elements. Quartz is a single crystal commonly used in sensors. Man-made piezoelectric ceramics are mainly based on barium titanate (BT), lead titanate (PT), and lead zirconate titanate (PZT). In this project, three different materials were used as the transduction element in the prototype accelerometer, including BNKBT-5, BNKLBT-1.5 and PZT APC 840. The PZT APC 840 rings are commercial product supplied by American Piezo Ceramics International Ltd. All lead-free ceramics were fabricated in ring-shaped and the sintered rings have outer diameter of 12.7mm, inner diameter of 5.1 mm and are 2.3mm thick. All the samples contain silver electrode and have been poled using conditions mentioned in the previous Chapter. Some important parameters are shown in Table 4.1.

Table 4.1 Some important parameters of the transduction element in the prototype accelerometer.

Sample	**BNKBT-5**	**BNKLBT-1.5**	**APC840**
Density (kg m^{-3})	5800	5780	7516
Relative permittivity ε_r	848	766	1112
tan δ loss (%)	2.66	1.61	0.75
k_t	0.462	0.524	0.357
k_p	0.313	0.328	0.59
k_{31}	0.230	0.188	0.32
s_{11}^E (x10^{-12} m^2 N^{-1})	8.265	8.369	10.62
s_{12}^E (x10^{-12} m^2 N^{-1})	-2.217	-2.33	-3.144
s_{11}^D (x10^{-12} m^2 N^{-1})	7.826	8.073	9.552
s_{12}^D (x10^{-12} m^2 N^{-1})	-2.656	-2.626	-4.209
$Q_{M(radial)}$	107.7	142.1	774.5
d_{33} (pC/N)	168	163	254
Y_{11}^E(x10^9 Nm^{-2})	120.99	110.49	94.22
Poisson's ratio	0.268	0.278	0.395
Acoustics Impedance Z_a (MRayl) In thickness (poling) direction	27.41	26.41	35.7

4.2.2.2. Electrodes

The electrodes have the function of collecting the electric charge appearing on specific surfaces of the transduction elements and feeding it to the connector of the sensor. In some design, one of the electrodes is formed by a part of the sensor housing, for example the wall of the sensor housing, and therefore connected to the seismic mass of the sensor. A thin metal foil or a vacuum-deposited metal film serves as the second electrode.

The faces of the transduction element that yield the electric charge are usually fully covered by the electrode. In all sensors which have piezoelectric elements on which the electric charges appear on the mechanically loaded surfaces, the electrodes are pressed against the piezoelectric elements by the preload to ensure good contact and maintain a constant capacitance.

Copper electrode with a donut shape was used in the prototype sensor. The copper electrode totally covered the transduction element and it was connected to the centre of a coaxial cable.

4.2.2.3. Insulating coaxial cable

In piezoelectric sensors, insulating materials in the coaxial cable which is used for carrying charges should meet specific requirements. The insulation resistance shall be over 10 TΩ for thickness of less than 1mm and surface area of a few mm^2. This value should be fairly constant with increasing temperature and/or humidity. The mechanical compressive strength should be at least about 200 N/mm^2 (Gautschi 2002).

PTFE (e.g. Teflon®) is a very good insulator for connectors and cables which is commonly used for applications at temperatures below 200 °C because their insulation is better than 1000 TΩm.

In all insulating materials the insulation resistance drops with increasing temperature. Also their mechanical properties are weakened (softening, crumbling) as temperature increases. The useful temperature range of PTFE goes up to about 200 to 250 °C. For higher temperature up to about 600 °C only ceramic insulators can be used. In ceramic insulators the insulation often drops with increasing temperature. In metal jacket cables, aluminium and magnesium oxides as well as mineral fibres and mica have been used successfully. In this project, the prototype accelerometer use PTFE (Teflon®) as the insulating material.

4.2.2.4. Accelerometer housing and preloading element

The sensor housing has several functions. It keeps out dirt and humidity and also serves as an electric shield to minimize external influence.

These requirements can mostly be met by a properly sealed housing. The housing material should be sufficiently corrosion resistant. The housing often directly serves as a preloading element and should have suitable elastic properties which would not adversely affect the force transmission. Loading faces and mounting threads are part of the housing. Therefore the housing material should have sufficient mechanical strength. Stainless steel was used as the raw material in fabricating the prototype accelerometer housing. It can provide enough hardness and has excellent rust resistance. In addition, it can be polished to good surface smoothness. The seismic mass (6.1g) using in this project is also made of stainless steel.

4.2.2.5. Connectors

Usually a piezoelectric sensor only needs a single-pin coaxial connector. In sensors with a transduction element electrically isolated from the housing (so-called ground-isolated sensors) connectors with 2 pins within the shield or coaxial connectors with 2 concentric shields (so-called biaxial connectors) are used.

The most widely used connector is the "Microdot" connector with a 10-32 Unified Fine thread (UNF thread). Numerous manufacturers have developed their own variations of this connector family and usually they are compatible amongst each other. Still it is wise to check because pin length and tolerance of the diameter may give problems or even lead to damage e.g. to the ceramic-insulated connectors on sensors when different makes are mixed.

For larger sensors, dynamometers and force plates, BNC and TNC type connectors are preferred because they are much more rugged than the "Microdot” connector. Moreover TNC connectors are water tight. In our prototype accelerometer, standard BNC connecters are used.

4.3. FABRICATION OF PROTOTYPE ACCELEROMETERS

The prototype accelerometers in this work are based on the compressive-type design with two sensing elements. The housing was fabricated in the workshop of our department. The surface smoothness of the sensors housing is important. Both the seismic mass and the base should have a mirror finishing surfaces which can greatly improve the force transmission to the sensing elements. The explosive diagram of the prototype accelerometer is shown in Figure 4.4. A screw passes through the centre of the seismic mass, electrodes and the piezoelectric ceramic rings are then attached to the metal base of the accelerometer as pre-stressing with a torque driver. The piezoelectric rings are positioned with their poling directions opposite to each other, hence the plates are connected electrically in parallel and mechanically in series. Both plates are then mechanically loaded by the same force and as they are connected electrically in parallel so the electric charges yielded by them are summed in the electrode. The electrode was joined to the centre wire of the coaxial cable to direct the signal. The prototype accelerometer contains a ~ 30 cm long, 1.17mm diameter coaxial cable. The cable has a silver-plated, copper coated steel conductor, PTFE insulation, silver plated braid and white fluorinated ethylene propylene (F.E.P.) sheath. It has a capacitance of 85 pC/m. A metal housing joined to the base of accelerometer with screw is used to protect the internal structure. Figure 4.5 shows the photograph of the prototype accelerometers with different transduction elements.

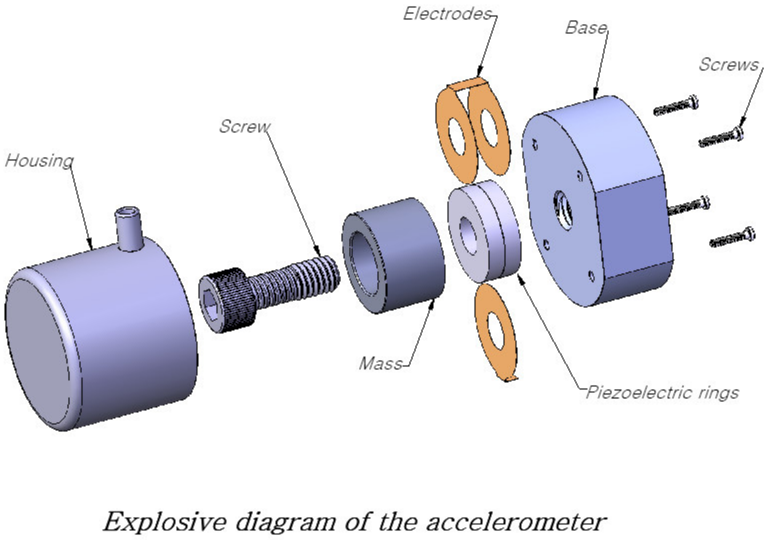

Figure 4.4 The explosive diagram of the prototype accelerometer.

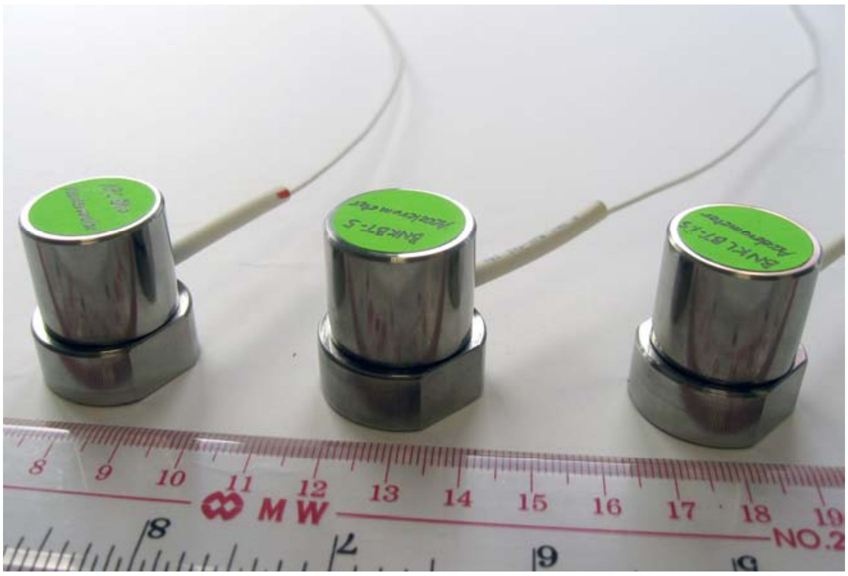

Figure 4.5 Photograph of prototype accelerometers with different transduction materials: from left to right, APC 840, BNKBT-5 and BNKLBT-1.5, respectively.

4.4. CHARACTERIZATION OF PROTOTYPE ACCELEROMETERS

4.4.1. IMPEDANCE MEASUREMENT OF PROTOTYPE ACCELEROMETERS

Piezoelectric accelerometer is an electromechanical device which can convert a mechanical vibration or force acting on the sensor to electrical signal. At certain frequencies, various vibrational modes are excited. These electromechanical resonance modes can be observed from the impedance / phase versus frequency spectrum. The sensitivity of the accelerometer depends on the piezoelectric coefficient of the transduction element. It can also be affected by the resonance modes of the transduction element. So that it is important to measure the impedance / phase versus frequency spectra of the sensor in its sensing frequency range which is up to 20 kHz.

In this study, prototype accelerometers with different transduction elements have been characterized. The measuring frequency range is from 40 Hz to 20 kHz. The impedance and phase versus frequency spectra of the 3 accelerometers show (Figure 4.6) that they have no strong resonance peak within this frequency range.

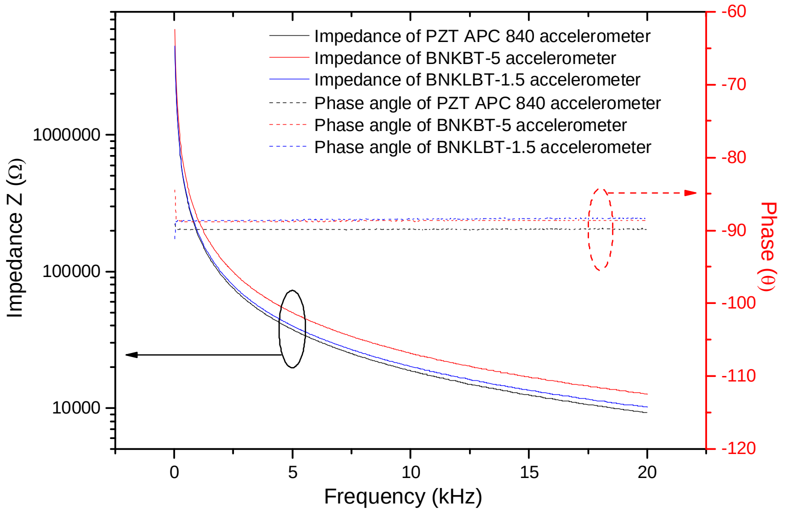

Figure 4.6 Frequency spectra of impedance and phase of the piezoelectric accelerometers with different transduction elements.

4.4.2. CAPACITANCE MEASUREMENT OF PROTOTYPE ACCELEROMETERS

Beside the impedance measurement, the capacitance versus frequency has also been measured. Capacitance measurement is also an alternative way to observe the resonance mode of the sensor (Figure 4.7).

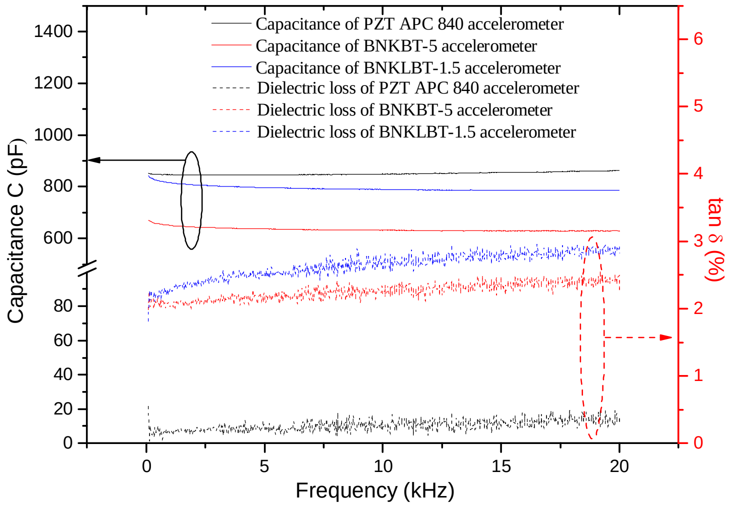

Figure 4.7 Frequency spectra of capacitance and dielectric loss of the piezoelectric accelerometer with different transduction elements.

4.5. CALIBRATION OF PROTOTYPE ACCELEROMETERS

Calibration is a test during which known values of measurand are applied to the transducer and corresponding output reading are recorded under specified conditions (ISA 1982). The sensitivity of prototype sensors can be found by suitable calibration methods. Once the relationship between the input and output quantities is calibrated, the calibration factor can be used to infer the value of the unknown variable in other measurements. If the instrument can be characterized by a linear input/output relationship, the slope of this line is called its sensitivity and has the units of the output over input signals. In this Section, the calibration method is presented and applied to calibrate the prototype sensors. Different equipments have been used to calibrate the prototype accelerometers and the detail of those equipments are described in the Appendix.

4.5.1. SELECTION OF SUITABLE PRE-STRESSING CONDITION

In our prototype accelerometer, a screw is used to connect the seismic mass, electrodes, transduction element and the base. The screw is fastened to the base and it is providing the pre-stress to the transduction element. The optimum pre-stressing condition should be found for the prototype accelerometers for optimizing the performance of the accelerometer.

A UNF 10-32 bolt is used in the prototype accelerometers. The bolt is screwed on the bass through the seismic mass by a torque driver. The pre-stress can be controlled by using different torques to fasten the bolt. The optimum condition can be found by measuring the charge output of the accelerometer under different torques. The accelerometer is mounted on the vibrator and the output measured under the same excitation with different pre-stressed condition. The result is shown in Figure 4.8. The output becomes steady when the pre-stress is higher than 50 kgf-cm. Therefore, a pre-stress of 60 kgf-cm is used in all the calibration measurement.

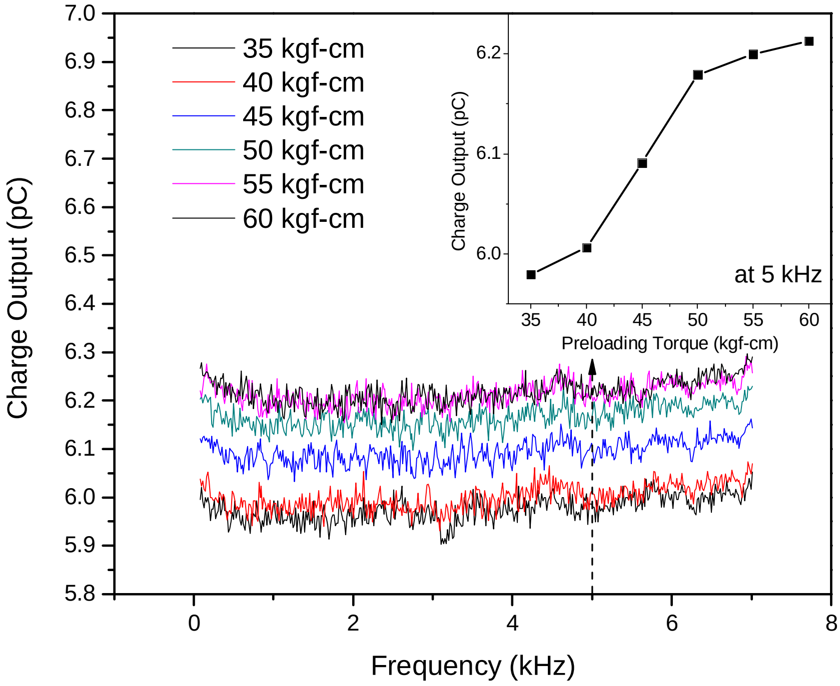

Figure 4.8 The charge output of a prototype accelerometer under different pre-stressing torques.

4.5.2. BACK-TO-BACK CALIBRATION METHOD

4.5.2.1. Methodology

The back-to-back (or comparison) calibration method is commonly used to find out the sensitivity of an unknown sensor (Harris and Piersol 2002). The sensor with unknown sensitivity is mounted with a reference sensor with known sensitivity and excited by the same amount of measurand. The output function of both sensors are measured and recorded (Figure 4.9). Transfer function is a key mathematical element denoting the transformation of input to output quantities. Transfer functions are usually the Laplace or Fourier transforms of linear differential equations relating inputs and outputs (Nachtigal 1990). The transformation is found by the multichannel analysis system (M.A.S.) using FFT. The sensitivity of the unknown sensor is then calculated as follows:

$$S_{ref} = \frac{Q_{ref}(f)}{a(f)} \tag{4.4}$$

$$a(f) = \frac{Q_{ref}(f)}{S_{ref}(f)} \tag{4.5}$$

$$S_x(f) = \frac{Q_x(f)}{a(f)} \tag{4.6}$$

where $S_x(f)$ is the sensitivity of the unknown accelerometer, $S_{ref}(f)$ is the sensitivity of reference accelerometer. $Q_{ref}(f)$ and $Q_x(f)$ are the charge out of the reference sensor and unknown sensor respectively. $a(f)$ is the acceleration.

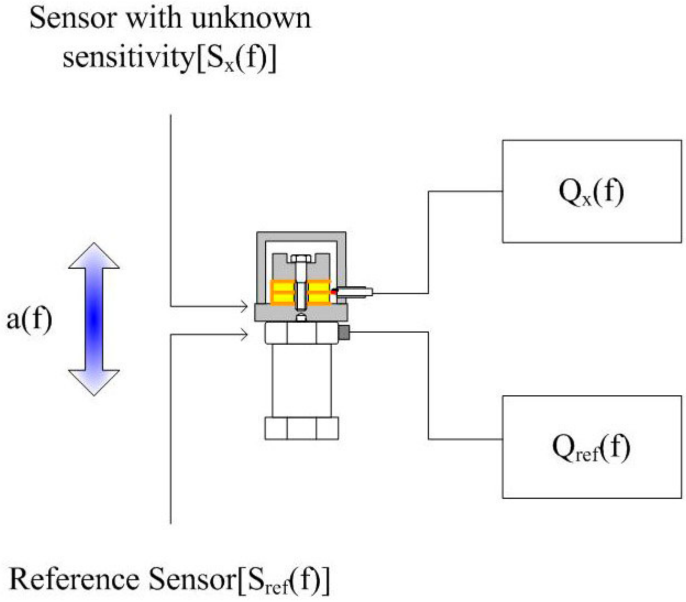

Figure 4.9 The principle of back-to-back calibration.

4.5.2.2. Calibration setup

The accelerometer calibration setup is shown in Figure 4.10. The instruments of this calibration system have been described in the Appendix. The unknown sensitivity prototype accelerometer and the reference accelerometer are mounted back-to-back on the vibrator. The vibrator is connected to the power amplifier and controlled by the generator module of the M.A.S. The prototype accelerometer is mounted on top of the B & K reference accelerometer which is used to measure the acceleration generated by the vibrator. All mountings are using steel studs or bolts. Improper mounting can change the usable frequency range of the sensor (Dally *et al.* 1993). The acceleration generated depends on the voltage applied by the generator. The signal outputs of both sensors are fed into two input modules of the M.A.S.. The calibration is performed at room temperature (25°C±3°C).

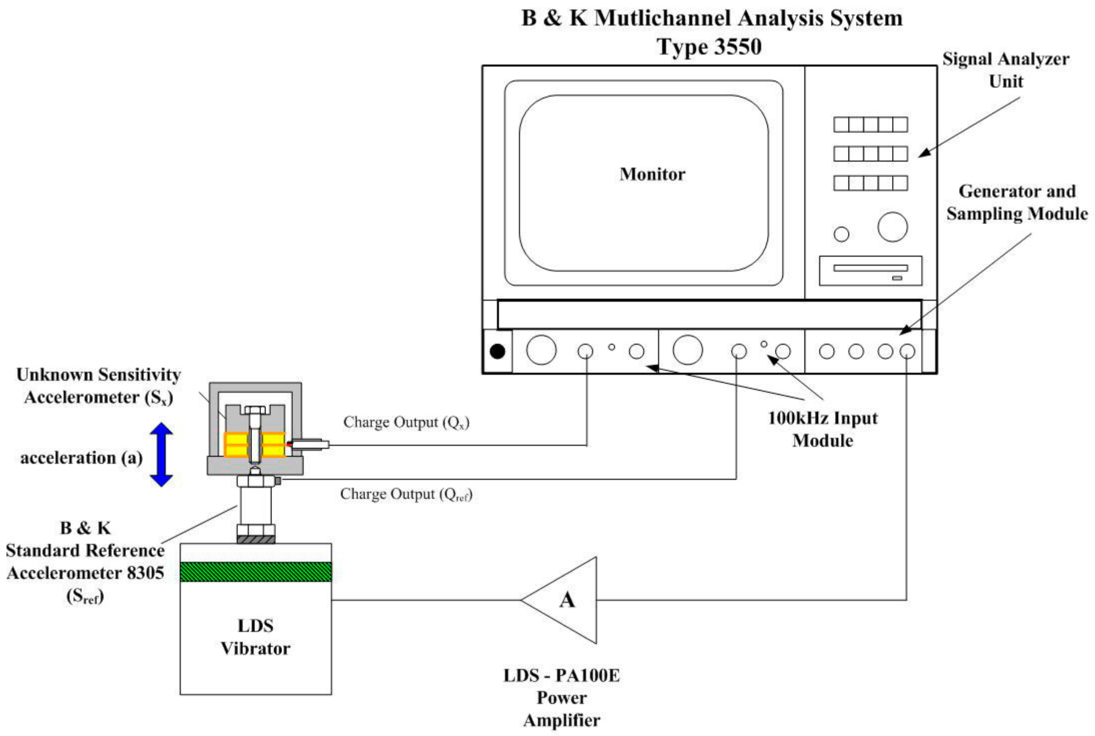

Figure 4.10 The setup of back-to-back calibration method.

4.5.2.3. Calibration results

The prototype accelerometers were mounted with the reference sensor back-to-back as shown in Figure 4.10. The charge output of the unknown accelerometer and the reference sensor were measured by the M.A.S. analyzing module.

A linear frequency range of 0-12.8 kHz and a white random vibration was used to excite the vibrator. White noise has equal energy in any frequency band of constant width over the spectrum of interest (ISO 1990). The amplitude of the vibration can be adjusted by varying the output voltage of the generator and the acceleration was measured by the reference accelerometer. The frequency response of the reference accelerometer and the prototype accelerometers with APC 840, BNKBT-5 and BNKLBT-1.5 are presented in Figures 4.11, 4.12 and 4.13, respectively. As the sensitivity of the reference accelerometer is known and already input into the M.A.S. thus the system will calculate the acceleration automatically from the measured charge.

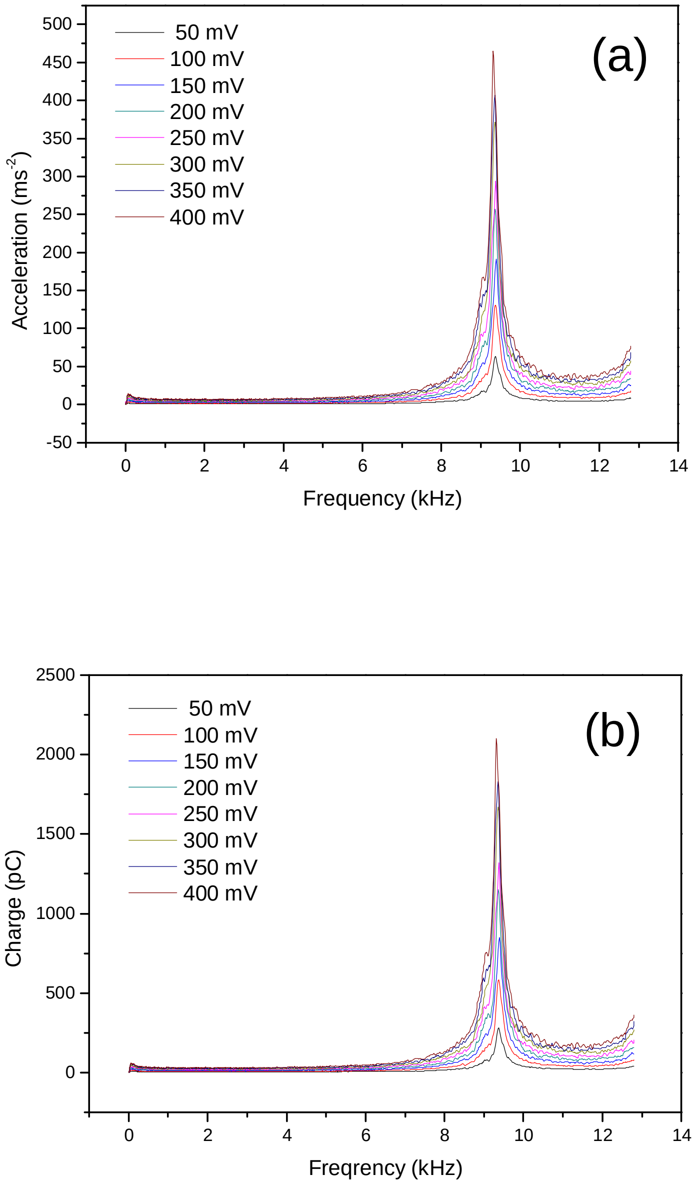

Figure 4.11 The frequency response curves under various vibration amplitudes of (a) type 8305 standard reference accelerometer $a(f) = \dfrac{Q_{ref}(f)}{S_{ref}(f)}$ and (b) prototype accelerometer with PZT APC 840 rings as transduction elements $Q_x(f)$.

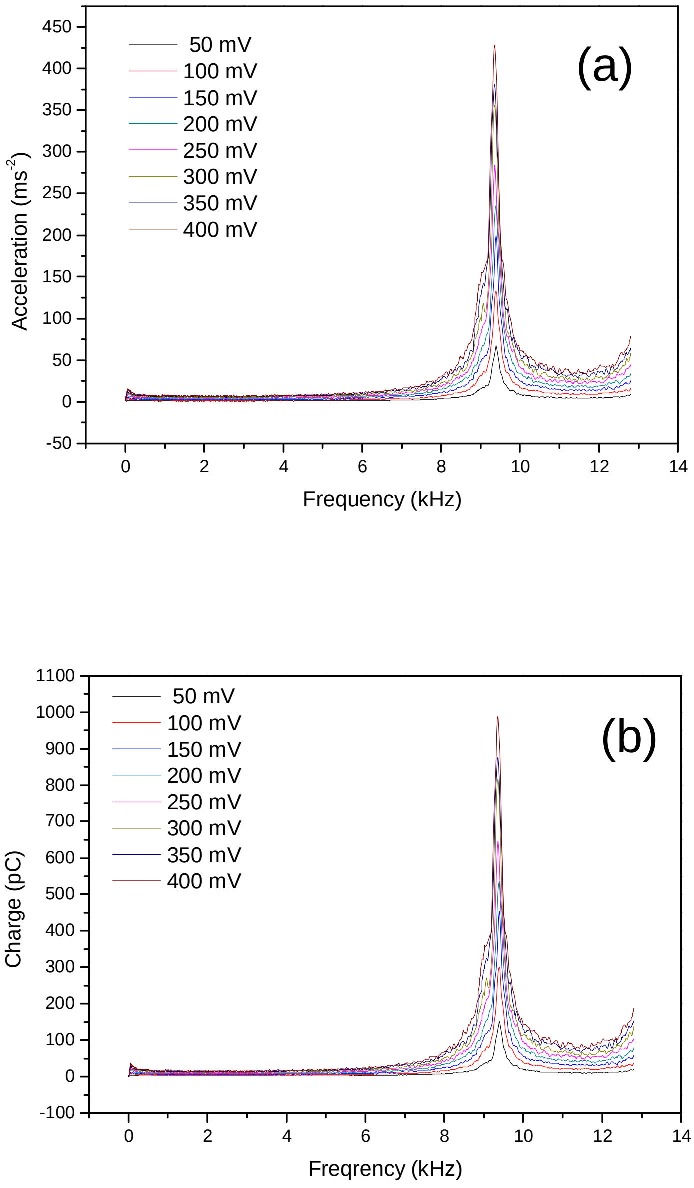

Figure 4.12 The frequency response curves under various vibration amplitudes of (a) type 8305 standard reference accelerometer $a(f) = \dfrac{Q_{ref}(f)}{S_{ref}(f)}$ and (b) prototype accelerometer with BNKBT-5 rings as transduction elements $Q_x(f)$.

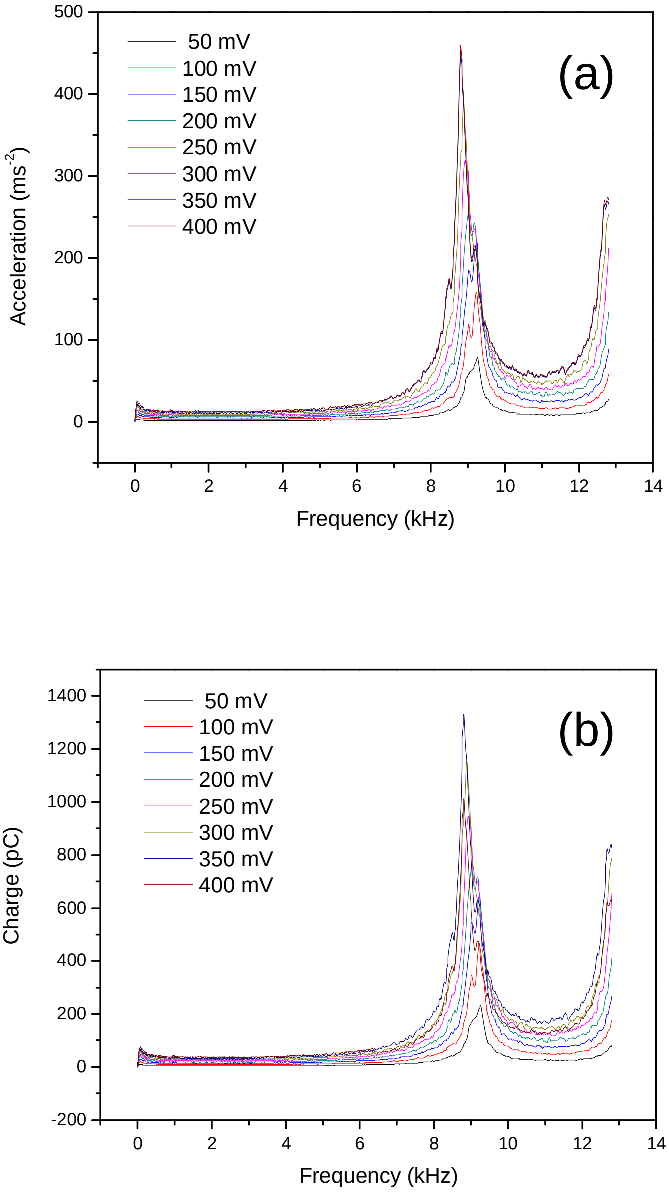

Figure 4.13 The frequency response curves under various vibration amplitudes of (a) type 8305 standard reference accelerometer $a(f)=\dfrac{Q_{ref}(f)}{S_{ref}(f)}$ and (b) prototype accelerometer with BNKLBT-1.5 rings as transduction elements $Q_x(f)$.

From the frequency spectra presented above, a sharp peak can be observed at frequencies between 8-8.5 kHz. The peak is due to the system resonance of the mounted components. The frequency-sensitivity spectrum of the prototype accelerometers is shown in Figure 4.14. The sensitivity of the prototype accelerometers is calculated by the individual charge output spectrum ($S_x = \frac{Q_x(f)}{a(f)}$). Basically, tolerance factor have been set for each devices. For piezoelectric accelerometer, the typical tolerance factor is range from ±2% to ±5%, depends on the manufacturers and the products. Some products will have a higher tolerance factor which is design dependent. In our study, the tolerance factor is standardized in the range of ±2.5% for all prototype accelerometers which are commonly used in commercial devices. The sensitivity curve is linear fitted to obtain the median value. By using the tolerance factor, the upper and lower limit of the acceptable range has been set and the usable frequency range can be found.

In this study, the accelerometer with PZT APC 840 as transduction element has the highest sensitivity of 4.34 pC/ms^{-2}. This is mainly because APC 840 has the highest d_{33} constant over the other lead-free materials. The usable frequency range of APC 840 is the narrowest which is from 50 Hz to 8.24 kHz. The sensitivity and frequency range of BNKBT-5 accelerometer is 2.24 pC/ms^{-2} and 50 Hz - 10.1 kHz, respectively. BNKLBT-1.5 accelerometer has the widest useable frequency range in the prototype accelerometers which is 50 Hz -12.45 kHz and has a sensitivity of 2.97 pC/ms^{-2}. An interesting result has been observed on the sensitivity of BNKBT-5 and BNKLBT-1.5 accelerometer. In the ideal case which mentioned in the previous section, the sensitivity of the piezoelectric sensor is directly related to the piezoelectric d_{33} constant of the transduction material. This phenomenon is seen in the PZT APC 840 accelerometer which has sensitivity higher than both BNKBT-5 and BNKLBT-1.5 accelerometers due to the higher d_{33} value in APC 840. But for BNKBT-5 and BNKLBT-1.5, both of them have a similar d_{33} value (within 5% difference) but their devices have ~20% sensitivity difference. This indicates that other than the major factor, d_{33} constant, other factors can also affect the performance of the accelerometer. Accelerometer is a device sensing the force which generated by acceleration acting on the piezoelectric transduction element. Charges are generated and collected by the M.A.S. in this study. If the energy/charge is not totally transfer to the M.A.S./measuring unit, the resultant sensitivity value will be reduced. As the transduction element is clamped by the base and the seismic mass in the compressive type accelerometer, the vibration energy may transfer to the metal parts and thus cannot be detected by the detector.

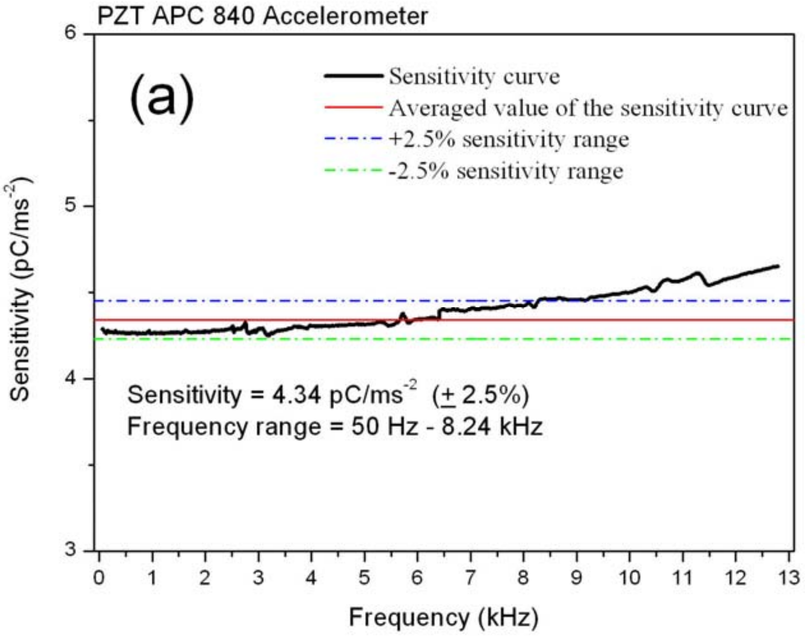
PZT APC 840 Accelerometer
(a)
Sensitivity curve
Averaged value of the sensitivity curve
+2.5% sensitivity range
-2.5% sensitivity range
Sensitivity = 4.34 pC/ms^{-2} (± 2.5%)
Frequency range = 50 Hz - 8.24 kHz
Sensitivity (pC/ms^{-2})
3
4
5
6
Frequency (kHz)
0 1 2 3 4 5 6 7 8 9 10 11 12 13

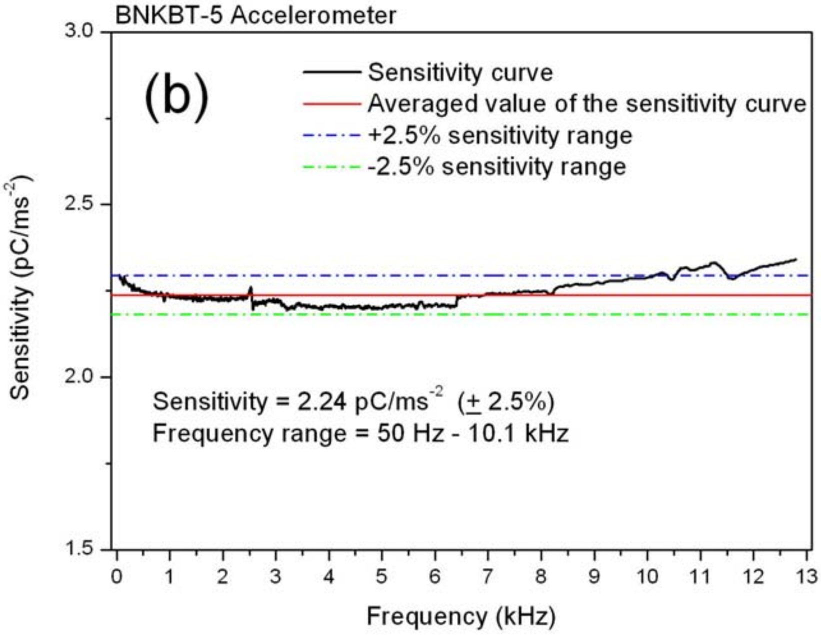
BNKBT-5 Accelerometer
(b)
Sensitivity curve
Averaged value of the sensitivity curve
+2.5% sensitivity range
-2.5% sensitivity range
Sensitivity = 2.24 pC/ms^{-2} (± 2.5%)
Frequency range = 50 Hz - 10.1 kHz
Sensitivity (pC/ms^{-2})
1.5
2.0
2.5
3.0
Frequency (kHz)
0 1 2 3 4 5 6 7 8 9 10 11 12 13

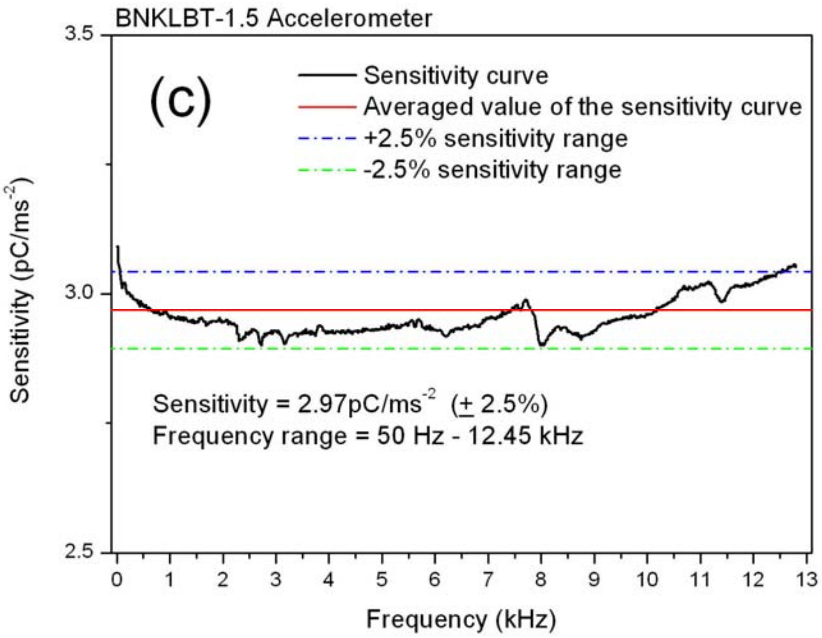

Figure 4.14 The sensitivity curve of prototype accelerometer with different transduction materials: (a) PZT APC 840, (b) BNKBT-5 and (c) BNKLBT-1.5, respectively. The ratio of charge output from prototype accelerometer $Q_x(f)$ to the measured acceleration in reference accelerometer a(f) which is the sensitivity of the prototype accelerometer.

4.6. CONCLUSION

Prototype piezoelectric accelerometers with different transduction elements have been fabricated. The accelerometers have the compressive-type design, with stainless steel seismic mass, base and housing; 1.17mm diameter PTFE insulated coaxial cables with length of ~30 cm, copper electrodes and BNC connectors. The electrical characteristics of the accelerometers have been measured using an impedance analyzer. From the measured results, no resonance peak has been found in the sensing frequency range (<12.8 kHz). The pre-stressing condition can affect performance of the accelerometer and an optimum condition has to be used. The transduction element has been tightened between the seismic mass and the base and different pre-stressing torque has been applied on an UNF 10-32 bolt by a torque driver. A 60 kgf-cm torque has been used as the optimum value. Prototype accelerometers are calibrated by a back-to-back method and the sensitivity of APC 840, BNKBT-5 and BNKLBT-1.5 accelerometers are found to be 4.34 pC/ms^{-2}, 2.24 pC/ms^{-2} and 2.97 pC/ms^{-2}, respectively. The frequency range are 50 Hz – 8.24 kHz, 50 Hz – 10.1 kHz and 50 Hz – 12.45 kHz, respectively.

CHAPTER 5 LEAD-FREE PIEZOELECTRIC DEVICE APPLICATION 2: ULTRASONIC WIREBONDING TRANSDUCER

5.1. INTRODUCTION

In the previous Chapter, we have presented the use of lead-free piezoelectric ceramics in accelerometer application. The principle of a piezoelectric accelerometer is based on the directly piezoelectric effect, which converts pressure/force to charge. In this Chapter, another piezoelectric device, the ultrasonic wirebonding transducer which uses the converse piezoelectric effect is presented.

Ultrasonic wirebonding transducer is a device operated in ultrasonic frequency which converts electrical to mechanical energy. Ultrasonic wirebonding transducer is mainly used in microelectronic packaging in chip level interconnections. In this Chapter, the basic background of the wirebonding technology, ultrasonic wirebonding transducer, fabrication and evaluation of the prototype transducer will be presented.

5.2. BACKGROUND

5.2.1. WIREBONDING TECHNOLOGY

Typical electronic systems are made up of several layers or levels of packaging, and each level of packaging has distinctive types of interconnection devices associated with it. Wirebonding belongs to the first-level interconnection. First-level interconnection (or packaging) refers to the technology required to get electrical signal into and out of a single transistor or integrated circuit (IC), or can be expressed as the connections required between the bonding pads on the IC and the pins of the package. Wirebonding is still the dominant method used in today's first-level interconnection, particularly for chips with moderate number of inputs/outputs, though it is the oldest method. This technique involves connecting gold or aluminium wires, with a diameter of ~1 mil (25μm), between the bonding pads located around the periphery of the chip, and contact points on the package. In the late 1950s, the wirebonding process used thermocompression bonding in which heat and force are used together to produce a solid-phase diffusion bond. Later, the addition of ultrasonic vibration to the wirebonding process made the process significantly more manufacturable and reliable (Ulrich and Brown 2006).

Ultrasonic wirebonding relies on pressing together the two bonding interfaces, namely the wire and the bonding surface on the substrate/frame. The ultrasonic bonding process (Figure 5.1) uses ultrasonic energy to vibrate the wire against the surface to combine the atomic lattices together at the surface. Firstly, the bonding tool, i.e. the wedge or capillary, descends at high velocity and makes transition to contact velocity at the wedge tip. The wire clamps are closed to assure the wire does not move under the tool. Secondly, the first bond is formed by application of bond force and ultrasonic energy. Thirdly, the clamps are opened and the wedge ascends vertically and it moves horizontally to a position over the second bond site. Next, the clamps are closed again and high-speed motions move the wedge downward until it reaches the tip distance above the package then the second bond is formed. The articulated clamps move away from the wedge to break the wire at the back radius tool. The clamps push the wire through the wedge feeding hole to provide the wire for the next bonding cycle.

Localized heating at the bond interface caused by the scrubbing action, aided by the oxide on the aluminium wire assists in forming the bond and prevents the substrate from heating. Intermetallic compound formation is not as critical as another wirebonding process, namely thermocompression bonding process, because both the wire and the device metallization are aluminium. Ultrasonic bonding makes a stitch on both the first and the second bonds. As the capillary must be aligned with the bond site when the first bond is made, the ultrasonic bonding has a lower speed than thermocompression bonding. Ultrasonic bonding to package leads maybe difficult if the leads are not tightly clamped since the ultrasonic energy may propagate down the leads instead of being coupled to the bond site. Figure 5.2 shows a photo of a successful ultrasonic wirebond, which is a typical first bond by wedge bonding, and the IC interconnection using wirebonding technology.

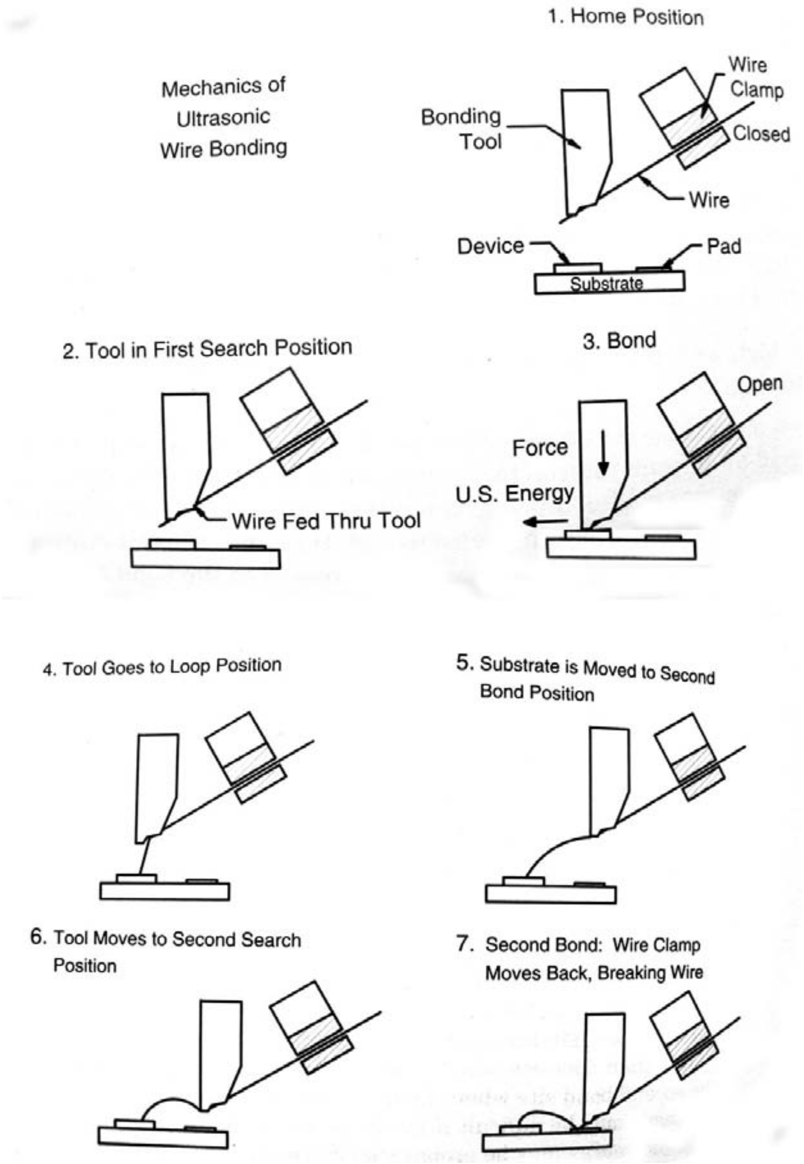

Figure 5.1 The bonding sequence in ultrasonic wirebonding. (Harper 2004)

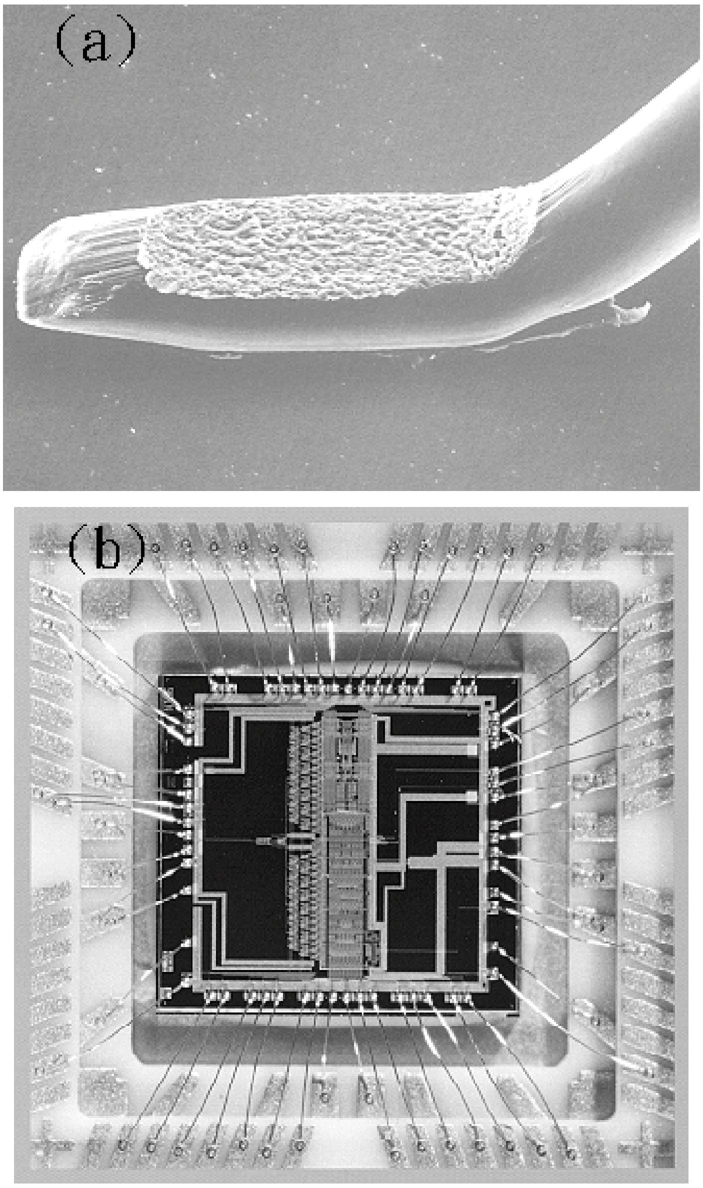

Figure 5.2 Photos of ultrasonic wirebonding. (a) An example of wedge bond, the first bond. (b) IC interconnection using wirebonding technology.

5.2.2. WIREBONDING TRANSDUCER

In ultrasonic wirebonding, the aluminium /gold wires form intermetallic bond with the bond pad using ultrasonic energy. The ultrasonic energy is provided by the ultrasonic wirebonding transducer which is a key component in the bonding process. A state-of-the-art ultrasonic wirebonding transducer which is currently used in wirebonding system is shown in Figure 5.3 (courtesy of ASM Assembly Automation Ltd in Hong Kong). The transducer is operating at 63 kHz and equipped with a wedge for wedge bonding. The transducer can be divided into 3 sections, including a driver, a horn and a wedge. The driver is used to generate the ultrasonic energy during the bonding and it is a Langevin sandwich-type transducer. It is designed to have a half-wave resonance to provide maximum power efficiency (Burgt and Stuijts 1963). It converts electrical energy generated by phase-locked-loop ultrasonic signal generator into longitudinal axial vibration along its length. The driver is formed by 4 piezoelectric rings, connected electrically in parallel and mechanically in series with thin ring electrodes inserted in between, and are sandwiched between front and back metal plates by a central prestressed bolt. The front plate of the driver is screw-topped which can screw-connect with to horn. The horn has an exponential profile which couples and amplifies the axial vibration of the driver to provide a maximum vibration across the horn tip. The amplified vibration is then transmitted via the wedge to the bonding wire, aluminium wire here, and the bond pad surface. The wedge is fixed into a hole drilled at the horn tip by a small screw inserted axially so that it can be replaced for periodic quality assurance.

The electrical properties of the state-of-the-art ultrasonic wirebonding transducer is shown in Figure 5.4 which are frequency spectra of impedance and phase angle. The position of the small circle indicates the operating mode and other resonance modes are also observed. It is important to have a relatively clean operating mode which is not affected by other resonance modes in order to obtain good bonding performance. In bonding point of view, besides axial mode, the existence of other resonance modes may have undesirable effect during bonding; especially those modes with frequencies close to the operating mode. Those resonance modes would be excited during the bonding process and degrade the bonding quality. Therefore, an elimination of unwanted non-axial modes while retaining the axial mode is an important factor in the design of a good wirebonding transducer.

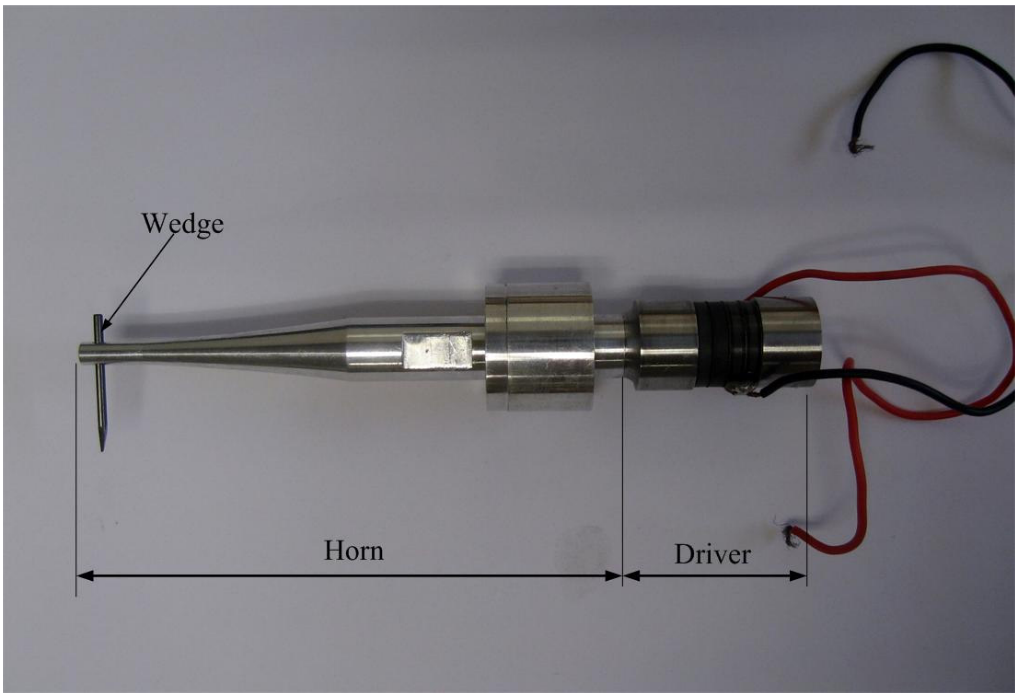

Figure 5.3 Photograph of the state-of-the-art ultrasonic wirebonding transducer with an operating frequency of 63 kHz and equipped with a wedge.

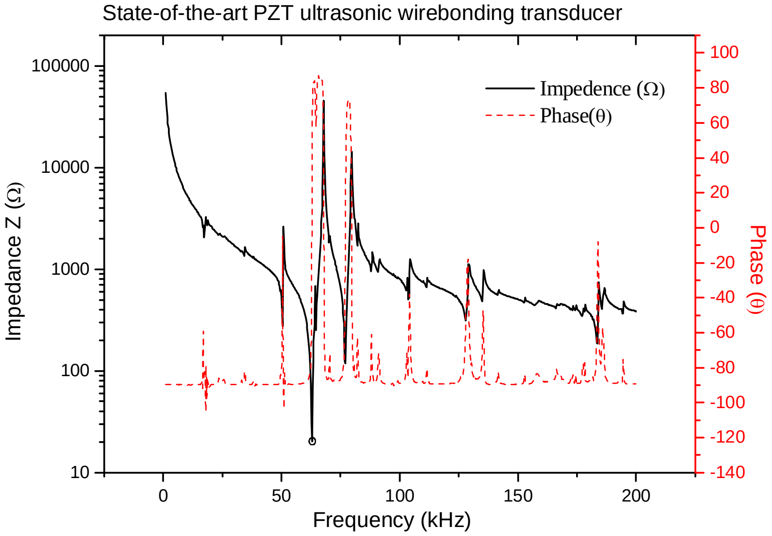

Figure 5.4 Impedance and phase frequency spectra of the wirebonding transducer (shown in Figure 5.3) operated at 63 kHz.

5.3. PROTOTYPE ULTRASONIC WIREBONDING TRANSDUCER

In this study, ultrasonic wirebonding transducers will be fabricated using different materials as the driving element in the ultrasonic driver. All the metallic transducer components are supplied by ASM Assembly Automation Ltd in Hong Kong. In this Section, the results of the prototype ultrasonic wirebonding transducers are presented, including the computational analysis, fabrication procedure, electrical properties and the mechanical properties. Those properties will be compared with the state-of-the-art ultrasonic wirebonding transducer. The prototype wirebonding transducer used the same design as the state-of-the-art transducer; the explosive diagram and the assembled diagram of the transducer are shown in Figure 5.5.

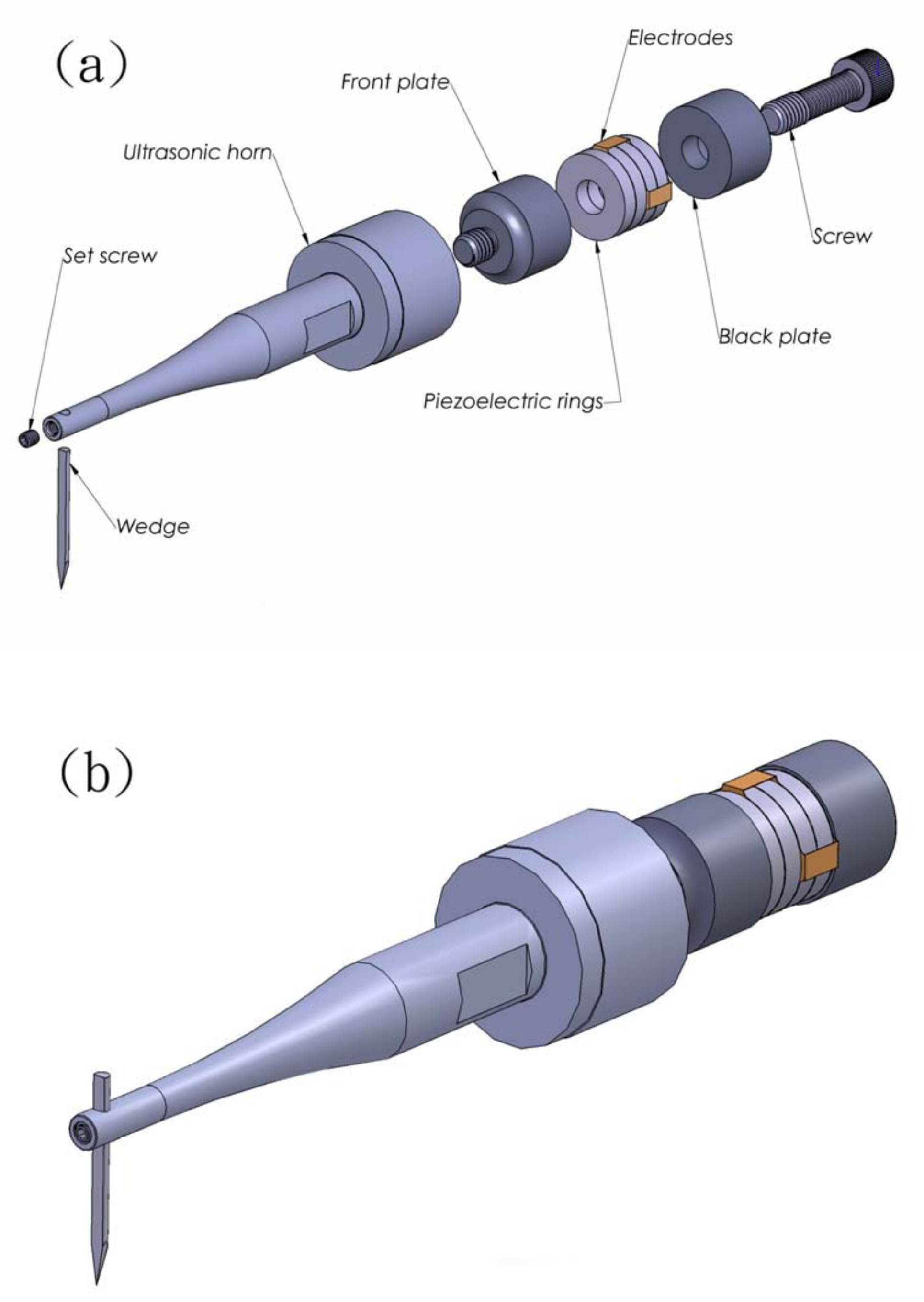

Figure 5.5 The prototype ultrasonic wirebonding transducer: (a) explosive diagram and (b) assembled diagram.

The transducer performance is mainly affected by the driving element, the piezoelectric rings, including the operating frequency, electrical and mechanical properties. It is essential to predict the performance of the transducer before fabrication. With improved computational technique and based on our previous experience, using computational simulation with appropriate models can effectively predict the performance of the final product. Finite element method is a commonly used computation analysis method. In the subsequence Section, the detail of the computational analysis on the prototype wirebonding transducer is given.

5.4. COMPUTATIONAL ANALYSIS USING FINITE ELEMENT METHOD

Finite element method (FEM) is a sophisticated numerical simulation method which aims at solving complex partial differential equations so as to mathematically describe, or predict, the physical behavior of an actual engineering structure by constructing the structure as a virtual object or model in a computer (Cook 1995). All finite element methods involve dividing the physical systems, such as structures, solid or fluid continuum, into small subregions or elements. Each element is a simple unit, the behavior of which can be readily analyzed. The complexities of the overall systems are accommodated by using large numbers of elements to obtain the numerical solution.

As the state-of-the-art wirebonding transducer is designed to operate at 63 kHz, the prototype transducers are designed to operate in the same frequency range. By using the FEM, the vibration profile of the transducers at different resonance modes, both axial mode and flexural mode, can be simulated and visualized. In this work, four different prototype transducers are modeled. The detail of the transducers is summarized in Table 5.1.

Table 5.1 Summary of the dimensions and materials used in the prototype ultrasonic wirebonding transducers.

	Driving material	Dimension of front plate (mm)	Dimension of back plate (mm)	Material of front and back plates
Transducer A	PZT APC 840	8	8	Stainless Steel (S.S.)
Transducer B	BNKBT-5	8	8	Stainless Steel (S.S.)
Transducer C	BNKLBT-1.5	8	8	Stainless Steel (S.S.)
Transducer D	BNKLBT-1.5	10	10	Titanium (Ti)

The transducer described in the previous Section (Figure 5.5) with axial-symmetry about their central (z) axes can be modelled as a 360^o sector of elements with symmetry boundary conditions applied about the z axes. A schematic diagram of a 360^o finite element model of the wirebonding transducer is shown in Figure 5.6 which is a common model for all transducers as all of them have a similar structure. All possible excited resonance modes, including both axial and flexural modes, can be found simultaneously by using the full model. All the material properties are equal to that presented in the previous Chapter (Table 3.4) but the loss factors have been ignored. Linear and anisotropic properties are assumed for the elements piezoelectric materials and the metal parts are assumed to be linear and isotropic.

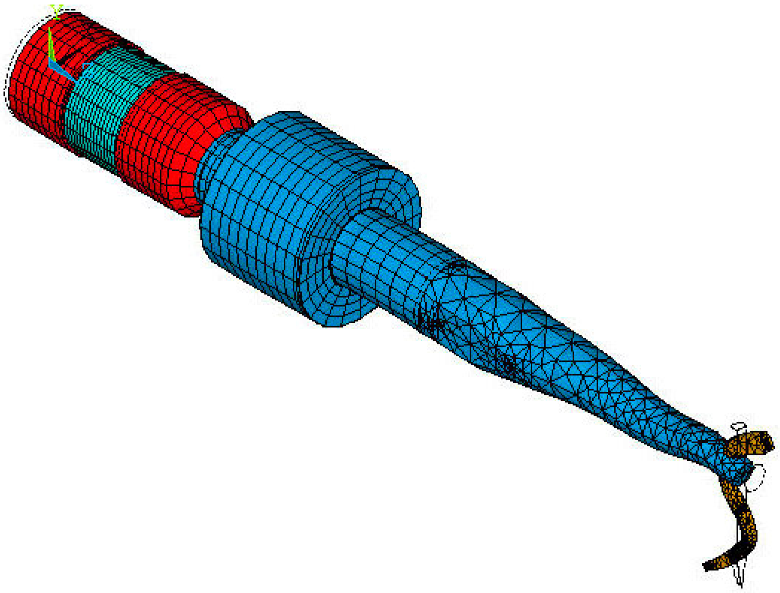

Figure 5.6 Finite element model of the 63 kHz wirebonding transducer shown in Figure 5.5.

To simplify the model, some amendments have been made between the real product and the model. Firstly, the screw for prestressing is ignored and so are the thread and threaded bore on the front plate. The ring shaped copper electrodes (~0.05mm each) are assumed to be very thin and will not be taken into account. All components in the assembly are assumed to have perfect mechanical coupling with each other. A suitable model is required for FEM. Based on the h-type approach suggested by J. R. Frederick (Frederick 1965), a good result, which is approximate to the exact numerical solution, can be simulated by increasing the number of solid elements and the number of nodes in the FEM. But the requirement is the mesh of the solid element is sufficiently dense for describing all mode shape of interest. A well-designed mesh in the model can provide a high refinement in the solution. A 3D coupled-field solid element SOLID5 and 3D structural solid element SOLID45 (Figure 5.6) are used for piezoelectric rings and the metal component, respectively.

Commercial FEM software, ANSYS® version 9, has been used to simulate the result in our study. ANSYS® provides a structural analysis technique, namely modal analysis, which aims at determining the natural frequencies and mode shapes of a resonance structure. The analysis ascertains the linear response of the structure with the exclusion of any nonlinearity.

The effective resonance modes of the prototype transducers within 50-70 kHz are summarized in Table 5.2. Some of the computed mode are found to be excluded by the electrical boundary conditions and are not observed in the impedance spectrum. The mode shape can be categorized as axial, torsional, flexural and complex modes. The computed axial operating frequency of the prototype transducers is around 63-65 kHz, which have a good agreement with the experimental result and the result will be presented in the subsequent Section. Basically, transducer produces a piston-like motion in its axial direction due to the pure axial vibration excitation. The axial vibration coupled with the horn and wedge to generate a large axial displacement with forward and backward motion. As this motion is essentially in line with the wire to be bonded, hence the axial mode is the most desirable resonance mode. In practice, all the mode will be excited simultaneously which would generate some undesirable motion that cannot be ignored. The lateral flexural motions from side to side and the torsional motion would affect the bonding quality thus purify the axial motion can reduce the loss of input energy and improve the bonding condition.

Table 5.2 Computed effective modes of prototype transducers.

	Resonance frequency (kHz)	Mode shape
APC 840 transducer with S.S. plates (Transducer A)	53.583	1λ Axial mode
	57.567	Flexural mode
	62.973	Torsional mode
	63.888	1.5 λ Axial mode
	70.653	Complex flexural mode
BNKBT-5 transducer with S.S. plates (Transducer B)	54.194	1λ Axial mode
	59.085	Flexural mode
	62.888	Torsional mode
	64.976	1.5λ Axial mode
	69.719	Complex flexural mode
BNKLBT-1.5 transducer with S.S. plates (Transducer C)	54.595	1λ Axial mode
	59.476	Flexural mode
	65.877	Torsional mode
	67.706	1.5λ Axial mode
	69.867	Complex flexural mode
BNKLBT-1.5 transducer with Ti plates (Transducer D)	53.774	1λ Axial mode
	58.387	Flexural mode
	65.473	1.5λ Axial mode
	67.152	Complex flexural mode
	67.967	Torsional mode

（a） 57. 567 kHz

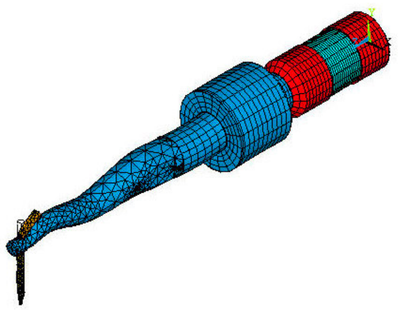

（b） 62. 973 kHz

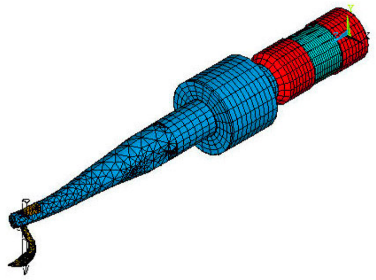

（c） 63. 888 kHz

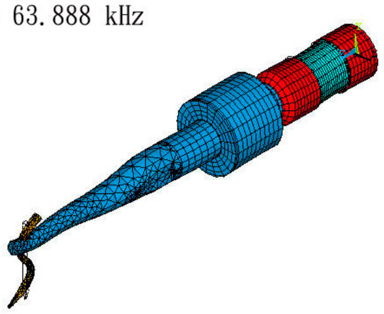

（d） 70. 653 kHz

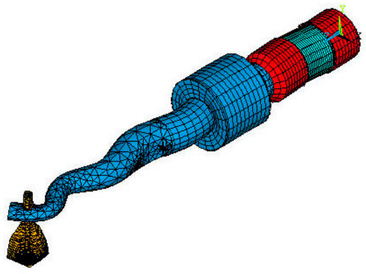

Figure 5.7 Deformed shapes of various natural modes in the APC 840 transducer with S.S. plates. The frequencies are (a) 57.567 kHz, (b) 62.973 kHz, (c) 63.888 kHz and (d) 70.653 kHz.

(a) 59.085 kHz

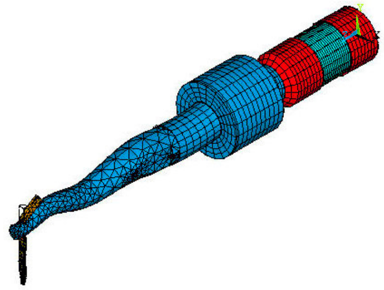

(b) 62.888 kHz

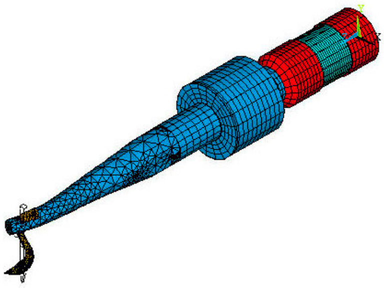

(c) 64.976 kHz

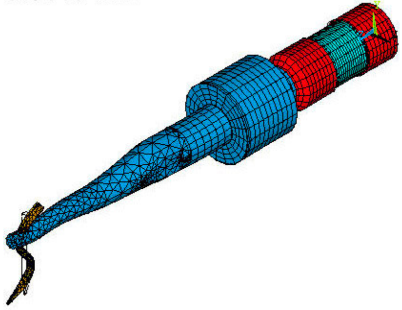

(d) 69.719 kHz

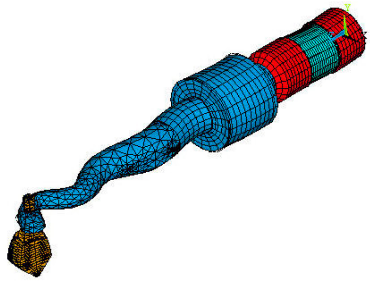

Figure 5.8 Deformed shapes of various natural modes in the BNKBT-5 transducer with S.S. plates. The frequencies are (a) 59.085 kHz, (b) 62.888 kHz, (c) 64.976 kHz and (d) 69.719 kHz.

(a) 59.476 kHz

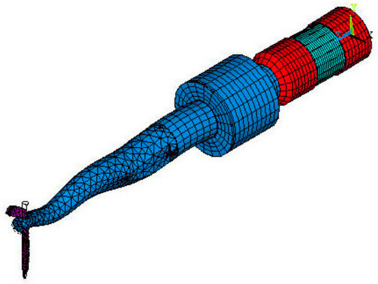

(b) 65.877 kHz

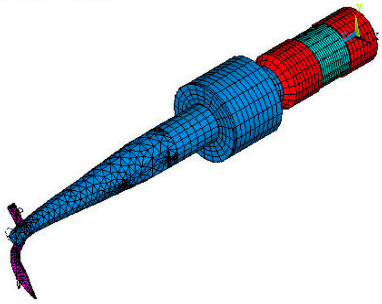

(c) 67.706 kHz

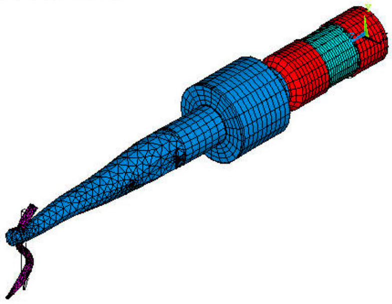

(d) 69.867 kHz

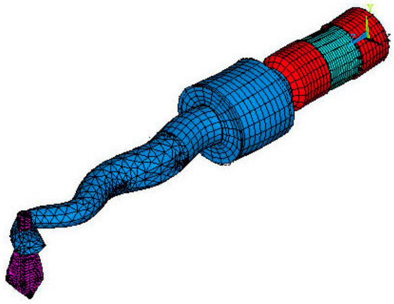

Figure 5.9 Deformed shapes of various natural modes in the BNKLBT-1.5 transducer with S.S. plates. The frequencies are (a) 59.085 kHz, (b) 62.888 kHz, (c) 64.976 kHz and (d) 69.719 kHz.

(a) 58. 387 kHz

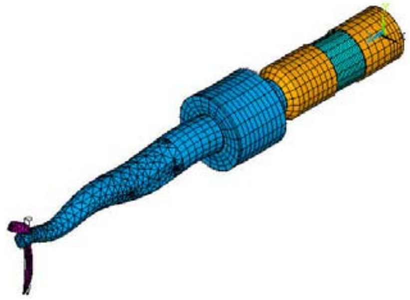

(b) 65. 473 kHz

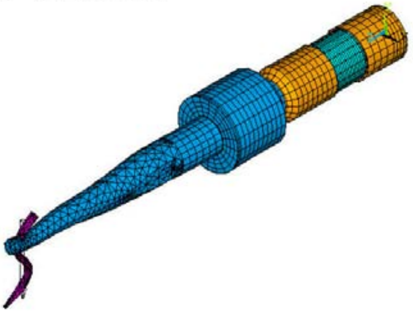

(c) 67. 706 kHz

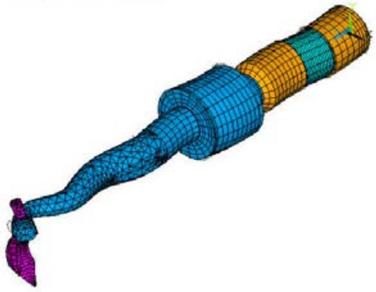

(d) 67. 967 kHz

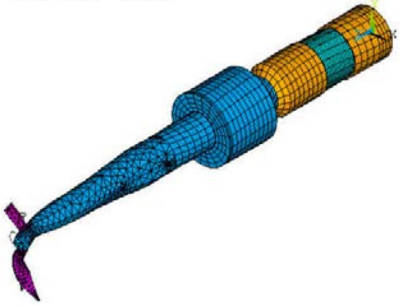

Figure 5.10 Deformed shapes of various natural modes in the BNKLBT-1.5 transducer with Ti plates. The frequencies are (a) 58.387 kHz, (b) 65473 kHz, (c) 67.706 kHz and (d) 67.967 kHz.

Different mode shapes of the corresponding prototype transducers are shown in Figures 5.7 to 5.10. The torsional mode (Figures 5.7(b), 5.8(b), 5.9(b) and 5.10(d)) is mainly due to the lateral vibration of the transducer generated by the driving elements. The separation between the operating mode (axial mode) and torsional mode is much closer in Transducer A (APC 840) than that in lead-free transducers. This indicates that the axial vibration of Transducer A will be affected by the lateral vibration more easily.

5.5. FABRICATION OF PROTOTYPE ULTRASONIC WIREBONDING TRANSDUCER

Fabrication technology, based on the intrinsic material properties and design, is a key factor affecting the performance of a practical transducer. It is essential to have a good mechanical and electrical contact between various parts in the ultrasonic wirebonding transducer since the whole transducer will vibrate under the driving frequency. In this Section, fabrication of the transducer is described before the electrical and vibrational characteristics are reported and compared with the state-of-the-art transducer.

5.5.1. PREPARATION OF TRANSDUCER COMPONENTS

The components used to fabricate the prototype transducers are described as follows:

(a) Piezoelectric Rings

APC 840 rings are supplied by American Piezo Ceramics Inc. Both BNKBT-5 and BNKLBT-1.5 ceramics rings are fabricated using the procedures mentioned in the previous Chapter 3. The ceramic rings have outer diameter of 12.7 mm, inner diameter of 5.1 mm and are 2.3mm thick.

(b) Metal plates, Screw, Ultrasonic Horn and Wedge

Two different metals were used as the front and back plates of the driver, which are stainless steel and titanium alloy. The horn of the transducer used aluminium alloy as the raw material. A mild steelbolt, with insulated tube covering its screw to prevent the direct contact between electrodes and the bolt to avoid short-circuiting, is used to prestress the driver. The wedge of the transducer is made of tungsten carbide which is fixed in the front of the horn and set by a screw.

(c)Ring-shaped Electrodes

Ring-shaped copper electrodes (99.9% oxygen-free) with an outer diameter of 12.7 mm, an inner diameter of 5.0 mm, and a rectangular extended part of 2.5 × 1 mm^2, thickness of 0.05 mm were used. The extended position provides a suitable location for soldering electrical wires.

(d) Electrical Wires

The electrical wires have 0.4 mm diameter covered with 0.4 mm wall-thickness insulating silicone rubber have been used. The wire has good electrical conductivity and mechanical bending ability. In addition, the silicone rubber is colour-coded with red representing the positive and black representing the ground terminal.

5.5.2. ESSENTIALS OF FABRICATION

The prototype transducers were fabricated by assembling different components in an appropriate order as shown in Figure 5.5. A red electrical wire was soldered onto the two central ring-shaped electrodes to indicate the positive terminal while a black one was attached to either of the outermost ones to represent the ground terminal. Next, the polarity of piezoelectric rings was arranged in reversed direction from one ring to the other, and the rings were connected electrically in parallel and mechanically in series to give higher displacement and lower impedance. Afterward, a compressive pre-stress was applied axially onto the piezoelectric rings using a torque driver (Kanon – 100 LTDK). The tightening process stopped automatically as long as the predetermined torque level preset at the torque driver was reach. Both front and back plates had good surface finishing and parallelity. This can improve quality of the pre-stressing in driver.

As the pre-stressing condition affects the transducer performance, too high a pre-tress can cause depolarization or even breakage of the piezoelectric materials, but too low a pre-stress can reduce transducer efficiency as this will increase the losses at various contacting interfaces which impedes the transducer components from behaving as an integrated resonator. A pre-stressing test was performed and the result is shown in Figure 5.11. According to the result, a 63 kgf-cm pre-stress gives the lowest impedance, which is close to the recommended pre-stress level of around 60-65 kgf-cm. Hence, 63 kgf-cm torque was used in the fabrication process.

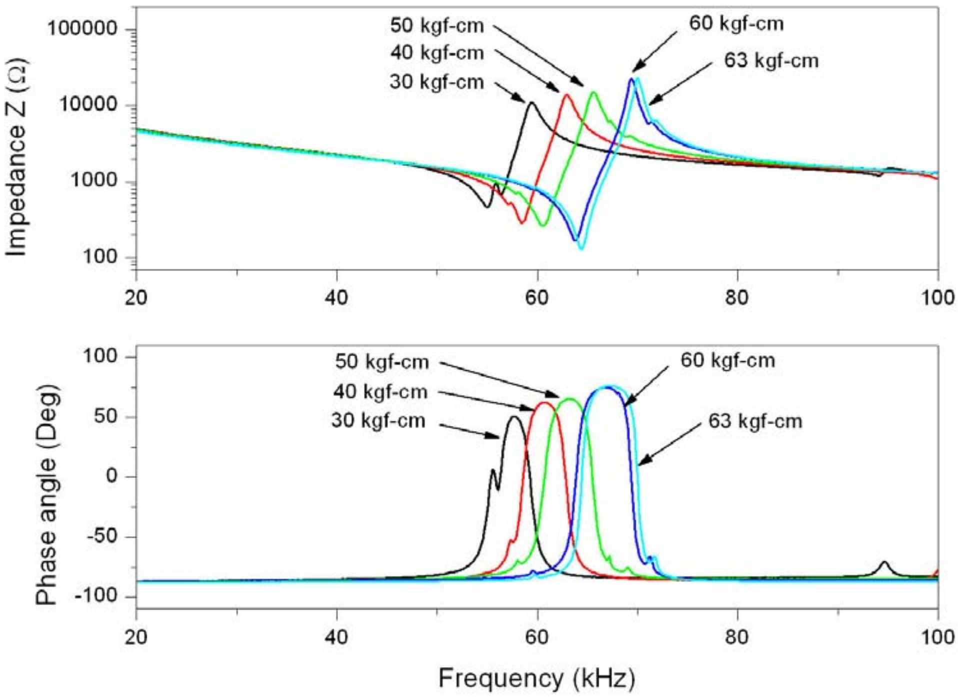

Figure 5.11 The impedance/phase angle frequency spectra of the ultrasonic driver under different pre-stress conditions.

The horn was then installed onto the driver by a torque driver (Tohnichi 60CL with SH8DX8 head) using a 55kgf-cm torque. The wedge was installed in the front of the horn and fixed by a screw.

5.6. PROTOTYPE ULTRASONIC WIREBONDING TRANSDUCER EVALUATION

5.6.1. ELECTRICAL RESONANCE CHARACTERISTICS MEASUREMENT

The electrical resonance characteristics of the prototype ultrasonic wirebonding transducer were evaluated by measuring their electrical impedance and phase spectra using an HP4294A impedance analyzer. Firstly, the electrical properties of each prototype transducer drivers were measured before installing the horn. Figures 5.12, 5.13, 5.14 and 5.15 are the results of the APC 840 driver with S.S. plates (Driver A), BNKBT-5 driver with S.S. plates (Driver B), BNKLBT-1.5 driver with S.S. plates (Driver C) and BNKLBT-1.5 driver (Driver D) with Ti plates, respectively.

The electrical impedance and phase spectra of the prototype ultrasonic wirebonding transducers equipped with horn and wedge are shown in Figures 5.16, 5.17, 5.18 and 5.19 which represent Transducer A, B, C and D, respectively, and comparing with the state-of-the-art PZT transducer. The result of the state-of-the-art transducer is shown in Figure 5.20. Figure 5.21 shows the photographs of the prototype transducers.

In the frequency spectra from 1 kHz to 800 kHz, the strongest resonance mode of all the prototype transducers is at ~64 kHz, which is the operating mode (1.5 λ axial mode) of the transducer. The results are close to the simulation result from FEM. But some spurious resonance modes can be observed close to the working axial mode, which may affect the bonding quality. All transducers with lead-free materials as driving element have weaker and less spurious mode than the PZT transducer, which may improve the bonding quality.

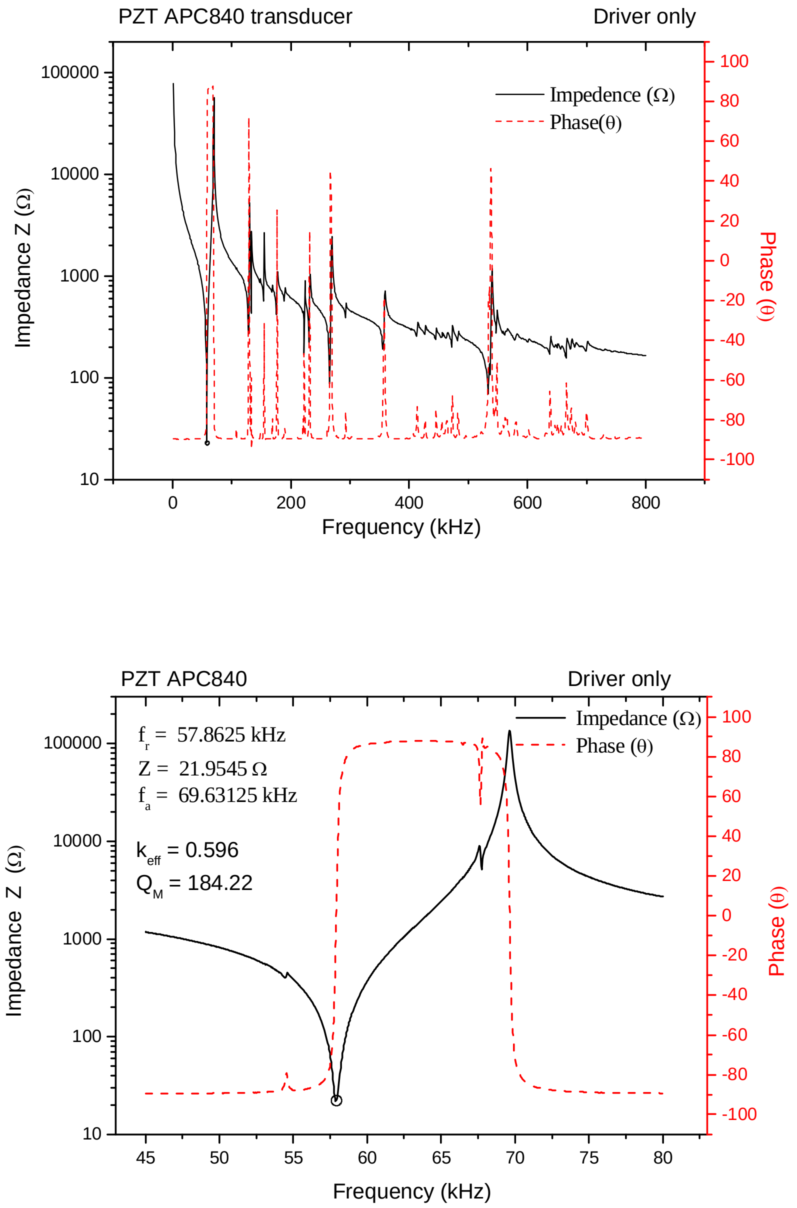

Figure 5.12 Plots of electrical impedance and phase angle versus frequency for the APC 840 ceramics driver with S.S. front and back plates.

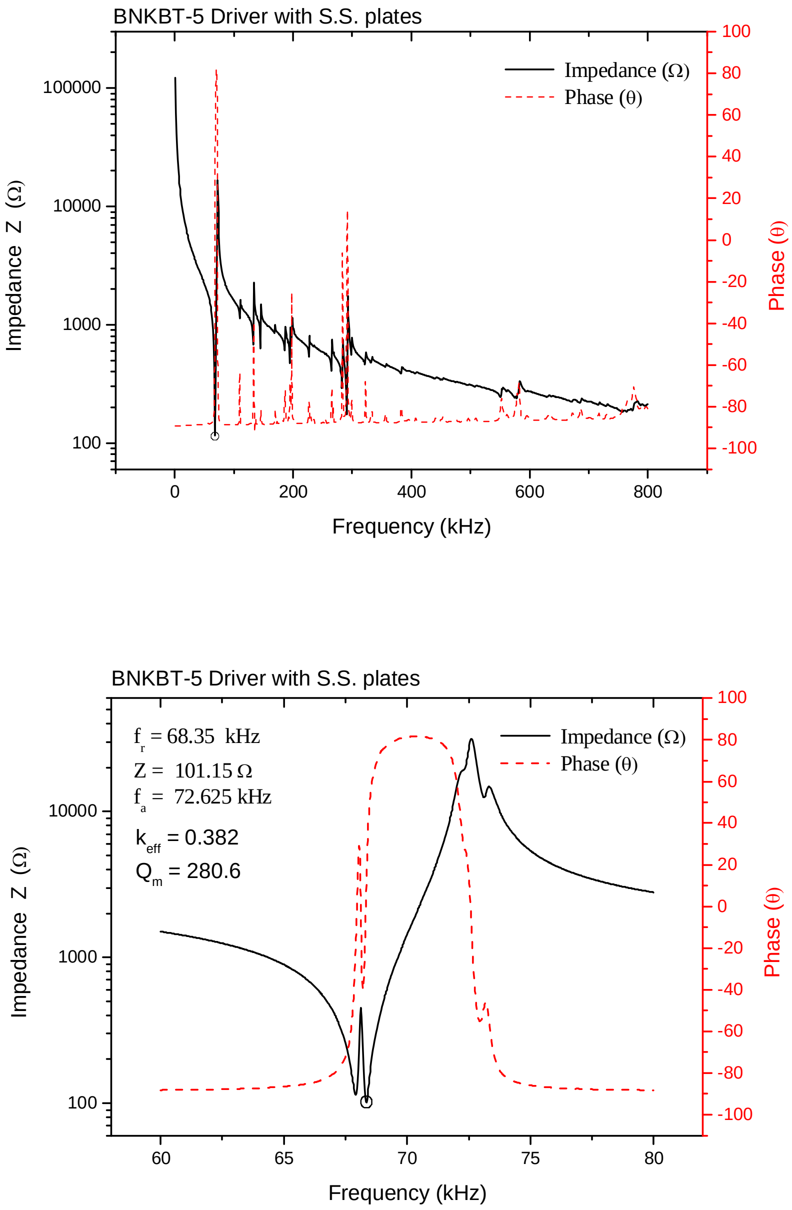

Figure 5.13 Plots of electrical impedance and phase angle versus frequency for the BNKBT-5 ceramics driver with S.S. front and back plates.

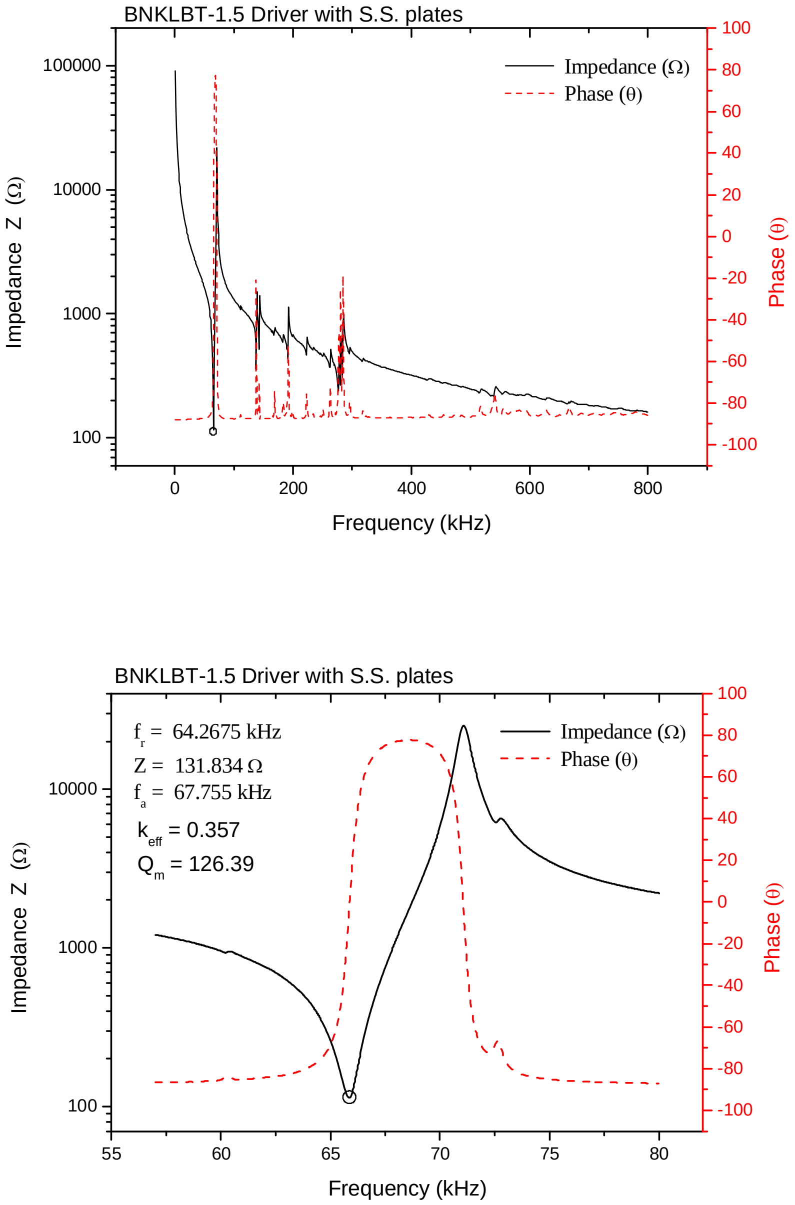

Figure 5.14 Plots of electrical impedance and phase angle versus frequency for the BNKLBT-1.5 ceramics driver with S.S. front and back plates.

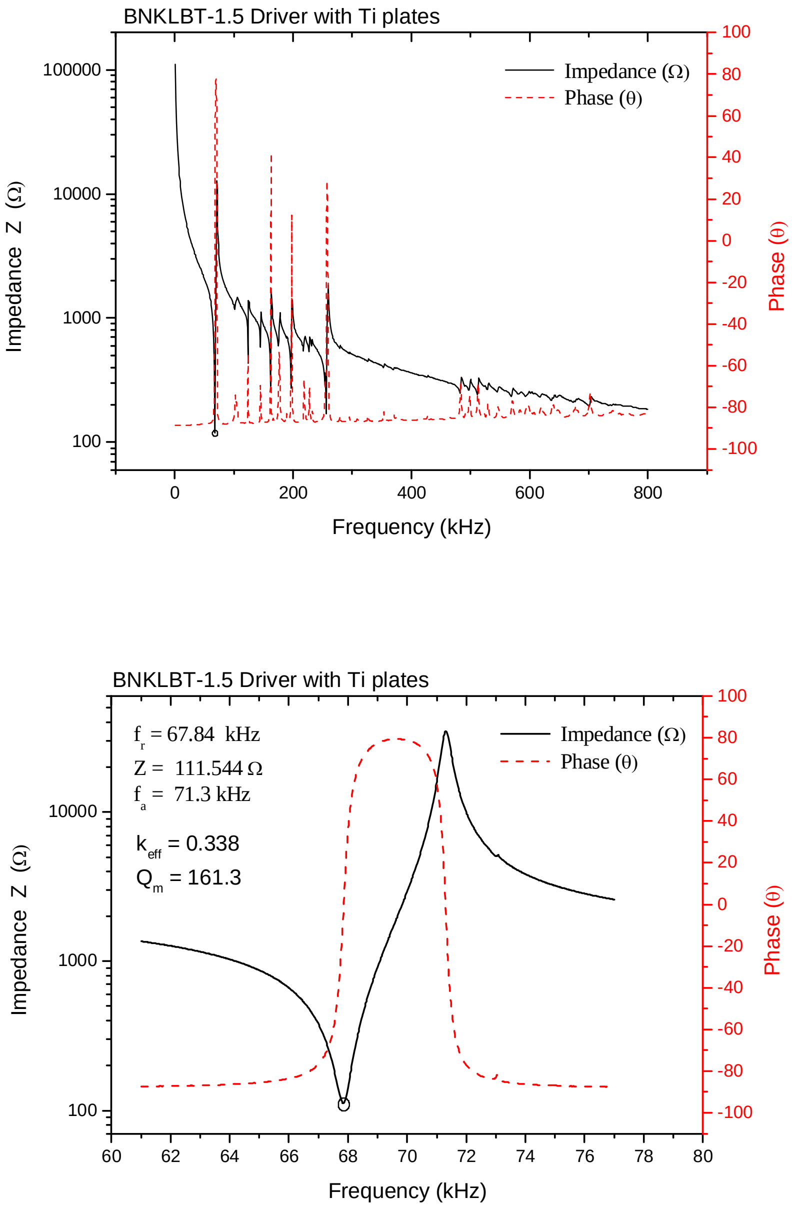

Figure 5.15 Plots of electrical impedance and phase angle versus frequency for the BNKLBT-1.5 ceramics driver with Ti front and back plates.

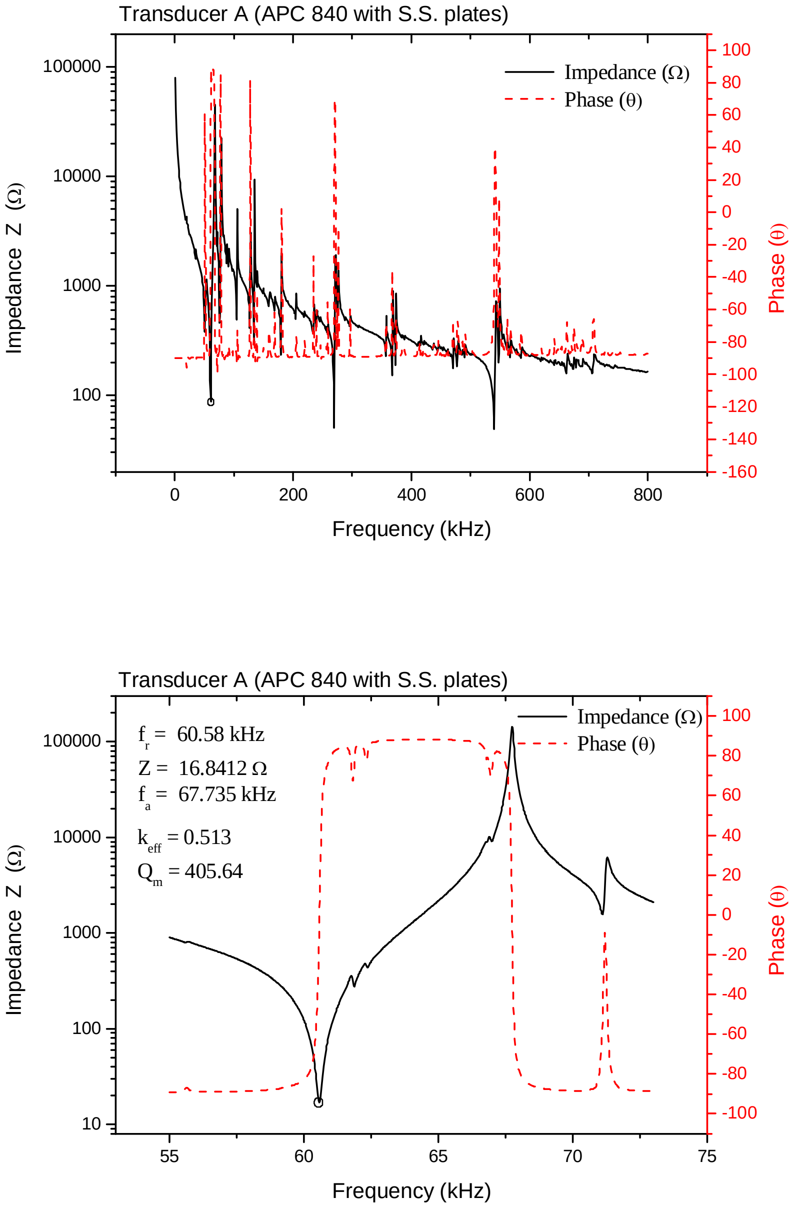

Figure 5.16 Plots of electrical impedance and phase angle versus frequency for the prototype transducer A.

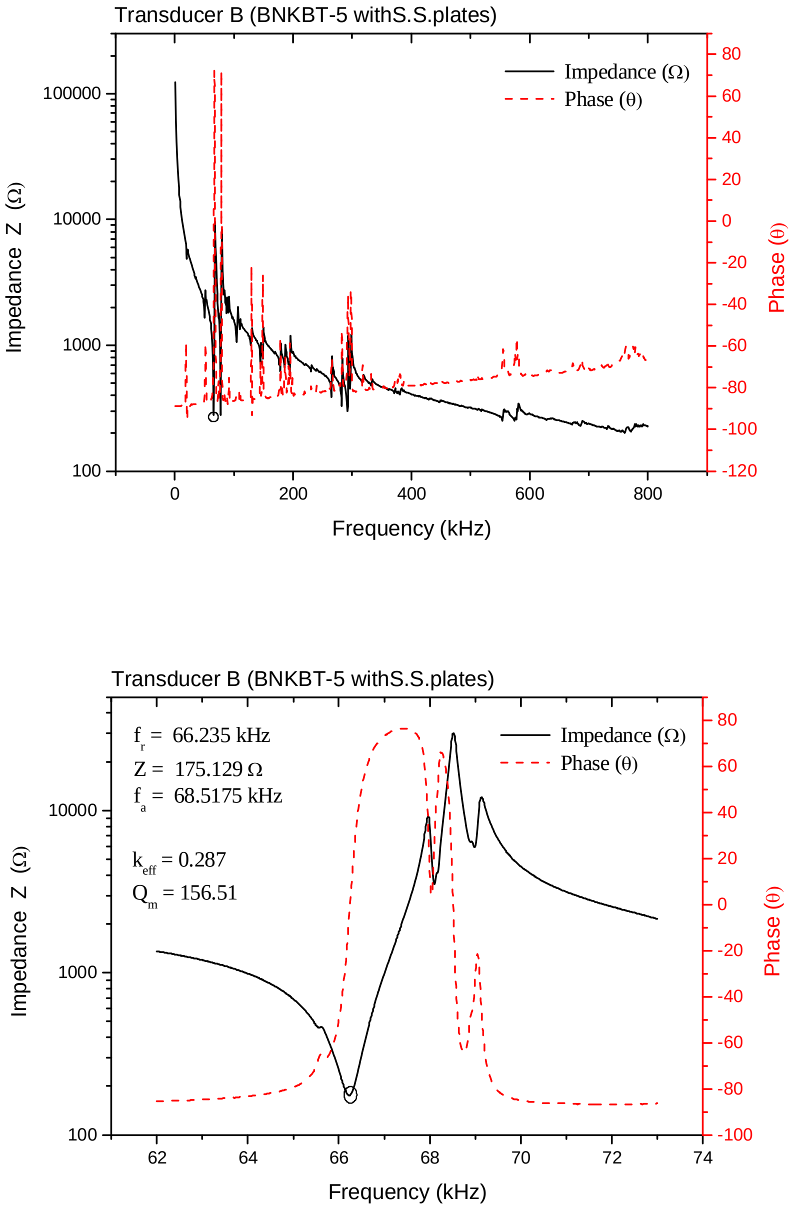

Figure 5.17 Plots of electrical impedance and phase angle versus frequency for the prototype transducer B.

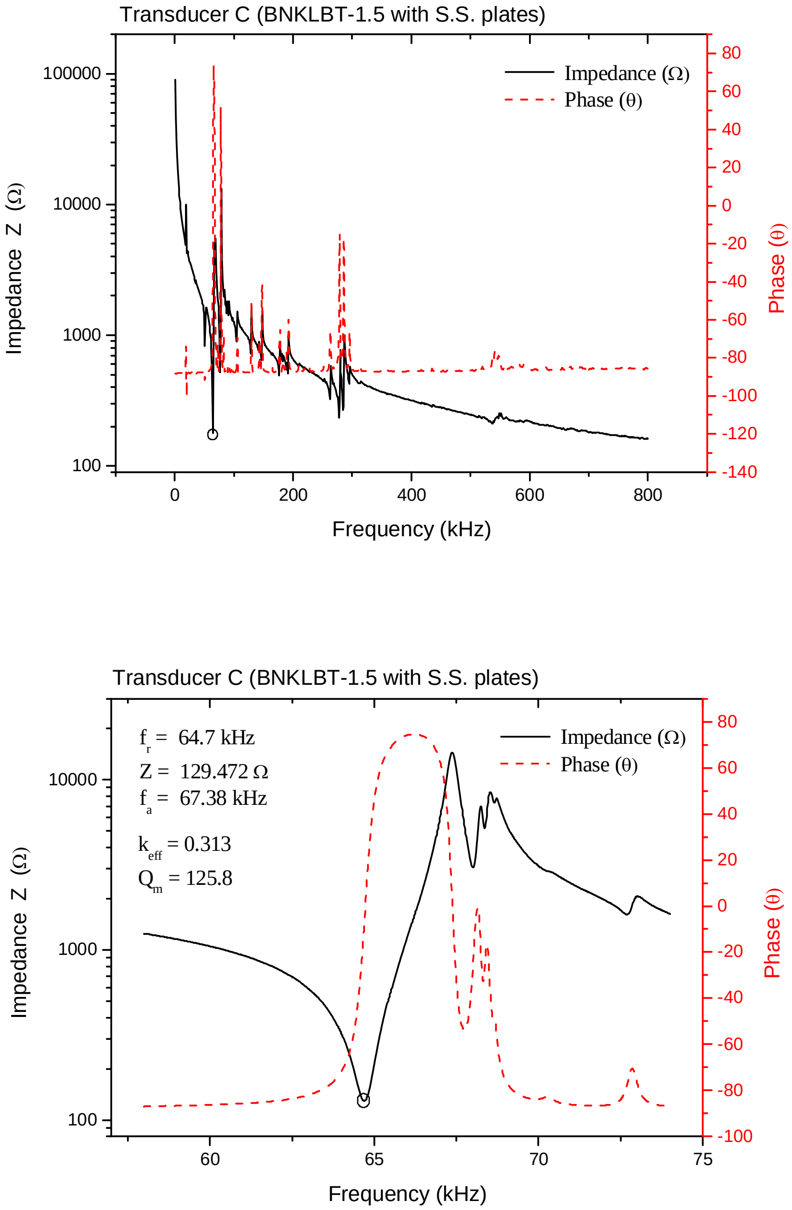

Figure 5.18 Plots of electrical impedance and phase angle versus frequency for the prototype transducer C.

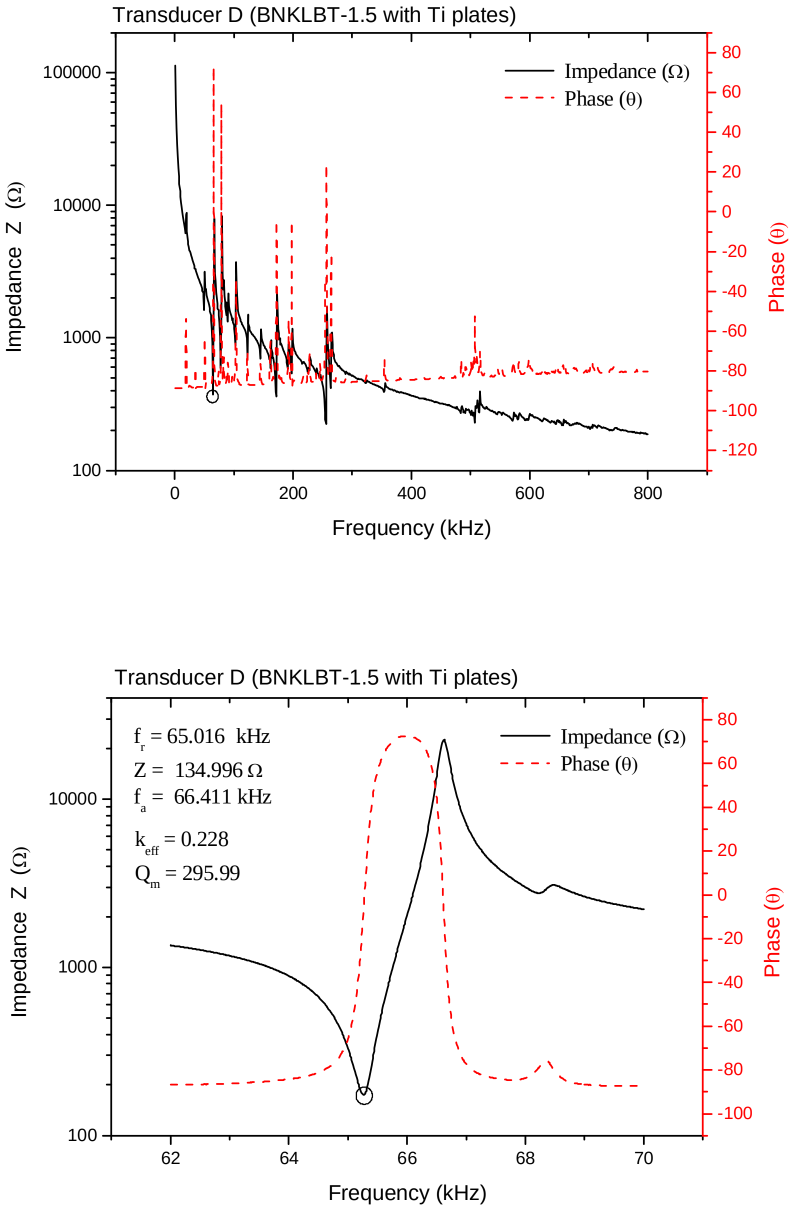

Figure 5.19 Plots of electrical impedance and phase angle versus frequency for the prototype transducer D.

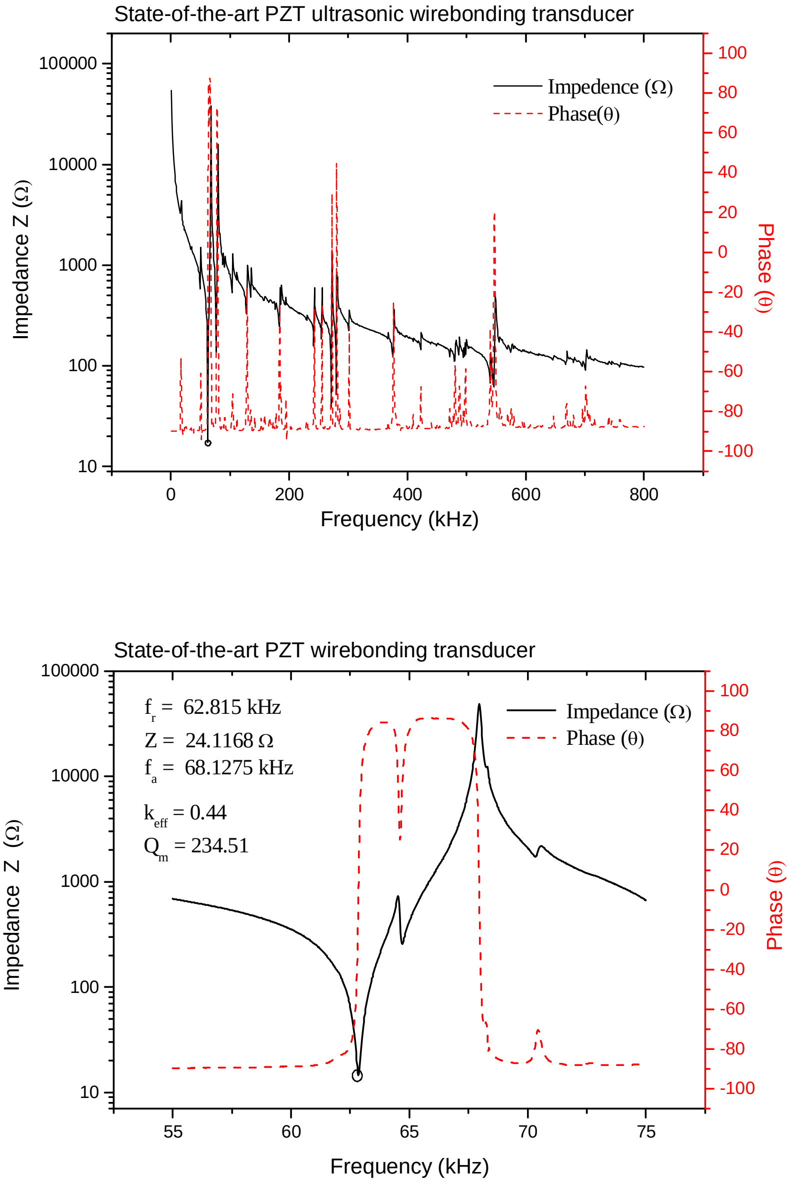

Figure 5.20 Plots of electrical impedance and phase angle versus frequency for the state-of-the-art PZT ultrasonic wirebonding transducer.

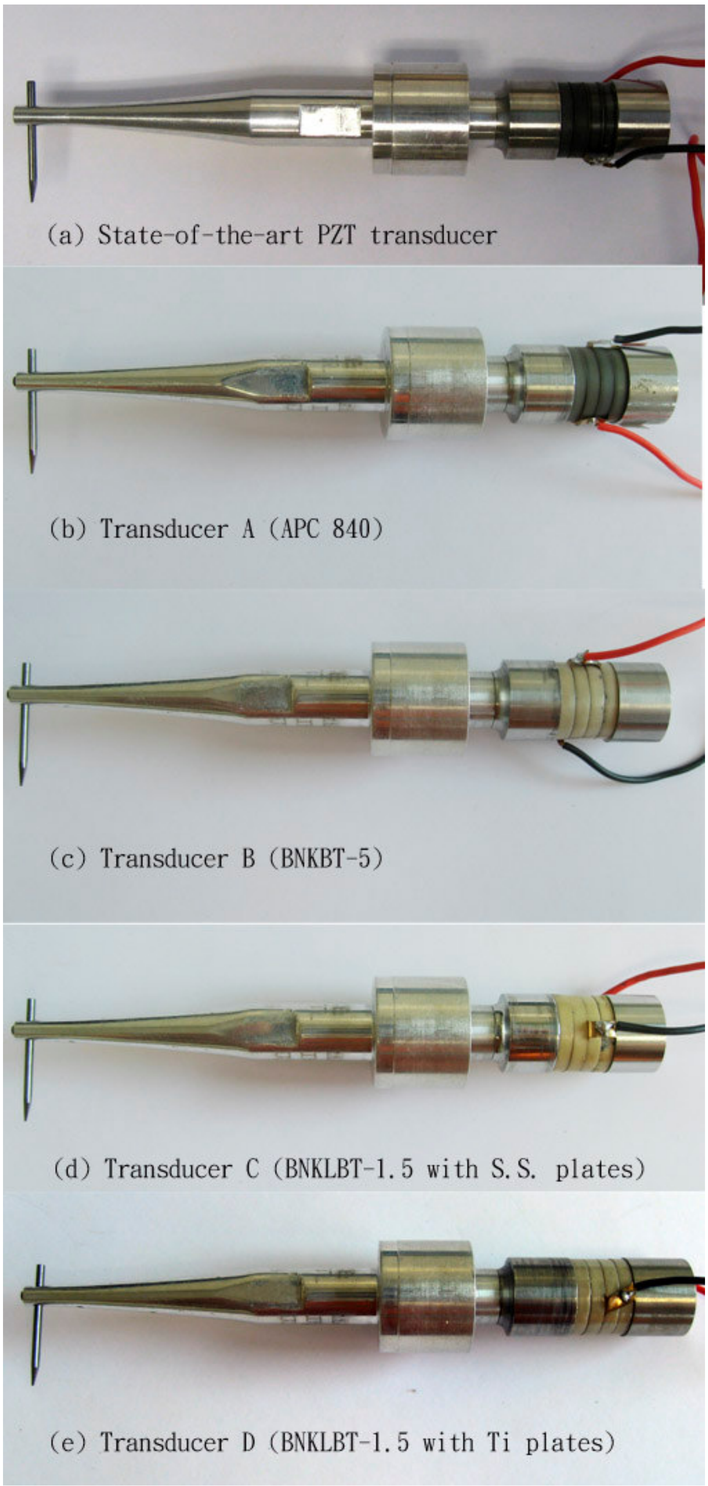

Figure 5.21 Photographs of ultrasonic wirebonding transducers. (a) State-of-the-art PZT transducer, (b) Prototype Transducer A, (c) Prototype Transducer B, (d) Prototype Transducer C and (e) Prototype Transducer D, respectively.

5.6.2. VIBRATION AMPLITUDE MEASUREMENT

5.6.2.1. Experimental Setup

A Polytec laser doppler vibrometer (OFV-303 and OFV-3001 controller processor) was used to characterize the vibration performance of the prototype transducers. OFV-303 Doppler vibrometer based on the principle of Mach-Zehnder type heterodyne interferometer. OFV-303 involves interfering a frequency-shifted (40 MHz) reference laser beam with phase-modulated signal laser beam that contains the vibration information of the transducer (Polytec 1995). The advantages of this state-of-the-art technique are providing a contactless and quantitative measurement without the influence of low frequency ambient vibration. The prototype transducer is fixed on a mounting bracket similar to the clamping condition in the wire bonder. The bracket was placed on an X-Y table with movement in the x and y direction. The schematic diagram of the measurement setup is shown in Figure 5.22.

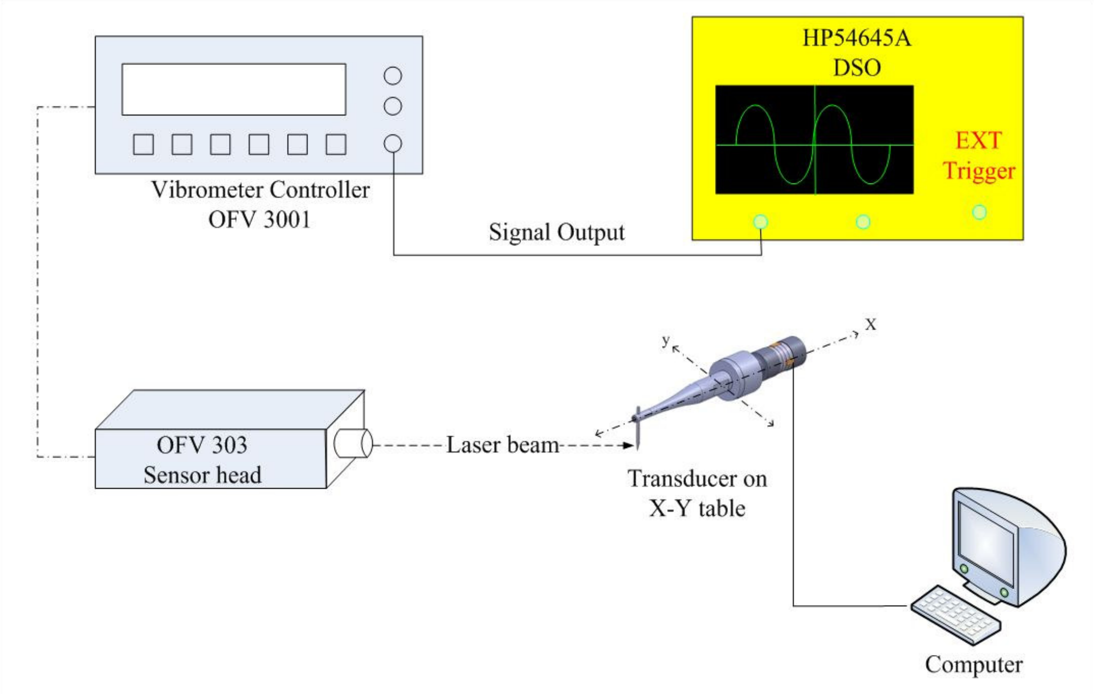

Figure 5.22 Schematic diagram of the measurement of the vibration amplitude.

A computer equipped with a controller board with controlling software was used as an ultrasonic generator to drive the transducer with a constant output power. This board can deliver a constant voltage and has a digital phase-locked-loop (PLL), which will maintain the transducer at resonance during measurement by automatically tuning its output signal frequency to satisfy the preset resonance criteria. The transducer under test was placed at ~50 cm from the laser interferometer. The vibrometer controller (OFV3001) collected the vibration information and then transferred them to an HP 54645 oscilloscope. After being calibrated by the appropriate sensitivity (in V/ms^{-1}) of the vibrometer, the peak velocity amplitude spectrum was recorded in conjunction with that of the resultant waveform. Figure 5.23 shows the locations of the vibration amplitude measurement, including the front of the wedge tip, side of the wedge tip and the top of wedge tip. These amplitude values can indicate the motion of the wedge. Figure 5.24 shows the waveform of the axial displacement of the state-of-the-art PZT transducer and the prototype transducers.

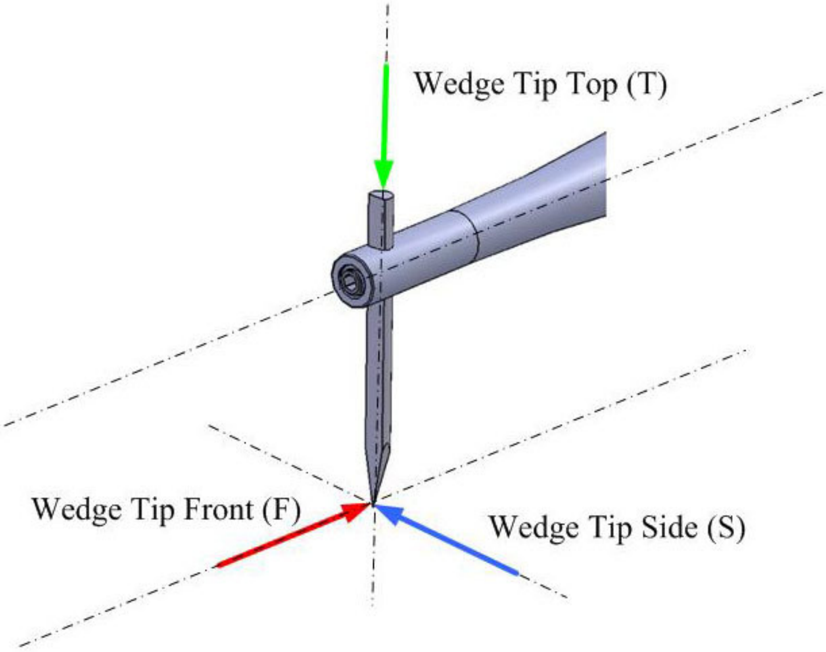

Figure 5.23 Diagram showing the locations of vibration amplitude measurements. Laser beam is indicated by an arrow.

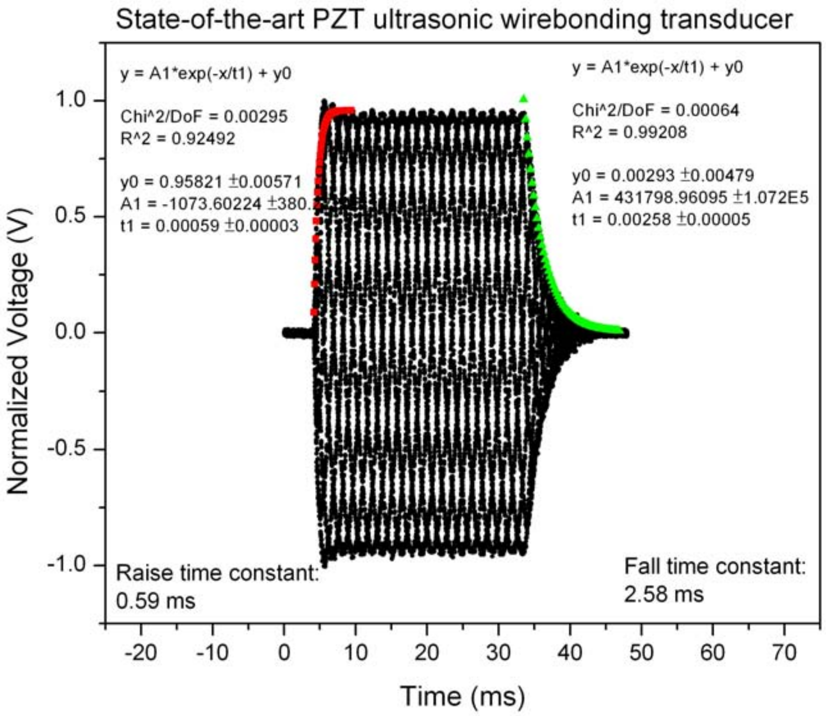
State-of-the-art PZT ultrasonic wirebonding transducer
y = A1*exp(-x/t1) + y0
Chi^2/DoF = 0.00295
R^2 = 0.92492
y0 = 0.95821 ±0.00571
A1 = -1073.60224 ±380.
t1 = 0.00059 ±0.00003
y = A1*exp(-x/t1) + y0
Chi^2/DoF = 0.00064
R^2 = 0.99208
y0 = 0.00293 ±0.00479
A1 = 431798.96095 ±1.072E5
t1 = 0.00258 ±0.00005
Raise time constant:
0.59 ms
Fall time constant:
2.58 ms
Normalized Voltage (V)
1.0
0.5
0.0
-0.5
-1.0
-20
-10
0
10
20
30
40
50
60
70
Time (ms)

(a)

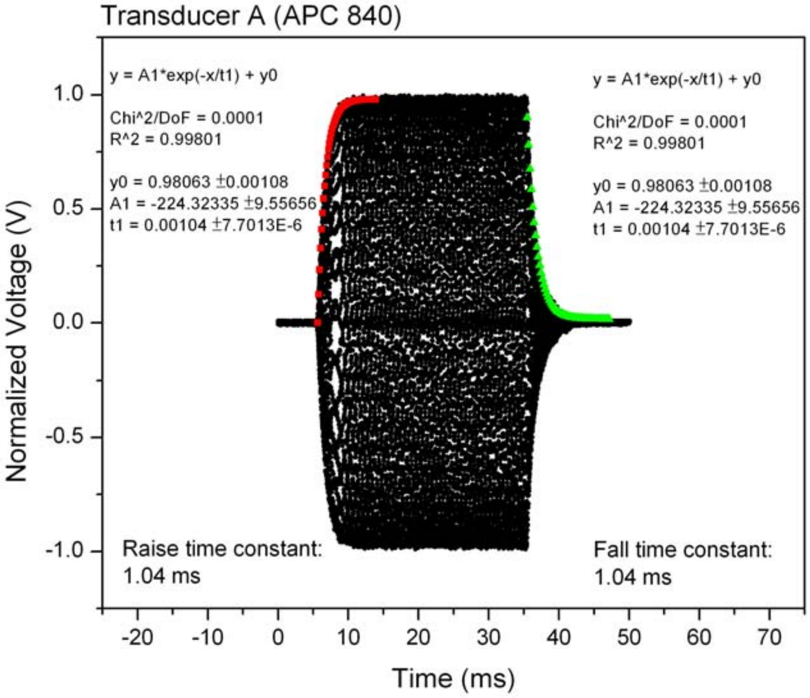
Transducer A (APC 840)
y = A1*exp(-x/t1) + y0
Chi^2/DoF = 0.0001
R^2 = 0.99801
y0 = 0.98063 ±0.00108
A1 = -224.32335 ±9.55656
t1 = 0.00104 ±7.7013E-6
y = A1*exp(-x/t1) + y0
Chi^2/DoF = 0.0001
R^2 = 0.99801
y0 = 0.98063 ±0.00108
A1 = -224.32335 ±9.55656
t1 = 0.00104 ±7.7013E-6
Raise time constant:
1.04 ms
Fall time constant:
1.04 ms
Normalized Voltage (V)
1.0
0.5
0.0
-0.5
-1.0
-20
-10
0
10
20
30
40
50
60
70
Time (ms)

(b)

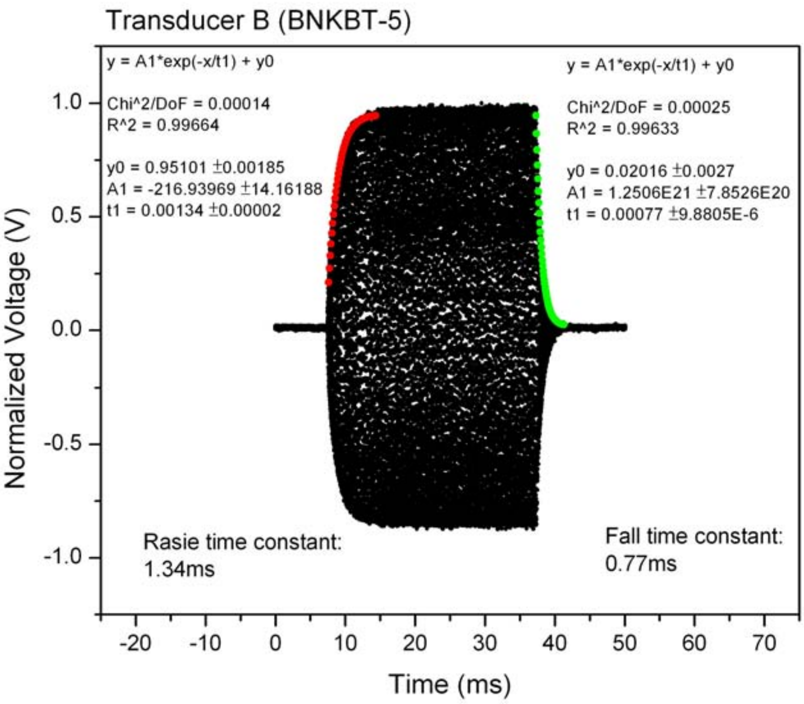
Transducer B (BNKBT-5)
y = A1*exp(-x/t1) + y0
Chi^2/DoF = 0.00014
R^2 = 0.99664
y0 = 0.95101 ±0.00185
A1 = -216.93969 ±14.16188
t1 = 0.00134 ±0.00002
y = A1*exp(-x/t1) + y0
Chi^2/DoF = 0.00025
R^2 = 0.99633
y0 = 0.02016 ±0.0027
A1 = 1.2506E21 ±7.8526E20
t1 = 0.00077 ±9.8805E-6
Rasie time constant:
1.34ms
Fall time constant:
0.77ms
Normalized Voltage (V)
1.0
0.5
0.0
-0.5
-1.0
-20
-10
0
10
20
30
40
50
60
70
Time (ms)

(c)

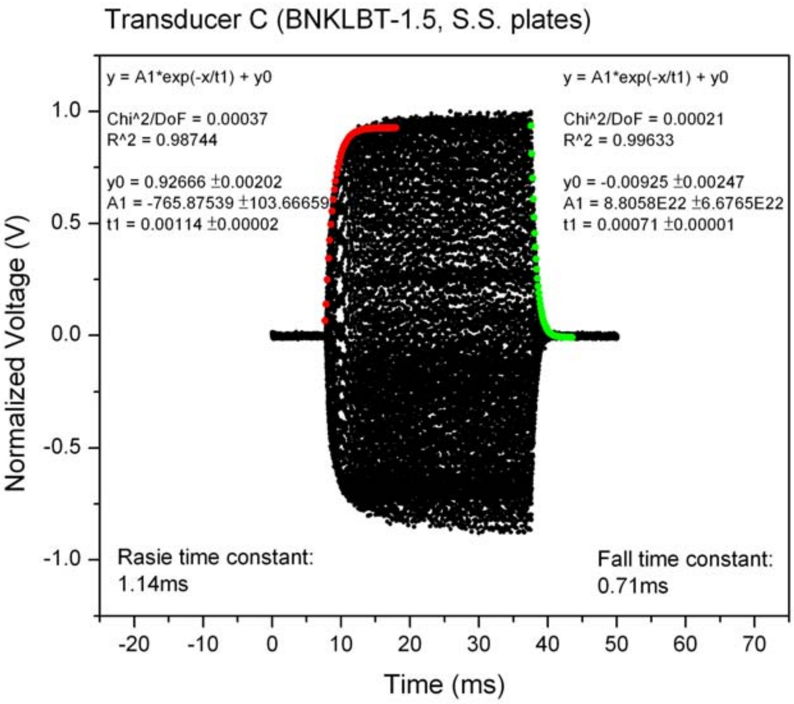
Transducer C (BNKLBT-1.5, S.S. plates)
y = A1*exp(-x/t1) + y0
Chi^2/DoF = 0.00037
R^2 = 0.98744
y0 = 0.92666 ±0.00202
A1 = -765.87539 ±103.66659
t1 = 0.00114 ±0.00002
y = A1*exp(-x/t1) + y0
Chi^2/DoF = 0.00021
R^2 = 0.99633
y0 = -0.00925 ±0.00247
A1 = 8.8058E22 ±6.6765E22
t1 = 0.00071 ±0.00001
Rasie time constant:
1.14ms
Fall time constant:
0.71ms
Normalized Voltage (V)
1.0
0.5
0.0
-0.5
-1.0
-20
-10
0
10
20
30
40
50
60
70
Time (ms)

(d)

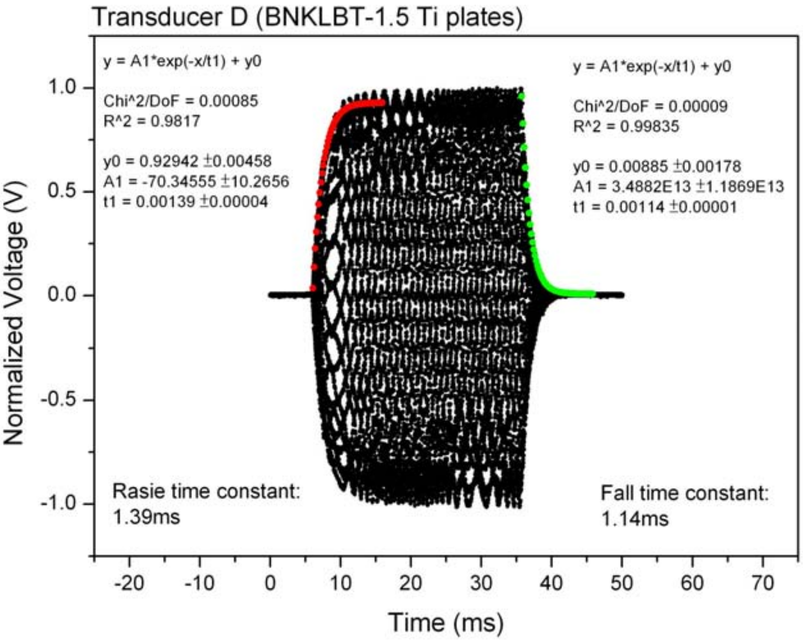

(e)

Figure 5.24 Axial vibration response measured at the front of wedge tip with normalized voltage. (a) State-of-the-art PZT transducer, (b) Prototype Transducer A, (c) Prototype Transducer B, (d) Prototype Transducer C and (e) Prototype Transducer D.

5.6.2.2. Results and discussion

Table 5.3 summarized the vibration amplitude measurements at different locations on the transducers. During the bonding action, envelop of sine waves corresponding to the transducer resonance frequency was received by the transducer. The transducer has a responding time to increase/decrease the vibration amplitude to the desired level. That corresponding times are called the rise time and fall time. Since the delay is mainly related to the R-C circuit (capacitance of transducer) and/or the design of the transducer, the profile is a first order exponential function. The time constant of the rising/falling time can be found by using exponential fitting. The result of the fitting and the time constant of the corresponding transducers are shown in Figure 5.24. Both PZT and the state-of-the-art and the Transducer A, have very high axial vibration amplitude which exceeds 1.5 μm. But both transducers have relatively large lateral displacement and thus the ratio of axial displacement to lateral displacement (F:S and F:T ratio, see Figure 5.23) are relatively small, especially the F:S ratio. The locus of vibration measured on the wedge tip will become an ellipse as shown in Figure 5.27. When the lateral displacement is large, the bond width will increase and that is not desirable. Hence, to maintain a high F:S ratio is important for miniaturization as a narrow bond width can be achieved. The transducers (Transducers B and C) using lead-free materials equipped with stainless steel (S.S.) front and back plates only have about 70% axial vibration of the lead-based transducer. The advantage of the lead-free transducers is having a smaller lateral vibration thus with high F:S and F:T ratio. The lateral vibration is mainly due to the lateral vibration of the driving material, thus the lateral vibration can effectively be reduced by using driving materials with lower electromechanical coupling coefficient in the lateral direction (k_{31}). Fabricating 1-3 ceramic/polymer composites is a good way to reduce k_{31} thus the performance of the transducer can be enhanced (Chong *et al.* 2004). Here, using BNKBT-5 and BNKLBT-1.5, which have a much smaller k_{31} than the PZT APC 840, can effectively reduce the energy transfer to the lateral vibration and thus improve the ratio between axial vibration to lateral vibration.

Transducer D has large axial vibration and relatively small lateral vibration. The relatively small lateral vibration amplitude is due to the intrinsic characteristic of lead-free material as mentioned previously. Large axial vibration is mainly due to the design of the driver which is related to the acoustic impedance between the materials. Ultrasonic wirebonding transducer is a device operating at it 1.5λ axial vibrational mode, which is mainly contributed by the axial vibration of the driver. The axial vibration of the driver is generated by the thickness mode vibration of the driving elements (piezoelectric ceramics). By converse piezoelectric effect, piezoelectric ceramics convert electrical energy to mechanical energy. The mechanical energy is the source of the vibration, firstly transferred to the metal plates in the driver and then transferred to the horn. The acoustic impedance between the piezoelectric ceramics and the metal plates (front and back plates) is a critical factor that determined the efficiency of energy transfer in the ultrasonic wirebonding transducer. The increase of the mismatch of acoustic impedance result in a decrease in efficiency. The acoustic impedance of the driving materials in the thickness mode is listed in Table 5.3. The acoustic impedance of stainless steel and titanium alloy is 45.7 MRayl and 27.3 MRayl, respectively (Onda_Corporation). The acoustic impedance of titanium alloy is close to both BNKBT-5 and BNKLBT-1.5 hence vibration energy can be transferred more effectively which greatly improves the axial vibration performance. It has been found that the BNKLBT-1.5 transducer has better performance than the BNKBT-5 transducer in the preliminary study thus BNKLBT-1.5 was selected to be sandwiched between the titanium front and back plates.

Table 5.3 Vibration amplitudes and other related parameters at different positions of the transducers. The input power is 0.1 W.

Transducer type	State-of-the-art PZT transducer	Transducer A	Transducer B	Transducer C	Transducer D
Wedge tip, Front (μm)	1.566	1.693	1.386	0.956	1.669
Wedge tip, Side (μm)	0.160	0.191	0.068	0.085	0.082
Wedge tip, Top (μm)	0.118	0.196	0.066	0.029	0.060
F:S ratio	9.79	8.86	20.29	11.27	20.23
F:T ratio	13.27	8.63	21.11	32.61	27.89
Rise time constant, τ_r (ms)	0.59	1.04	1.34	1.14	1.39
Fall time constant, τ_f (ms)	2.58	1.04	0.77	0.71	1.14

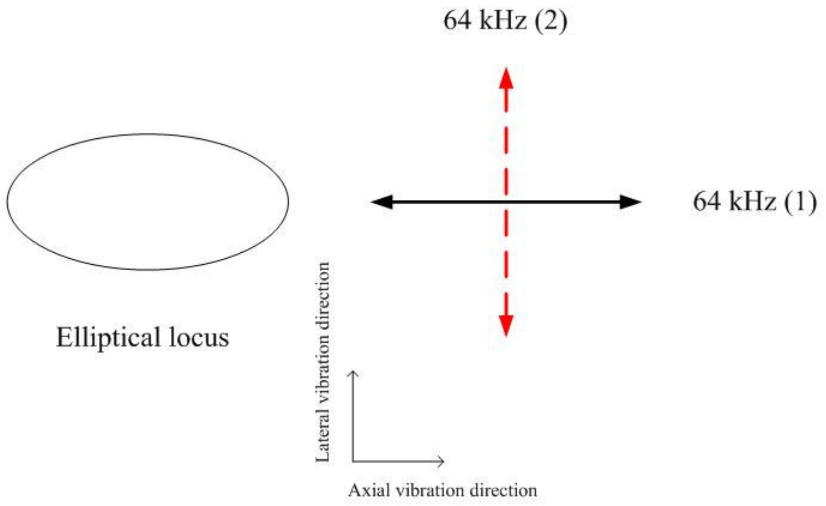

Figure 5.25 Schematic diagram of the vibration locus of the welding tip.

5.6.3. CHARACTERISTICS AT DIFFERENT INPUT POWER

The output power of the ultrasonic wirebonding transducer can be varied under different bonding conditions and the output power is determined by the electrical input power. It is important to have a transducer with high stability for industrial applications. The vibrational performance of different prototype transducers with varied input power from 0.05 W to 0.3 W is shown in Figures 5.27, 5.28 and 5.29, respectively. The axial vibration of the wedge tip is approximately linearly proportional to the input power, but the lateral vibration of the wedge tip, including both tip side and wedge top, is different in different prototype transducers. It is observed that lead-based transducers have higher axial vibration and high lateral vibration thus have relatively low F:S ratio and F:T ratio which is due to the intrinsic properties of PZT having high k_{31}. Both lead-free transducers with S.S. front and back plates perform well in F:S and F:T ratio at low input power. The ratios decrease as the input power increases which could be due to the stronger excitation in lateral mode at high power driving. Transducer D has a steady F:S and F:T ratios over the measuring range and has a better performance in reducing the lateral vibration than the lead-based transducer. In addition, the axial vibration at the wedge tip of Transducer D is comparable with lead-based transducer. This indicates that the lead-free ceramics, BNKLBT-1.5, can be a potential candidate for the ultrasonic wirebonding transducer application.

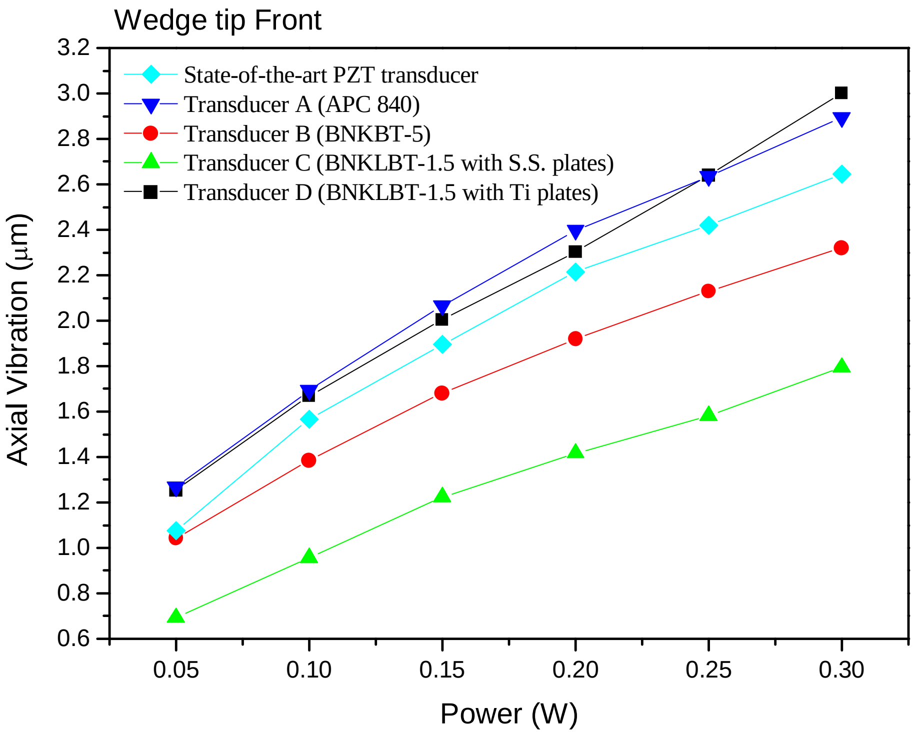

Figure 5.26 Plots of the axial vibration of the wedge tip versus the input power for various transducers.

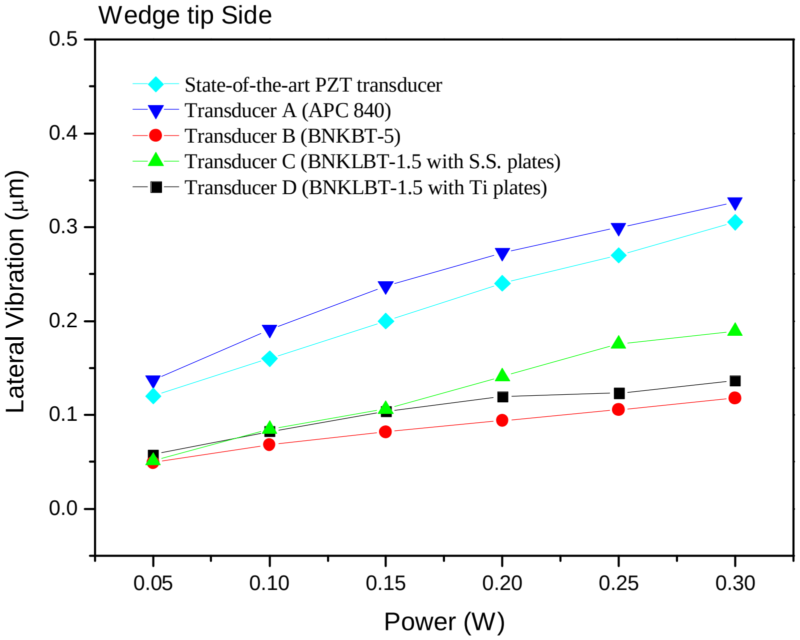

(a)

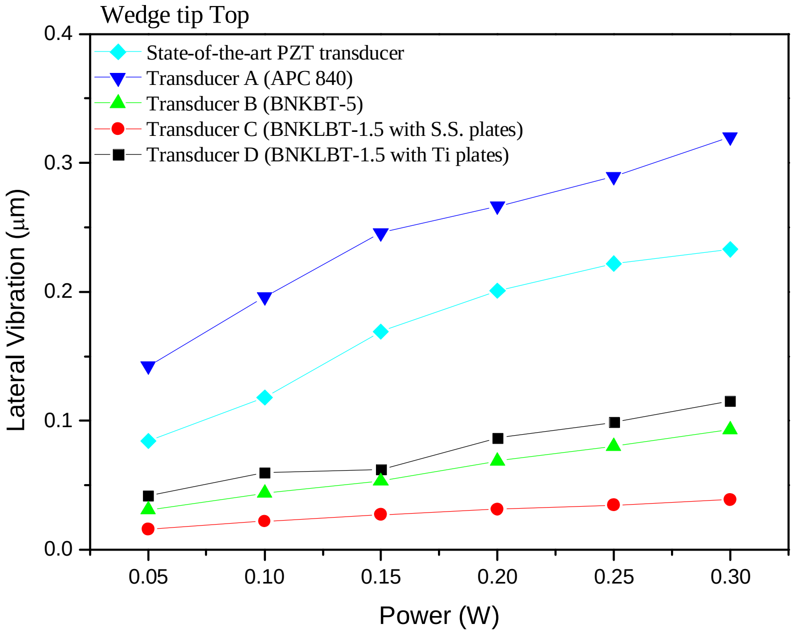

(b)

Figure 5.27 Plots of (a) the lateral vibration of the wedge tip side and (b) the lateral vibration of the wedge tip top versus the input power for various transducers.

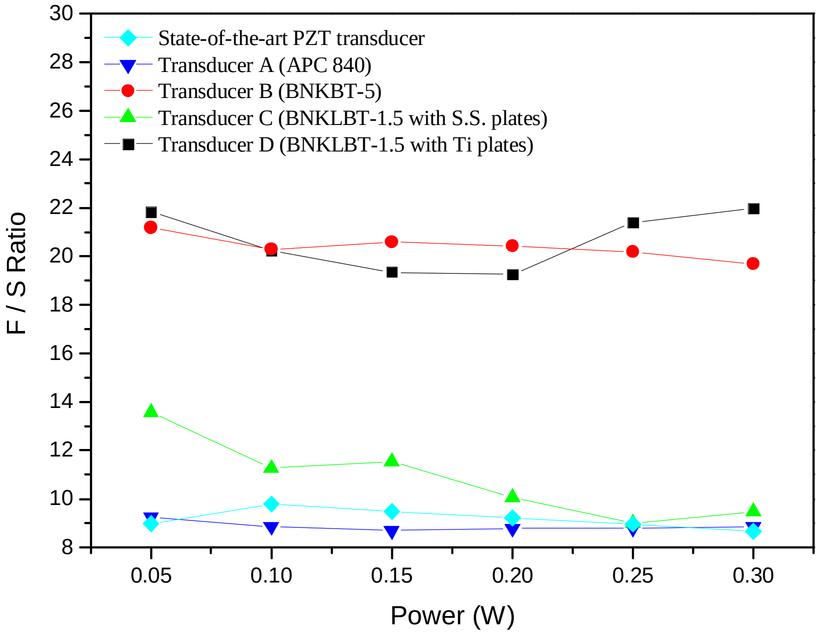

(a)

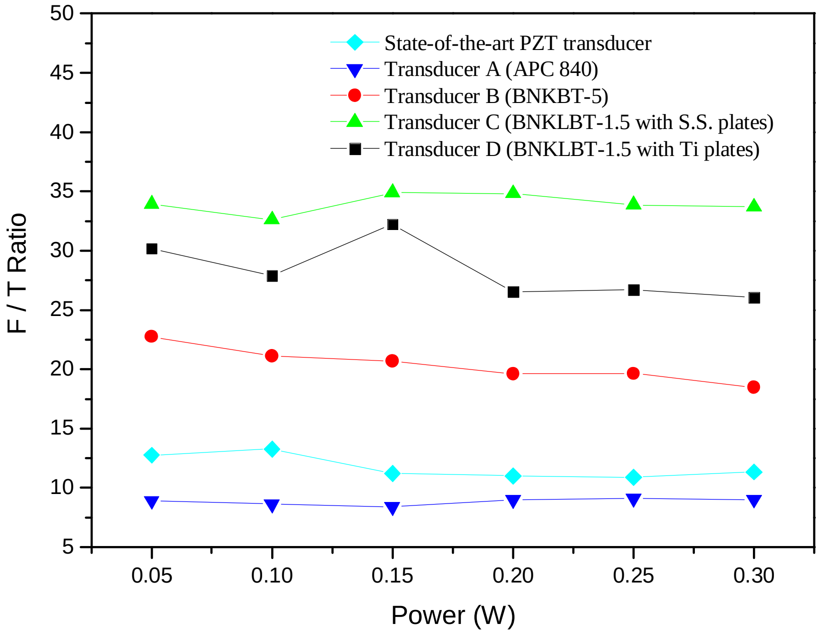

(b)

Figure 5.28 Plots of (a) F:S ratio and (b) F:T ratio of the wedge tip versus the input power for various transducers.

5.7. CONCLUSION

Prototype ultrasonic wirebonding transducers with different driving elements and different metal front and back plates were fabricated and their performances evaluated. A three-dimensional finite element method (FEM) analysis was used to simulate the vibration characteristic of the prototype transducers. Four different types of wedge-bonding transducers operating at ~63 kHz were fabricated. Their performance were evaluated and compared with state-of-the-art PZT wirebonding transducer. The vibrational parameter of the prototype transducers were studied at 0.1W input power, which is the standard driving power of the state-of-the-art transducer. The vibration amplitudes of the transducer at different locations were measured by using the laser Doppler vibrometer. A large axial vibration on the wedge tip front was recorded in both lead-based ultrasonic transducers (state-of-the-art transducer and Transducer A) and a large lateral vibration was also found on the wedge tip thus resulting in a relatively low F:S and F:T ratios. The vibration amplitude of lead-free transducers with S.S. front and back plates (Transducers B and C) have a smaller axial vibration, which is ~70% of amplitude observed in lead-based transducers, but have much smaller lateral vibration. As the lateral vibration is mainly governed by the lateral vibration of driving materials and lead-free materials have much lower electromechanical coupling coefficient than lead-based materials in the lateral direction. Transducer D, using BNKLBT-1.5 as driving materials and has titanium front and back plates, has a comparable axial vibration amplitude as lead-based transducers and also has a relatively small lateral vibration simultaneously. In addition, Transducer D has good linearity over different input power which is a potential candidate for replacing lead-based wirebonding transducer.

CHAPTER 6 CONCLUSIONS AND SUGGESTIONS FOR FUTURE WORK

6.1. CONCLUSION

A BNT-based ternary system combining bismuth sodium titanate, bismuth potassium titanate $(Bi_{0.5}K_{0.5})TiO_3$ (BKT) and barium titanate $BaTiO_3$ (BT), have been investigated. The composition 0.90(BNT) - 0.05(BKT) - 0.05(BT) (BNKBT-5) has been found to have good piezoelectric, ferroelectric and dielectric properties. BNKBT-5 was chosen as the base material in this study. The properties of BNKBT-5 can be modified by using additives/dopings. Three different materials were used as the additives/dopings, including cerium oxide (CeO_2), dicalcium ferrite ($Ca_2Fe_2O_5$) and bismuth lithium titanate ($Bi_{0.5}Li_{0.5}TiO_3$, BLT). All the ceramic samples were fabricated by conventional metal mix oxide method. The dielectric, piezoelectric and ferroelectric properties were investigated by different methods and studied the effect of adding different additives/dopings studied.

Pure BNKBT-5 ceramics with single perovskite phase was sintered at 1170 ^{o}C to produce an averaged grain size of 2-3 μm and had single perovskite phase. The coercive field E_c and remnant polarization P_r at room temperature was 3.45 MV/m and 28.23

$\mu C/cm^2$, respectively. The depolarization temperature and the Curie temperature were ~110 ^oC and ~300 ^oC, respectively. The piezoelectric d_{33} constant of BNKNT-5 was 165 pC/N. The electromechanical coupling coefficient k_p and k_t were found to be 0.313 and 0.462, respectively.

In the BNKBT-5 + x mol% CeO_2 system (x ranged from 0-1 mol%), CeO_2 was added as an additive. Small amount of CeO_2 additive can enhance both ferroelectric, piezoelectric and dielectric properties. The optimum additive level in this system was x = 0.25 mol%. In this composition, the remnant polarization P_r and piezoelectric d_{33} constant increased to 31.1 $\mu C/cm^2$ and 178 pC/N respectively, and the dielectric loss could be reduced by over 20%. Both the electromechanical coupling coefficients and mechanical quality factors in the radial and thickness modes were enhanced. The T_d in this composition was over 100 ^oC which is in the acceptable temperature range for application.

Dicalcium ferrite ($Ca_2Fe_2O_5$) was doped into BNKBT-5 with the formula (1-x)BNKBT-5 – (x) $Ca_2Fe_2O_5$ with x ranged from 0-1 mol%. $Ca_2Fe_2O_5$ could improve the sintering ability and density of BNKBT-5. After doped with dicalcium ferrite, the coercive field increased from 3.5 MV/m to ~4 MV/m and the remnant polarization remained steady. The increment of coercive field is a common phenomenon for doping “hard” dopants, such as $Ca_2Fe_2O_5$. Hard dopings can improve the mechanical properties and reduce the dielectric loss of the ceramics. The dielectric loss was reduced by over

20% compared with the pure BNKBT-5 and the mechanical quality factors Q_M in both radial and thickness modes reached the peak values when x = 0.75 mol%, which was over 70% improvement. The optimum doping level in this system occured when x = 0.5 mol%. Other than the improvement in mechanical properties and dielectric properties, the k_t reached the peak value in this composition and k_p was also slightly enhanced. The piezoelectric d_{33} constant reduced from 165 pC/N to ~140 pC/N and the T_d and T_c were ~100 ^oC and ~300 ^oC, respectively.

Another modification was based on the chemical formula (0.90-x) $(Bi_{0.5}Na_{0.5})TiO_3 – 0.05(Bi_{0.5}K_{0.5})TiO_3 – (x)(Bi_{0.5}Li_{0.5})TiO_3 – 0.05BaTiO_3$ system with x ranged from 0 to 2.5 mol% (BNKLBT-100x). The ferroelectric properties were greatly enhanced while P_r increased to 32.3 $\mu C/cm^2$, about 15% improvement, at x = 1.5 mol%. This composition (x = 1.5 mol%, BNKLBT-1.5) also had the best performance in this system. The T_d and T_c in BNKLBT-1.5 were 140 ^oC and 320 ^oC, respectively. The dielectric loss was reduced significantly from ~2.6% to ~1.6% (over 30% reduction). Both electromechanical coupling factor (k_p, k_t) and mechanical quality factor ($Q_{M(radial)}$, $Q_{M(thickness)}$) increased after doped with Li^+. BNKLBT-1.5 sample giving maximum k_t, $Q_{M(radial)}$ and $Q_{M(thickness)}$ values of 0.524, 142 and 102, respectively. Comparing with undoped samples, there were ~14%, 31% and ~81% increment in k_t, $Q_{M(radial)}$ and $Q_{M(thickness)}$ values, respectively. The k_t (=0.524) value was superior compared to most of the reported BNT-based lead-free materials. Another important factor, the d_{33} piezoelectric constant, did not have much variation after doping Li^+ and retained a relatively high value ranged from 160-170 pC/N.

Based on experimental results, the best composition BNKLBT-1.5was used to fabricate piezoelectric devices. Both BNKBT-5 and BNKLBT-1.5 were characterized according to the IEEE standard method to obtain the full sets of material parameters. Those material parameters were used in designing the device using finite element method (FEM).

Different piezoelectric materials were used as the transduction element in the prototype piezoelectric accelerometers, including PZT APC840, BNKBT-5 and BNKLBT-1.5. The principle of piezoelectric accelerometer is based on the direct piezoelectric effect. The prototype accelerometers used the compressive-type design, with stainless steel seismic mass, base and housing; 1.17mm diameter PTFE insulated coaxial cables with length of ~30 cm, copper electrodes and BNC connectors. The optimum pre-stressing condition was applied by a 60 kgf-cm torque driver. The electrical properties of the accelerometers, within 40 Hz to 20 kHz, were measured using an HP4294A impedance analyzer and no strong resonance peak within this frequency range was found for all prototype accelerometers. The sensitivity of the prototype accelerometers were calibrated using a back-to-back calibration method at room temperature and Brüel & Kjær Standard Reference Accelerometer Type 8305 was used. The sensitivity of APC 840, BNKBT-5 and BNKLBT-1.5 accelerometers were found to be 4.34 pC/ms^{-2}, 2.24 pC/ms^{-2} and 2.97 pC/ms^{-2}, respectively. The useable frequency ranges were 50 Hz – 8.24 kHz, 50 Hz – 10.1 kHz and 50 Hz – 12.45 kHz, respectively.

Another piezoelectric device using the converse piezoelectric effect was also studied which is the ultrasonic wirebonding transducer. The ultrasonic wirebonding transducer is a device operating at its 1.5λ axial vibration resonance mode and this mode is mainly governed by the thickness vibration of the driving element. A three-dimensional finite element analysis was used to model the vibration characteristic of the transducers with different driving elements and different metal front and back plates. Several non-axial vibration resonances could be found to exist around the operating frequency (~64 kHz) which could affect the bonding condition. The APC 840 transducer (Transducer A) has the torsional mode much closer than that observed in lead-free based transducers (Transducers B, C and D).

Four different types of wedge-bonding transducers operated at ~64 kHz were fabricated. Their performance were evaluated and compared with state-of-the-art wirebonding transducer. The vibrational parameter of the prototype transducers were firstly studied at 0.1 W input power. The vibration amplitude of the transducer at different locations were measured using the laser Doppler vibrometer. Lead-based ultrasonic transducers (state-of-the-art transducer and Transducer A) have large axial and lateral displacements at the wedge tip. The vibration amplitude of lead-free transducers with S.S. front and back plates (Transducers B and C) have a smaller axial vibration, which is about 70% of the lead-based transducers, and much smaller lateral vibration. As the lateral vibration is mainly governed by the lateral vibration of driving materials and lead-free materials have lower electromechanical coupling coefficient than lead-based materials in the lateral direction. Transducer D, using BNKLBT-1.5 as driving materials and has titanium front and back plates, have an axial vibration amplitude comparable at the wedge tip to that of lead-based transducers and also has a relatively small lateral vibration. In addition, Transducer D has good linearity over different input power which makes it a potential candidate for replacing lead-based wirebonding transducer.

6.2. SUGGESTIONS FOR FUTURE WORK

In this work, the properties of the BNT-based lead-free ceramics have been improved using various methods and BNKLBT-1.5 has been found to have the best properties. However, there is still room for improvement, especially in varying the additives/dopants to further enhance the ceramics properties.

The frequency range of the prototype accelerometer can be further improved by replacing the normal coaxial cable with a “low-noise” cable, which is currently used by different sensor manufacturers. This can lower the noise floor of the accelerometer and allows it to measure acceleration down to 1 Hz.

The prototype wirebonding transducer, with BNKLBT-1.5 as driving element equipped with titanium front and back plates, has large axial vibration amplitude at the wedge tip which is comparable to the state-of-the-art wirebonding transducer with PZT as driving element. The relative small amplitude in lateral vibration is an advantage to reduce the elliptical locus during the bonding thus could produce finer bond. Prototype transducers can be further optimised and installed onto the bondhead of automatic wire bonder for further characterisation in the future.

REFERENCES

ANSI/IEEE, *IEEE STANDARD ON PIEZOELECTRICITY*, The Institution of Electrical and Electronic Engineers, Inc.1987.

Aparna, M., Bhimasankaram, T., Kumar, G. S. and Prasad, G. Synthesis and characterization of lanthanum doped sodium bismuth titanate. *MODERN PHYSICS LETTERS B*, 2002, 16(26), 1007.

Aurivullius, B. Mixed bismuth oxides with layer lattices. II. Structure of $Bi_4Ti_3O_{12}$. *ARKIV FUR KEMI*, 1949, 1, 499.

B&K, *TECHNICAL REVIEW NO. 3 AND NO. 4." BV0031 & BV0032*. Denmark, Brüel & Kjær Ltd.1987.

B&K, *TECHNICAL DOCUMENTATION OF MULTICHANNEL ANALYSIS SYSTEM TYPE 3550*. Denmark, Brüel & Kjær Ltd.1992.

Belding, J. H. and M.G., M. Behavior of Modified Lead Zirconate-Lead Titanate Piezoelectric Ceramics Under High Electric Fields. *AMERICAN CERAMIC SOCIETY BULLETIN*, 1970, 49, 1025.

Berlincourt, D. A., Curran, D. R. and Jaffe, H.. Piezoelectric and piezomagnetic materials and their function in transducer. *PHYSICAL ACOUSTICS*. W. P. Mason. New York, Academic Press. 1964, 1**,** 169.

Buhrer, C. F. Some properties of bismuth perovskites. *JOURNAL OF CHEMICAL SOCIETY*, 1962, 36, 798.

Burgt, C. M. and Stuijts, A. L. Motional positive feedback system for ultrasonic power generators. *IEEE TRANSACTIONS ON ULTRASONIC ENGINEERING*, 1963, UE-10(2), 2.

Callister, W. D., *MATERIALS SCIENCE AND ENGINEERING: AN INTRODUCTION*. New York, John Wiley & Sons, Inc.1997.

Cho, J. H., Lee, Y. H., Chu, B. J., Kim, B. I. and Chung, H. T. Processing and properties of piezoelectrics based on BNT (Bi,Na)TiO_3. *EURO CERAMICS VIII, PTS 1-3*, 2004, 264-268, 1321.

Chong, C. P., Li, H. L., Chan, H. L. W. and Liu, P. C. K. Study of 1-3 composite transducer for ultrasonic wirebonding application. *CERAMIC INTERNATIONAL*, 2004, 30, 1141.

Cook, R. D., *FINITE ELEMENT MODELING FOR STREE ANALYSIS*. New York, John Wiley & Sons, Inc.1995.

Chu, B. J., Li, G. R., Jiang, X. P. and Chen, D. R. Piezoelectric property and relaxation phase transition of $Na_{1/2}Bi_{1/2}TiO_3$-$BaTiO_3$ system. *JOURNAL OF INORGANIC MATERIALS*, 2000, 15(5), 815.

Chu, B. J., Chen, D. R., Li, G. R. and Yin, Q. R. Electrical properties of $Na_{1/2}Bi_{1/2}TiO_3$-$BaTiO_3$ ceramics. *JOURNAL OF THE EUROPEAN CERAMIC SOCIETY*, 2002, 22, 2115.

Cohen, R. E. Orgin of Ferroelectricity in Perovskite Oxides. *NATURE*, 1992, 358, 136.

Curie, J. and Curie, P. *COMPTES RENDUS*, 1880, 91, 294.

Dally, J. W., Riley, W. F. and McConnell, K. G., *INSTRUMENTATION FOR ENGINEERING MEASUREMENTS*. New York, John Wiley & Sons, Inc.1993.

Darlington, C. N. W. and Megaw, H. D. The low-temperature phase transition of sodium niobate and the structure of the low-temperature phase. *ACTA CRYSTALLOGRAPHICA SECTION B*, 1973, 29(10), 2171.

Fraden, J., *HANDBOOK OF MODERN SENSORS: PHYSICS, DESIGNS AND APPLICATIONS*. New York, AIP Press.1997.

Frederick, J. R., *ULTRASONIC ENGINEERING*. New York, John Wiley & Sons, Inc.1965.

Gautschi, G., *PEIZOELECTRIC SENSORICS: FORCE, STRAIN, PRESSURE, ACCELERATION AND ACOUSTIC EMISSION SENSORS, MATERIALS AND AMPLIFIERS*. New York, Springer-Verlag Berlin Heidelberg, 2002.

Gomah-Pettry, J., Marchet, P., Simon, A., Von der Muhll, R., Maglione, M. and Mercurio, J. Dielectric properties of $Na_{0.5}Bi_{0.5}TiO_3$-$BaTiO_3$ ceramics. *INTEGRATED FERROELECTRICS*, 2004, 61, 155.

Guo, Y. P., Kakimoto, K. and Ohsato, H. Dielectric and piezoelectric properties of lead-free $(Na_{0.5}K_{0.5})NbO_3$–$SrTiO_3$ ceramics. *SOLID STATE COMMUNICATIONS*, 2004a, 129, 279.

Guo, Y. P., Kakimoto, K. and Ohsato, H. Phase transitional behavior and piezoelectric properties of $(Na_{0.5}K_{0.5})NbO_3$-$LiNbO_3$ ceramics. *APPLIED PHYSICS LETTERS*, 2004b, 85(18), 4121.

Guo, Y. P., Kakimoto, K. and Ohsato, H. Structure and electrical properties of lead-free $(Na_{0.5}K_{0.5})NbO_3$-$BaTiO_3$ ceramics. *JAPANESE JOURNAL OF APPLIED PHYSICS PART 1-REGULAR PAPERS SHORT NOTES & REVIEW PAPERS*, 2004c, 43(9B), 6662.

Guo, Y. P., Kakimoto, K. and Ohsato, H. $(Na_{0.5}K_{0.5})NbO_3$-$LiTaO_3$ lead-free piezoelectric ceramics. *MATERIALS LETTERS*, 2005, 59(2-3), 241.

Hankel, W. G. *ABH. SÄCHS.*, 1881, 12, 457.

Harper, C. A., *ELECTRONIC MATERIALS ANS PROCESSES HANDBOOK*, The McGraw-Hill Companies, Inc, 2004.

Harris, C. M. and Piersol, A. G., *SHOCK AND VIBRATION HANDBOOK*, McGraw-Hill Book Company, 2002.

Herbert, J. M., *FERROELECTRIC TRANSDUCERS AND SENSORS*. New York, Gordon and Breach, 1982.

Hirose, M., Suzuki, T., Oka, H., Itakura, K., Miyauchi, Y. and Tsukada, T. Piezoelectric Properties of $SrBi_4Ti_4O_{15}$ - Based Ceramics. *JAPANESE JOURNAL OF APPLIED PHYSICS PART 1-REGULAR PAPERS SHORT NOTES & REVIEW PAPERS*, 1999, 38(9B), 5561.

Hiruma, Y., Aoyagi, R., Nagata, H. and Takenaka, T. Ferroelectric and piezoelectric properties of $(Bi_{1/2}K_{1/2})TiO_3$ ceramics. *JAPANESE JOURNAL OF APPLIED PHYSICS PART 1-REGULAR PAPERS SHORT NOTES & REVIEW PAPERS*, 2005, 44(7A), 5040.

Hom, C. L., Pilgrim, S. M., Shankar, N., Bridger, K., Massuda, M. and Winzer, S. R. Calculation of Quasi-Static Electromechanical Coupling Coefficients for Electrostrictive Ceramic Materials. *I.E.E.E. TRANSACTION ON ULTRASONIC, FERROELECTRICITY AND FREQUENCY CONTROL*, 1994, 41(4), 542.

ISA Electrical Transducer Norenclature and Terminology. *AMERICAN NATIONAL STANDARD*, 1982, ANSI/ISA-S37.1-1975 (R1982).

ISO, *ISO 2041: 1990: VIBRATION AND SHOCK - VOCABULARY*, ISO, Geneva,1990.

IRE, *IRE STANDARDS ON PIEZOELECTRIC CRYSTALS: MEASUREMENTS OF PIEZOELECTRIC CERAMICS*, 1961.

Ivanova, V. V., Kapyshev, A. G., Venevtsev, Y. N. and Zhdanov, G. S. *IZV. AKAD. NAUK SSSR*, 1962, 26, 354.

Jaeger, R. E. and Egerton, L. Hot pressing of Potassium-sodium Niobates. *JOURNAL OF THE AMERICAN CERAMIC SOCIETY*, 1962, 45, 209.

Jaffe, B., Cook, W. R. and Jaffe, H., *PIEZOELECTRIC CERAMICS*, Academic Press Ltd., 1971.

Jiang, W. J., Cao, W. W., Yi, X. J. and Chen, H. C. The elastic and piezoelectric properties of tungsten bronze ferroelectric crystals $(Sr_{0.7}Ba_{0.3})_2NaNb_5O_{15}$ and $(Sr_{0.3}Ba_{0.7})_2NaNb_5O_{15}$. *JOURNAL OF APPLIED PHYSICS*, 2005, 97(9), 094106.

Jovalekic, C., M., P., P., O. and L., A. X-ray photoelectron spectroscopy study of $Bi_4Ti_3O_{12}$ ferroelectric ceramics. *APPLIED PHYSICS LETTERS*, 1998, 72, 1051.

Kaewkamnerd, N., Takenaka, T., Sakata, K. and Toda, K. Material characterization of $(Bi_{1/2}Na_{1/2})(0.94)Ba_{0.06}TiO_3$ ceramic as a lamb wave device substrate. *SENSORS AND MATERIALS*, 1997, 9(1), 47.

Kusumoto, K. (17th Oct 2005).*http://www.geocities.jp/kusumotokeiji/indexeng.html*

Langevin, P., Improvements Relating to the Emission and Receptions of Submatine Waves. B. P. Office. Great Britain, 1921.

Lefkowitz, I., Lukaszewicz, K. and Megaw, H. D. The high-temperature phases of sodium niobate and the nature of transitions in pseudosymmetric structures. *ACTA CRYSTALLOGRAPHICA*, 1966, 20(5), 670.

Li, H. D., Feng, C. D. and Yao, W. L. Some effects of different additives on dielectric and piezoelectric properties of $(Bi_{0.5}Na_{0.5})TiO_3$–$BaTiO_3$ morphotropic-phase-boundary composition. *MATERIALS LETTERS*, 2004, 58, 1194.

Li, J. F., Wang, K., Zhang, B. P. and Zhang, L. M. Ferroelectric and piezoelectric properties of fine-grained Na0.5K0.5NbO3 lead-free piezoelectric ceramics prepared by spark plasma sintering. *JOURNAL OF THE AMERICAN CERAMIC SOCIETY*, 2006, 89(2), 706.

Li, Y. M., Chen, W., Xu, Q., Zhou, J., Gu, X. Y. and Fang, S. Q. Electromechanical and dielectric properties of $Na_{0.5}Bi_{0.5}TiO_3$-$K_{0.5}Bi_{0.5}TiO_3$-$BaTiO_3$. *MATERIALS CHEMISTRY AND PHYSICS*, 2005, 94(2-3), 328.

Lin, D. M., Xiao, D. Q., Zhu, J. G. and Yu, P. Piezoelectric and ferroelectric properties of $[Bi_{0.5}(Na_{1-x-y}K_xLi_y)_{0.5}]TiO_3$ lead-free piezoelectric ceramics. *APPLIED PHYSICS LETTERS*, 2006, 88, 062901.

Lin, D. M., Xiao, D. Q., Zhu, J. G., Yu, P. and Yan, H. J. Researches and progresses of bismuth layer-based lead-free piezoelectric ceramics. *FUNCTIONAL MATERIALS*, 2003, 5, 491.

Lin, D. M., Xiao, D. Q., Zhu, J. G., Yu, P., Yan, H. J. and Li, L. Z. Synthesis and piezoelectric properties of lead-free piezoelectric $[Bi_{0.5}(Na_{1-x-y}K_xLi_y)_{(0.5)}]TiO_3$ ceramics. *MATERIALS LETTERS*, 2004a, 58(5), 615.

Lin, D. M., Xiao, D. Q., Zhu, J. G., Yu, P., Yan, H. J., Li, L. Z. and Zhang, W. The relations of sintering conditions and microstructures of $[Bi_{0.5}(Na_{1-x-y}K_xLi_y)_{0.5}]TiO_3$ piezoelectric ceramics. *CRYSTAL RESEARCH AND TECHNOLOGY*, 2004b, 39(1), 30.

Lines, M. E. and Glass, A. M., *PRINCIPLES AND APPLICATIONS OF FERROELECTRICS AND RELATED MATERIALS*, Oxford, Clarendon Press.1977.

Lippmann, M. G. *ANNALES DE PHYSIQUE ET DE CHIMIE, 5TH SERIES*, 1881, 24, 145.

Makiuchi, Y., Aoyagi, R., Hiruma, Y., Nagata, H. and Takenaka, T. $(Bi_{1/2}Na_{1/2})TiO_3$-$(Bi_{1/2}K_{1/2})TiO_3$-$BaTiO_3$-Based lead-free piezoelectric ceramics. *JAPANESE JOURNAL OF APPLIED PHYSICS PART 1-REGULAR PAPERS BRIEF COMMUNICATIONS & REVIEW PAPERS*, 2005, 44(6B), 4350.

Matsuo, K., Xie, R. J., Akimune, Y. and Sugiyama, T. Preparation of lead-free $Sr_{2-x}Ca_xNaNb_5O_{15}$ (x=0.1)-based piezoceramics with tungsten bronze structure. *JOURNAL OF THE CERAMIC SOCIETY OF JAPAN*, 2002, 110(5), 491.

Matthias, B. T. and Remeika, J. P. Ferroelectricity in the Ilmenite Structure. *PHYSICAL REVIEW*, 1949, 76(12), 1886.

Miranda, C., Costa, M. E. V., Avdeev, M., Kholin, A. L. and Baptista, J. L. Relaxor properties of Ba-based layered perovskites. *JOURNAL OF THE EUROPEAN CERAMIC SOCIETY*, 2001, 21, 1303.

Mitchell, R. H., *PEROVSKITES: MODERN AND ANCIENT*. Ontario, Almaz Press Inc., 2002.

Mitsui, T., Tatsuzaki, I. and Nakamura, E., *AN INTRODUCTION TO THE PHYSICS OF FERROELECTRICS*. London, Gordon and Breach Science Publishers Ltd., 1976.

Nachtigal, C. L., *INSTRUMENTATION AND CONTROL FUNDAMENTALS AND APPLICATIONS*. New York, John Wiley & Sons, Inc., 1990.

Nagata, H., Koizumi, N. and Takenaka, T. Lead-Free Piezoelectric Ceramics of $(Bi_{1/2}Na_{1/2})TiO_3$ -$BiFeO_3$ System. *KEY ENGINEERING MATERIALS*, 1999, 169-170, 37.

Nagata, H. and Takanaka, T. Lead-Free Piezoelectric Ceramics of $(Bi_{1/2}Na_{1/2})TiO_3$-1/2(Bi_2O_3•Sc_2O_3) System. *JAPANESE JOURNAL OF APPLIED PHYSICS PART 1-REGULAR PAPERS SHORT NOTES & REVIEW PAPERS*, 1997, 36(9B), 6055.

Nagata, H. and Takenaka, T. $(Bi_{1/2}Na_{1/2})TiO_3$-based non-lead piezoelectric ceramics. *JOURNAL OF THE KOREAN PHYSICAL SOCIETY*, 1998, 32, S1298.

Nagata, H., Yoshida, M., Makiuchi, Y. and Takenaka, T. Large piezoelectric constant and high Curie temperature of lead-free piezoelectric ceramic ternary system based on bismuth sodium titanate-bismuth potassium titanate-barium titanate near the morphotropic phase boundary. *JAPANESE JOURNAL OF APPLIED PHYSICS PART 1-REGULAR PAPERS SHORT NOTES & REVIEW PAPERS*, 2003, 42(12), 7401.

Neurgaonkar, R. R. Growth of Ferroelectric Tungsten Bronze Crystals and Thin-Films. *FERROELECTRICS*, 1989, 91, 209.

Neurgaonkar, R. R., Cory, W. K. and Oliver, J. R. Growth and Applications of Ferroelectric Tungsten Bronze Family Crystals. *PROCEEDINGS OF THE SOCIETY OF PHOTO-OPTICAL INSTRUMENTATION ENGINEERS*, 1985, 540, 146.

Neurgaonkar, R. R., Cory, W. K., Oliver, J. R., Clark, W. W., Wood, G. L., Miller, M. J. and Sharp, E. J. Growth and Ferroelectric Properties of Tungsten Bronze $Ba_{2-x}Sr_xK_{1-y}Na_yNb_5O_{15}$ (BSKNN) Single-Crystals. *JOURNAL OF CRYSTAL GROWTH*, 1987, 84(4), 629.

Neurgaonkar, R. R., Cory, W. K., Oliver, J. R., Sharp, E. J., Wood, G. L., Miller, M. J., Clark, W. W. and Salamo, G. J. Growth and Ferroelectric Properties of Tungsten Bronze $Sr_{2-x}Ca_xNaNb_5O_{15}$ Single-Crystals. *MATERIALS RESEARCH BULLETIN*, 1988a, 23(10), 1459.

Neurgaonkar, R. R., Hall, W. F., Oliver, J. R., Ho, W. W. and Cory, W. K. Tungsten Bronze $Sr_{1-x}Ba_xNb_2O_6$ - a Case-History of Versatility. *FERROELECTRICS*, 1988b, 87, 167.

Neurgaonkar, R. R., Oliver, J. R., Cory, W. K. and Cross, L. E. Ferroelectric Properties of Lanthanum-Modified $Sr_{0.6}Ba_{0.4}Nb_2O_6$ Single-Crystals. *JOURNAL OF CRYSTAL GROWTH*, 1988c, 89(4), 463.

Ogawa, T. Ferroelectric domain structures in lead free piezoelectric ceramics composed of Bi-layer structured $SrBi_4Ti_4O_{15}$. *JOURNAL OF THE EUROPEAN CERAMIC SOCIETY*, 2004, 24(6), 1517.

Oka, H., Hirose, M., Tsukada, T., Watanabe, Y. and Nomura, T. Thickness-Shear Vibration Mode Characteristics of $SrBi_4Ti_4O_{15}$-Based Ceramics. *JAPANESE JOURNAL OF APPLIED PHYSICS PART 1-REGULAR PAPERS SHORT NOTES & REVIEW PAPERS*, 2000, 39, 5613.

Onda_Corporation. (15th Dec 2002). from http://www.ondacorp.com/tecref_acoustictable.html.

Peng, C., Li, J. F. and Gong, W. Preparation and properties of $(Bi_{1/2}Na_{1/2})TiO_3$-$Ba(Ti,Zr)O_3$ lead-free diezoelectric ceramics. *MATERIALS LETTERS*, 2005, 59(12), 1576.

Polytec, *VIBROMETER OPERATOR'S MANUAL FOR POLYTEC VIBROMETER SERIES 3000*, Polytech PI. Inc., 1995.

Saito, Y., Takao, H., Tani, T., Nonoyama, T., Takatori, K., Homma, T., Nagaya, T. and Nakamura, M. Lead-free piezoceramics. *NATURE*, 2004, 432(7013), 84.

Sakowski-Cowley, A. C., Lukaszewicz, K. and Megaw, H. D. The structure of sodium niobate at room temperature, and the problem of reliability in pseudosymmetric structures. *ACTA CRYSTALLOGRAPHICA SECTION B*, 1969, 25(5), 851.

Sanson, A. and Whatmore, R. W. Properties of $Bi_4Ti_3O_{12}$ - $(Na_{1/2}Bi_{1/2})TiO_3$ Piezoelectric Ceramics. *JAPANESE JOURNAL OF APPLIED PHYSICS PART 1-REGULAR PAPERS SHORT NOTES & REVIEW PAPERS*, 2002, 41(11B), 7127.

Sasaki, A., Chiba, T., Mamiya, Y. and Otsuki, E. Dielectric and Piezoelectric Properties of $(Bi_{0.5}Na_{0.5})TiO_3$-$(Bi_{0.5}K_{0.5})TiO_3$ Systems. *JAPANESE JOURNAL OF APPLIED PHYSICS PART 1-REGULAR PAPERS SHORT NOTES & REVIEW PAPERS*, 1999, 38(9B), 5564.

Sawyer, C. B. and Tower, C. H. Rochelle salt as a dielectric. *PHYSICAL REVIEW*, 1930, 35, 269.

Simon, A. and Ravez, J. Lead-free relaxors with "TTB" structure containing either lanthanum or bismuth. *PHYSICA STATUS SOLIDI (A)*, 2003, 199(3), 541.

Smolenskii, G. A., Isupov, V. A., Agranovskaya, A. I. and Krainik, N. N. New Ferroelectrics of Complex Composition. *SOV. PHYS.-SOLID STATE (ENGL. TRANSL.)*, 1961, 2(11), 2651.

Srimaungsong, P., Udomkan, N., Pdungsap, L. and Winota, P. Effect of CeO_2 on sintering Temperature and Piezoelectric Properties PZT (Zr:Ti =52:48) Ceramics. *INTERNATIONAL JOURNAL OF MODERN PHYSICS B*, 2005, 19(10), 1757.

Subbarao, E. C. Ferroelectricity in $Bi_4Ti_3O_{12}$ and its solid solutions. *PHYSICAL REVIEW*, 1961, 122, 804.

Subbarao, E. C. Crystal chemistry of mixed bismuth oxides with layer-structures. *JOURNAL OF THE AMERICAN CERAMIC SOCIETY*, 1962a, 45, 166.

Subbarao, E. C. A family of ferroelectric bismuth compounds. *JOURNAL OF PHYSICS AND CHEMISTRY OF SOLIDS*, 1962b, 23, 665.

Suchanicz, J., Roleder, K., Kania, A. and Handerek, J. Electrostrictive Strain and Pyroeffect in the Region of Phase Coexistance in $Na_{0.5}Bi_{0.5}TiO_3$. *FERROELECTRICS*, 1988, 77, 107.

Takahashi, H., Numamoto, Y., Tani, J., Matsuta, K., Qiu, J. H. and Tsurekawa, S. Lead-free barium titanate ceramics with large piezoelectric constant fabricated by microwave sintering. *JAPANESE JOURNAL OF APPLIED PHYSICS PART 2-LETTERS & EXPRESS LETTERS*, 2006, 45(1-3), L30.

Takanaka, T., Maruyama, K. I. and Sakata, K. $(Bi_{0.5}Na_{0.5})TiO_3$-$BaTiO_3$ System for Lead-Free Piezoelectric Ceramics. *JAPANESE JOURNAL OF APPLIED PHYSICS PART 1-REGULAR PAPERS SHORT NOTES & REVIEW PAPERS*, 1991, 30(9B), 2236.

Takenaka, T., Okuda, T. and Takegahara, K. Lead-free piezoelectric ceramics based on $(Bi_{1/2}Na_{1/2})TiO_3$-$NaNbO_3$. *FERROELECTRICS*, 1997, 196(1-4), 495.

Ulrich, R. K. and Brown, W. D., *ADVANCED ELECTRONIC PACKAGING*, A John Wiley & Sons, Inc., 2006.

Wang, X. X., Chan, H. L. W. and Choy, C. L. $(Bi_{0.5}Na_{0.5})TiO_3$-$Ba(Cu_{0.5}W_{0.5})O_3$ Lead-Free Piezoelectric Ceramics. *JOURNAL OF THE AMERICAN CERAMIC SOCIETY*, 2003a, 86(10), 1809.

Wang, X. X., Chan, H. L. W. and Choy, C. L. Piezoelectric and dielectric properties of CeO_2-added $(Bi_{0.5}Na_{0.5})_{0.94}Ba_{0.06}TiO_3$ lead-free ceramics. *SOLID STATE COMMUNICATIONS*, 2003b, 125, 395.

Wang, X. X., Chan, H. L. W. and Choy, C. L. $(Bi_{0.5}Na_{0.5})_{0.94}Ba_{0.06}TiO_3$ lead-free ceramics with simultaneous addition of CeO_2 and La_2O_3. *APPLIED PHYSICS A-MATERIALS SCIENCE & PROCESSING*, 2005a, 80(2), 333.

Wang, X. X., Choy, S. H., Tang, X. G. and Chan, H. L. W. Dielectric behavior and microstructure of $(Bi_{1/2}Na_{1/2})TiO_3$ - $(Bi_{1/2}K_{1/2})TiO_3$ - $BaTiO_3$ lead-free piezoelectric ceramics. *JOURNAL OF APPLIED PHYSICS*, 2005b, 97, 104101.

Wang, X. X., Or, S. W., Tang, X. G., Chan, H. L. W., Choy, P. K. and Liu, P. C. K. TiO_2-nonstoichiometry dependence on piezoelectric properties and depolarization temperature of $(Bi_{0.5}Na_{0.5})_{(0.94)}Ba_{0.06}TiO_3$ lead-free ceramics. *SOLID STATE COMMUNICATIONS*, 2005c, 134(10), 659.

Wang, X. X., Tang, X. G. and Chan, H. L. W. Electromechanical and ferroelectric properties of $(Bi_{1/2}Na_{1/2})TiO_3$-$(Bi_{1/2}K_{1/2})TiO_3$-$BaTiO_3$ lead-free piezoelectric ceramics. *APPLIED PHYSICS LETTERS*, 2004, 85(1), 91.

Wu, L., Xiao, D. Q., Lin, D. M., Zhu, J. G. and Yu, P. Synthesis and properties of $[Bi_{0.5}(Na_{1-x}Ag_x)_{(0.5)}]_{(1-y)}Ba_yTiO_3$ piezoelectric ceramics. *JAPANESE JOURNAL OF APPLIED PHYSICS PART 1-REGULAR PAPERS BRIEF COMMUNICATIONS & REVIEW PAPERS*, 2005, 44(12), 8515.

Wu, Y., Zhang, H., Zhang, Y., Ma, J. and Xie, D. Lead-free piezoelectric ceramics with composition of $(0.97\text{-}x)Na_{1/2}Bi_{1/2}TiO_3$- $0.03NaNbO_3$-x $BaTiO_3$. *JOURNAL OF MATERIALS SCIENCE*, 2003, 38, 987.

Xie, R. J. and Akimune, Y. Lead-free piezoelectric ceramics in the $(1\text{-}x)Sr_2NaNb_5O_{15}$ - $xCa_2NaNb_5O_{15}$ (0.05 <= x <= 0.35) system. *JOURNAL OF MATERIALS CHEMISTRY*, 2002, 12(10), 3156.

Xie, R. J., Akimune, Y., Wang, R. P. and Hirosaki, N. Spark plasma sintering of tungsten bronze $Sr_{2-x}Ca_xNaNb_5O_{15}$ (x=0.1) piezoelectric ceramics: II, electrical properties. *JOURNAL OF THE AMERICAN CERAMIC SOCIETY*, 2002a, 85(11), 2731.

Xie, R. J., Akimune, Y., Wang, R. P., Matsuo, K., Sugiyama, T. and Hirosaki, N. Spark plasma sintering of tungsten bronze $Sr_{2-x}Ca_xNaNb_5O_{15}$ (x=0.1) piezoelectric ceramics: I, processing and microstructure. *JOURNAL OF THE AMERICAN CERAMIC SOCIETY*, 2002b, 85(11), 2725.

Xu, W. C., Lam, K. H., Choy, S. H. and Chan, H. L. W., A stepped Horn Transducer Driven by Lead-free Piezoelectric Ceramics, International Symposium on Integrated Ferroelectrics, Hawaii, USA, 2006

Xu, Y. H., *FERROELECTRIC MATERIALS AND THEIR APPLICATIONS*. North-Holland, Elsevier Science Publishers B.V., 1991.

Yoo, J., Hong, J., Lee, H., Jeong, Y., Lee, B., Song, H. and Kwon, J. Piezoelectric and dielectric properties of La_2O_3 added Bi(Na, K)TiO_3–$SrTiO_3$ ceramics for pressure sensor application. *SENSORS AND ACTUATORS A-PHYSICAL*, 2006, 126(1), 41.

Yoo, J., Oh, D., Jeong, Y., Hong, J. and Jung, M. Dielectric and piezoelectric characteristics of lead-free $Bi_{0.5}(Na_{0.84}K_{0.16})_{0.5}TiO_3$ ceramics substituted with Sr. *MATERIALS LETTERS*, 2004, 58, 3831.

Yoo, J. H., Yoon, H. S., Yoon, K. H., Jeong, Y. H. and Park, C. Y., Piezoelectric characteristics of PMN-PZT ceramics for piezoelectric transformer, 1998.

Yu, Z., Ang, C., Guo, R. and Bhalla, A. S. Piezoelectric and strain properties of $Ba(Ti_{1-x}Zr_x)O_3$ ceramics. *JOURNAL OF APPLIED PHYSICS*, 2002, 92(3), 1489.

Zhao, M. L., Wang, C. L., Wang, J. F., Chen, H. C. and Zhong, W. L. Enhanced piezoelectric properties of $(Bi_{0.5}Na_{0.5})_{(1-x)}Ba_x TiO_3$ lead-free ceramics by sol-gel method. *ACTA PHYSICA SINICA*, 2004, 53(7), 2357.

Zuo, R. Z., Rodel, J., Chen, R. Z. and Li, L. T. Sintering and electrical properties of lead-free $Na_{0.5}K_{0.5}NbO_3$ piezoelectric ceramics. *JOURNAL OF THE AMERICAN CERAMIC SOCIETY*, 2006, 89(6), 2010.

APPENDIX

A1. CALIBRATION EQUIPMENT

Calibration is an important process to characterize the performance of the accelerometer. It is necessary to standardize the testing equipment used in the calibration since using different equipment from time to time would cause great difference during the measurement. Some important equipment used for the sensor calibration is listed and importance processing steps were also explained.

A1.1 Multi-channel analysis system

The Multichannel Analysis System (M.A.S. 3550 supplied by Brüel & Kjær Co.) is the main equipment in the calibration process. Basically, the system contains a signal analysis unit, two 100 kHz input modules and a generator and sampling module. The generator and sampling module can generate different kinds of waveforms which can be used as a signal source to drive other devices, for example, the vibrator. The input module is used to collect signal from the measuring devices, which include the calibration including the prototype accelerometer, and a standard reference accelerometer. Since the module has a built-in charge amplifier thus those devices can be connected to the measuring system directly and the output signal in terms of charge will be given. The collected signal will be analyzed by the signal analysis unit.

The measured signal is in the time domain. In order to obtain the frequency response, it is necessary to transform the signal to the frequency domain using the Fast Fourier Transform (FFT). The major advantages of FFT over other types of frequency analysis is the retention of phase information which makes the transformation in either domain (time to frequency and frequency to time) possible. In all types of practical frequency analysis the signal must be time limited before it can be analyzed. The FFT calculation works on finite and well defined blocks of time data record length. The input time signal is multiplied by a weighting function or viewed through a window before the Fourier spectrum is calculated. This window can put a uniform or non-uniform weighting on the time signal (Figure A1). Using no trigger (Free Run), the complex Fourier spectra might have a random phase from measurement to measurement. In this case averaging has no meaning and will only result in a spectrum with zero amplitude and zero phase. Averaging can be performed on the zero phase autospectrum. This is calculated by a complex squaring of the Fourier spectrum, the spectrum multiplied by its own complex conjugate, $A^*A=G_{AA}$. Figure A2 shows a block diagram of a single channel FFT analyzer.

The input time signal is multiplied by a weighting function before the frequency analysis is performed. The selection of the weighting function will affect the resulting autospectrum. Different commonly used weighting functions are shown in Figure A3, including Rectangular, Hanning, Kaiser-Bessel and Flat top windows. A Flat top window (Figure A4) should be used when an accurate measurement of amplitude is required for calibration purposes, since the ripple in the passband of this weighting function is less than 0.01 dB and effect error is minimized by using this weighting function (Harris and Piersol 2002). Hence the flat top window was used in the calibration of accelerometers.

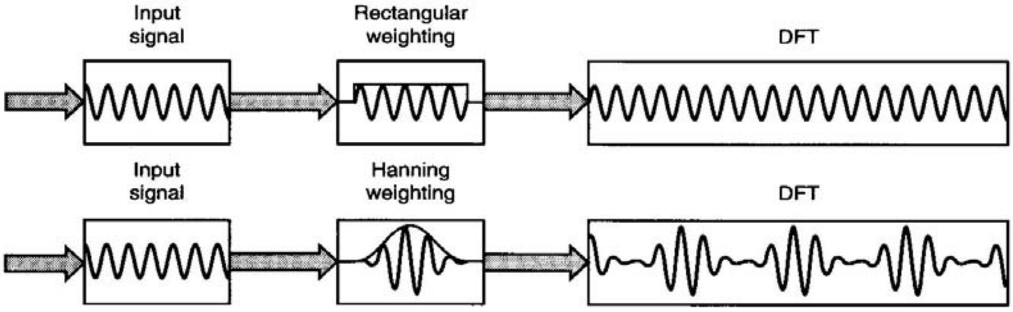

Figure A1 FFT time weighting. The input time signal is multiplied by a weighting function before the frequency analysis is performed. The analyzed time block is then treated like a periodic, repeated signal (B&K 1992).

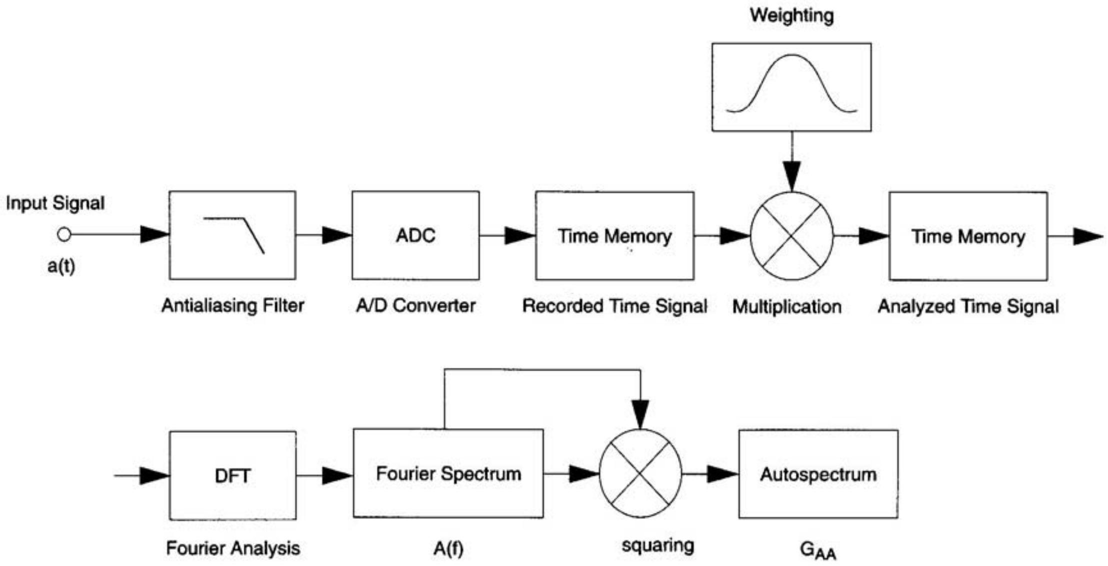

Figure A2 Block diagram of a single-channel FFT analyzer.

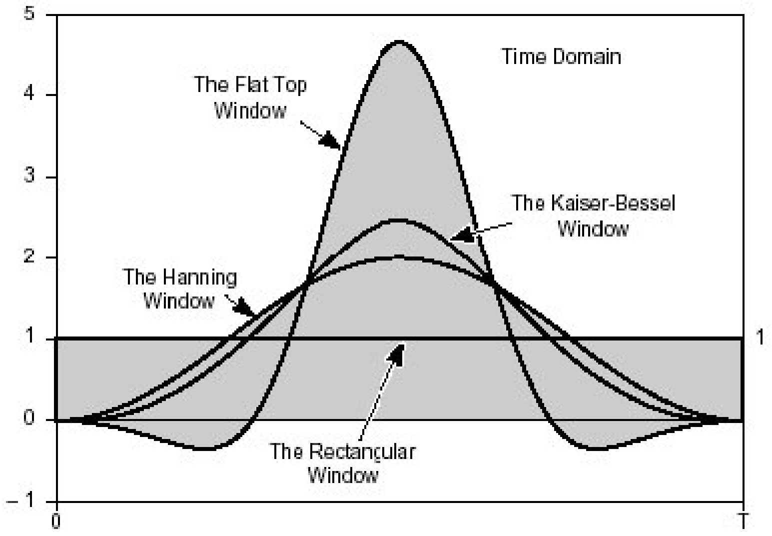

Figure A3 Different weighting functions including Rectangular, Hanning, Kaiser-Bessel and Flat top windows (B&K 1987).

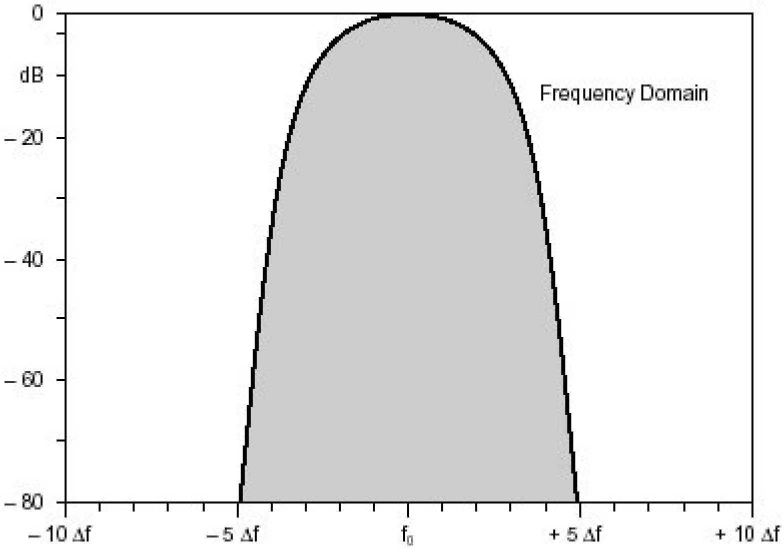

Figure A4 Frequency characteristics of a Flat Top window.

A1.2 Standard Reference Accelerometer

The Brüel & Kjær Standard Reference Accelerometer Type 8305 was used to measure the acceleration of the system in the calibration. This accelerometer is designed to be used in laboratories for making accurate calibration for vibration transducer. The sensitivity of the accelerometer at 159.2 Hz ($\omega = 1000$ s^{-1}), 50 ms^{-2} and 23.4 ^{o}C is 0.1251 pC/ms^{-2}. Its axial resonance frequency is >30 kHz and the useable frequency range is over 10 kHz.

A1.3 Permanent magnet vibrator

A permanent magnet vibrator was used to produce an axial vibration in the calibration. The vibrator was supplied by Ling Dynamic Systems (model V406). The vibrator can generate a max sine force peak of 98 N and 89 N for random force.